The Effect of Damage on the Fracture Toughness of C/C Composites

Lars Denk

DOCTOR OF PHILOSOPHY

Department of Space and Astronautical Science

School of Physical Science

The Graduate University for Advanced Studies

01.01.2010

Content

Abbreviations and Symbols

σ	remote loading stress
σ_{max}	ultimate tensile strength
$\sigma_{f,net}$	tensile net fracture stress
$\sigma_{net,ave}$	tensile net average stress
$\sigma_{gr,ave}$	tensile gross average stress
σ_x	local stress in x-direction
σ_y	local stress in y-direction
a	crack length
a'	notch length
d_0	characteristic distance ahead of a crack where the local stress σ_x just reaches σ_{max}
r	0°-ply fraction
t	thickness
w	width
w_{net}	net sectional width
W_L	total ligament width of a DEN specimen
x	distance from the crack tip in x-direction
F	load
F_{max}	fracture load
G_{12}	shear modulus
K_I	stress intensity factor under mode I
K_{IC}	critical stress intensity factor, also called (fracture) toughness of the material
CP	cross-ply
UD	uni-directional
C/C	carbon-carbon (composite)
DEN	double-edge notched specimen geometry
CT	compact-tension specimen geometry
τ	shear stress
τ_d	interfacial debonding stress
ε_u	the ultimate tensile fracture strain
ρ	bulk density
G_{Ic}	critical energy release rate under mode I
G_{IIc}	critical energy release rate under mode II
G_R	crack extension resistance

1. Introduction

1.1 What are C/C composites?

Carbon-carbon (C/C) composite is at present the most mature high temperature material retaining its superior specific strength and specific modulus at temperatures above 2000°C[1,2]. It consists of carbon or graphite fibre reinforcement in a carbon or graphite matrix and thus, both the matrix and the fibres have the same material constituents, e.g. the chemical element carbon.

The first carbon-carbon composite was obtained by accident in 1958[3]. In a chemical analysis to evaluate the volume fraction of the reinforcement, a polymer matrix composite, PMC was exposed to air at elevated temperature, and the lid of the test chamber was accidentally kept closed. Thus, instead of oxidising the matrix polymer, the PMC was pyrolised. The resulting resin-charred composite was found to possess structural durability, and consequently, the C/C composite was born.

Development of the C/C was at first slow but became rapid in the late 1960s. At that time the space shuttle program required a thermal protection material which had light weight, high thermal shock resistance, a low coefficient of thermal expansion, high stiffness etc.[4,5,6]. Graphite has most of these properties but exhibits a low strength and in particular high toughness. Around this time, the production of high strength PAN-based-carbon fibres had started, and the related fibre-reinforced plastic industry had greatly advanced. In addition, new composite fabrication techniques were available[7]. These factors fuelled the development of the C/C technology and carbon-carbon composites finally emerged as a new class of engineering materials.

1.2 Material constituents of C/C

The Carbon-carbon composite consists of carbon matrix and carbon fibres. These carbons have distorted versions of the graphite form, where carbon atoms are joined by strong covalent bonds. Thus, these carbon materials are highly refractory having the melting point above that of most ceramics. The graphite crystals have high thermal conductivity comparable to that of typical metals. This is another advantage of general carbon materials. While the term graphite refers in a strict sense only to carbon arranged

in a perfectly hexagonal structure, such perfection is rarely achieved in manufactured graphite. Thus, it has become common to use the word graphite as well for carbon which is approaching this limit. Similarly the term graphitization is used to denote high temperature heat treatment of carbons with the aim to obtain a nearer graphitic structure.

In graphite, carbon atoms are arranged in planar basal layers as shown in Fig 1.1. Within each layer the atoms are hexagonally close-packed with an interatomic distance of 0.14 nm and a bonding energy of 522 kJ mol^{-1}. Between, the layers are bonded by van der Waal's forces with a bonding energy of only 17 kJ mol^{-1}. The layers are separated by a distance of 0.33544 nm; however, because alternate layers are in atomic register, the repeat unit distance is just twice. This structure exhibits a high degree of anisotropy.

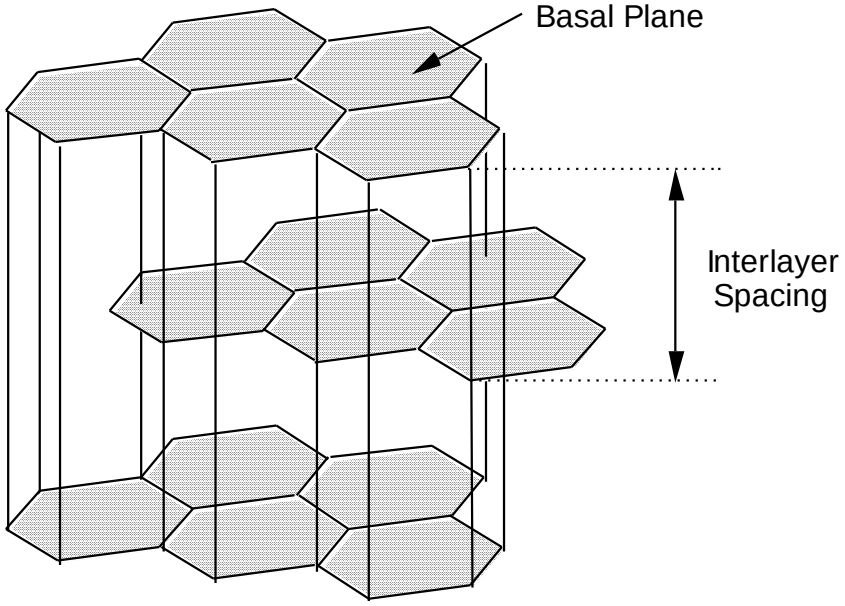

Fig. 1.1: Hexagonal crystal structure of graphite [8]

In the basal plane the material is electrically and thermally conducting and strong, having in addition a theoretical Young's modulus of 1050 GPa. On the other hand, the weak forces between the layers allow slip and lubricating properties with a theoretical Young's modulus of 35 GPa and electrical and thermal conductivity 2 orders of magnitude lower than in the basal plane. Manufactured carbon contains a substantial amount of crystal imperfections and voids so that the theoretical values cannot be achieved. A typical carbon structure consists of discrete graphite crystallite zones oriented randomly to each other and intermingled with a continuum of disordered, porous material [9]. Carbon fibres on the other hand reveal a high degree of perfection with the Young's modulus and tensile strength reaching up to 850 GPa and 6 GPa

respectively, when formed from liquid crystalline pitch. Fig. 1.2 shows the Young's modulus of carbon fibres in comparison to a wide variety of other materials. In this figure the carbon fibres' Young's modulus even reaches twice the value of its nearest competitors, the SIC, shown as second on the right.

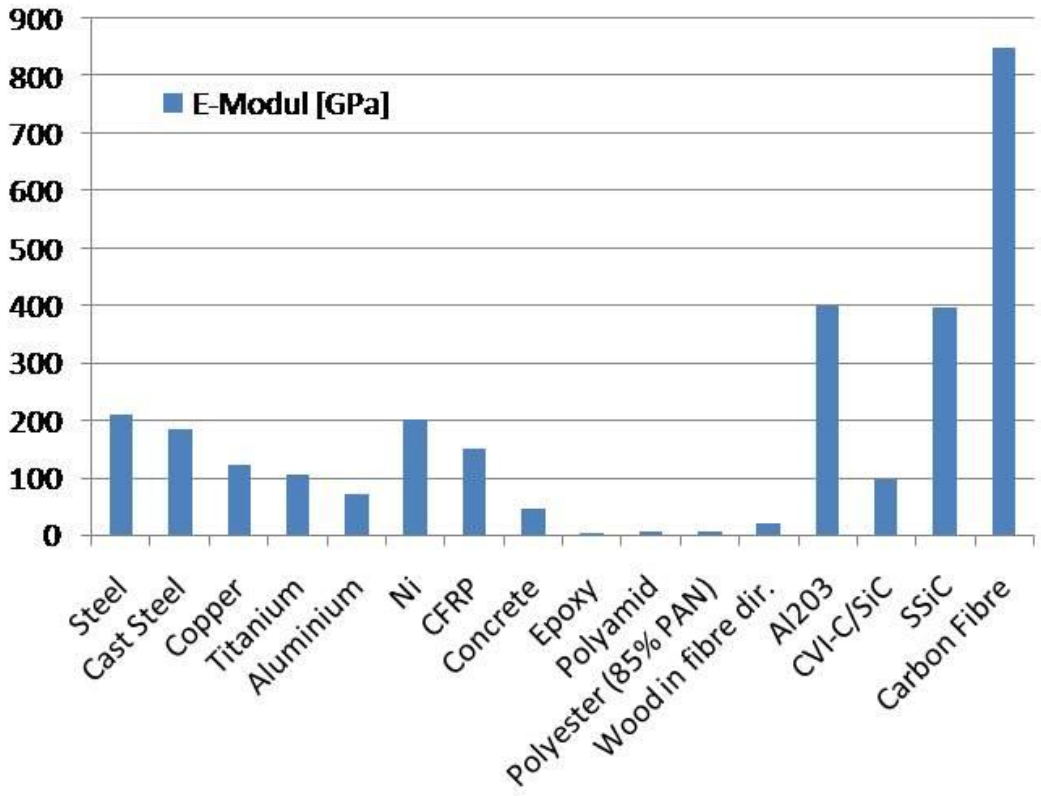

Fig. 1.2: Young's modulus of various materials with that of carbon fibers shown on the right.

1.3 Chemical structure and production route of the carbon fibres

While the theoretical strength of ideal graphite cannot be achieved in manufactured carbon, the high strength of graphite in the basal plane was exploited to produce high strength carbon fibres.

There exist at present three precursor materials to produce carbon fibres, e.g. rayon, polyacrylonitrile (PAN), and pitch. Carbon fibres of considerable strength were at first produced by the Union Carbide Corporation (UCC) at the middle of the 1960s using rayon as precursor material. The UCC showed that isotropic carbon fibres could be transformed into a high modulus product by stretching during high temperature heat treatment. Later, PAN fibres were found to be used instead of rayon fibres as precursor

material which proved to be more economical due to the lower cost of the PAN fibres. Both, carbon fibres with rayon and PAN as precursor material were non-graphitizing and the research continued to develop a truly graphitic fibre. It was then realised that liquid crystal pitch materials could develop a true graphite structure which led Otani in 1965[10] to begin investigating pitch as a precursor material for carbon fibres. Since then research on forming the pitch precursor and transforming the precursor into carbon fibres has continued leading to a commercial carbon fibre formed from liquid crystalline pitch with an ultra high modulus of 850 GPa[11]. Carbon fibres are sold in discontinuous, e.g. “chopped”, continuous, and woven form.

1.4 Applications of chopped, continuous and woven fibres

While carbon composites with chopped fibres, Fig 1.3, are mainly used in disk brakes, continuous Fig 1.4 and woven fibres Fig 1.5 are used in load bearing applications.

Fig. 1.3: Brake disk made of chopped fiber C/C composite (picture from the homepage of SGL carbon)

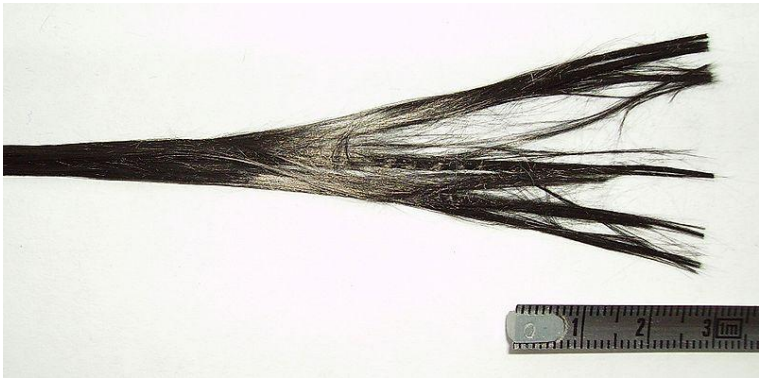

Fig. 1.4: Continuous carbon fibers (picture from Wikipedia)

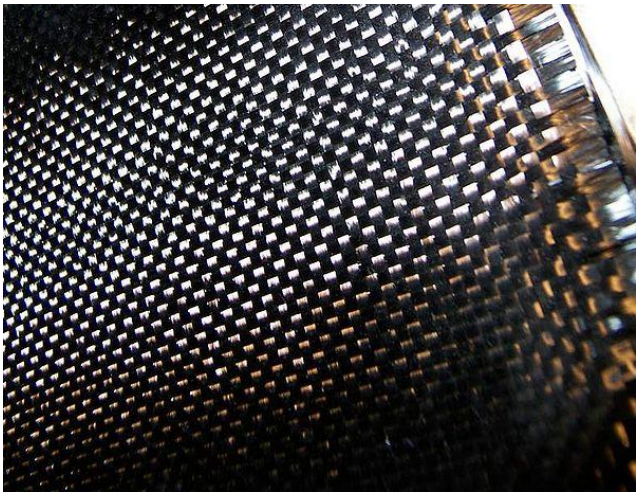

Fig. 1.5: Weaved carbon fiber mat (picture from Wikipedia)

Woven fibres are usually preferred in composite materials because of reduced manufacturing costs and improved damage resistance. However, they are weaker than unidirectional reinforced fibre composites. This is due to curvature of the fibres as a result of the weaving known as crimp acting as stress concentration sources. Unidirectional fibre composites usually have negligible strength in the direction normal to the fibres. This can be overcome by stacking uni-directionally reinforced lamina in orthogonal direction though resulting in an increasing amount of lay-ups which drives up the manufacturing cost. Nevertheless, having the well balanced highest tensile strength they are usually preferred in aerospace applications[12]. Typical fibre lay-ups of two-dimensionally reinforced composite are shown in Fig 1.6. If a load is only applied in one direction, the sheets, or laminae, are laid up with all fibres in one direction, as shown in Fig 1.6 on the left. However, in case of different directions of the applied load, the fibre direction usually alternates. In 2-directional loading, a cross-ply reinforcement $(0/90)_n$ is usually applied whereas in more complex loading cases quasi-isotropic fibre orientations, for example the $(0°/+45°/-45°/90°)_n$ case as depicted in Fig 1.6 on the right, are used. To predict the material properties of a laminated composite from the material properties of single laminae, a special technique, e.g. the lamination theory[13,14] is applied.

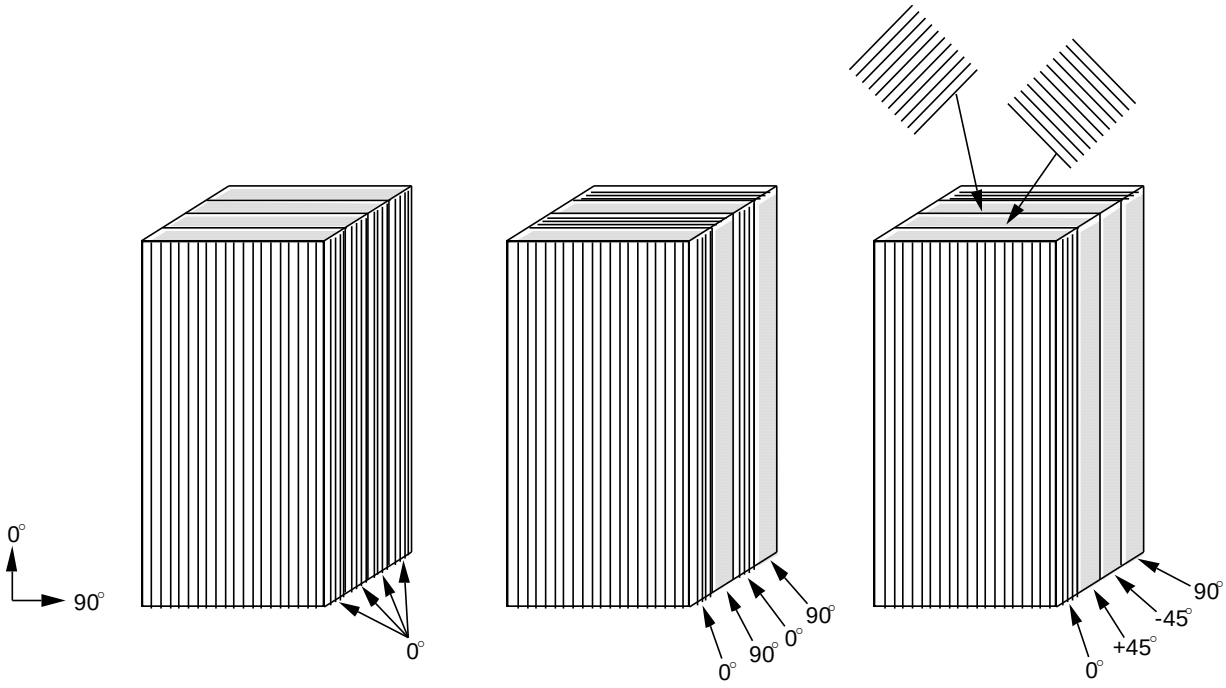

a) UD 0 b) CP 0/90 0 c) QI

Fig. 1.6: Composites with a) UD0, b) cross-ply (CP) 0/90 and c) a typical quasi-isotropic (QI) stacking sequence.

1.5 Production routes for C/C composites

Carbon and its thermodynamic equilibrium phase graphite melt only under high pressure and temperature in the order of 100 bars and 4000 K. This makes chemical routes to produce carbon-carbon composites as melting or sintering virtually impossible. Thus, only the preparation of elemental carbon by thermal decomposition of carbonaceous compounds is suitable for the preparation of solid structural carbon materials. Hydrocarbons are the basic carbonizable compounds. They might either be used in pure form or may contain additional ligands such as oxygen, sulphur, nitrogen, and halogens. Examples of the most suitable precursors are [15]

1. Pure hydrocarbons: gaseous low molecular weight compounds or molten pitches.
2. Oxygen-containing hydrocarbons: non-melting polymers such as phenolics and furans, and oxidised pitches and thermoplastics.
3. Nitrogen-containing hydrocarbons: polyacrylonitrile, polyimide, etc.
4. Sulfur- and halogen- containing compounds: modified pitches.

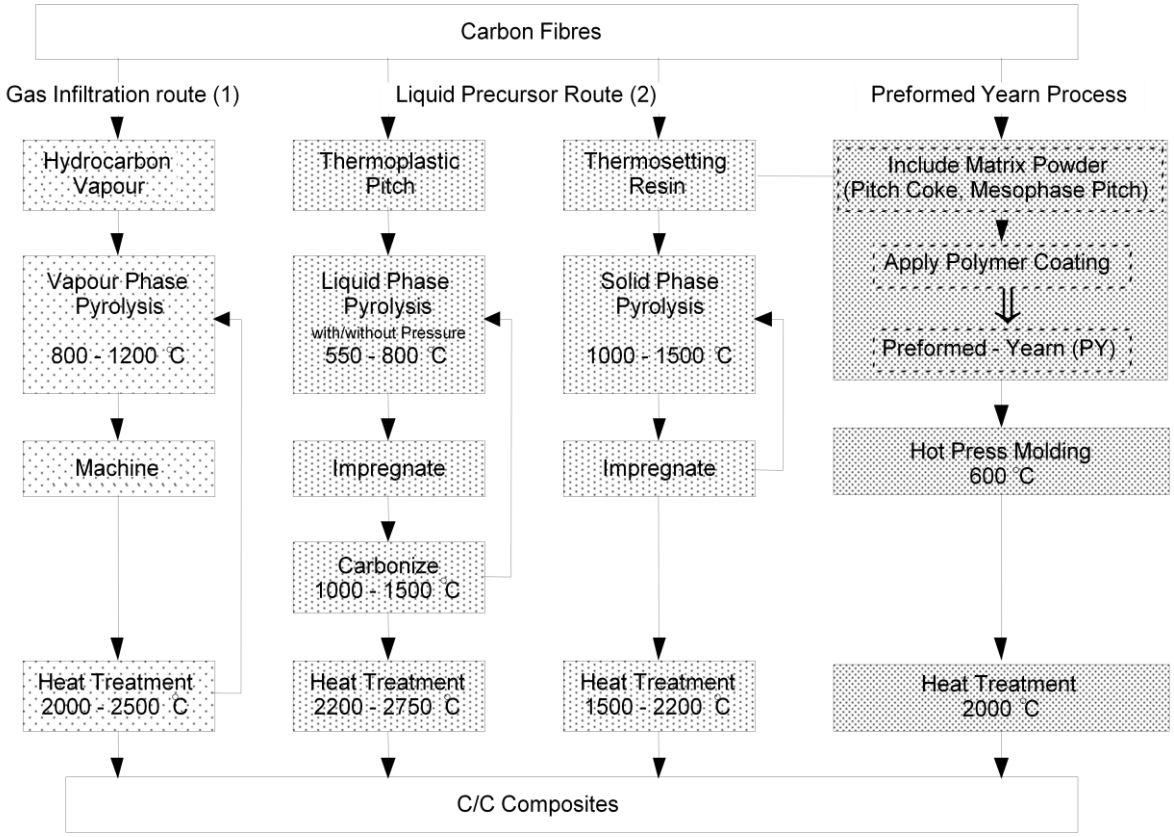

Fig. 1.7: Carbon/carbon processing routes

The main methods of placing the carbon matrix in the carbon perform are shown in Fig. 1.7. The first approach is to infiltrate a hydrocarbon gas into the preform under conditions where pyrolysis of the gas occurs directly on the fibre surfaces, gradually building up a layer of matrix. Since the surface layers are preferentially densified in this method, a good filling of the inner layers have to be confirmed. The second involves the impregnation of carbon fibre preform with a liquid carbon precursor, such as resin or pitch, and then pyrolysing the precursor to form the carbon matrix. While in the gaseous process the pyrolysis is not complete, so that a part of ligands remains after the process. Hence, an additional heat treatment is usually required. This causes substantial volumetric shrinkage. Thus, pores and shrinkage cracks are common in the matrix. These defects are filled by subsequent re-infiltration and pyrolysis/heat-treatment operations to densify the composite[16]. To overcome the time consuming cycles of repeated impregnation and carbonisation, the so-called preformed yearn (PY) method, shown in Fig. 1.8, was introduced. In this method, bundles of carbon fibres are filled with precursor particles of carbon matrix and sheathed with polypropylene films. The resulting material is yearn-like having a diameter of 1 to 2 mm and a length of 200 to 1000 m. The preformed yearns are then woven or uni-directionally arranged in sheets,

and the C/C is produced by a single hot press process of the laminated sheets followed by heat-treatment without further densification treatment [17].

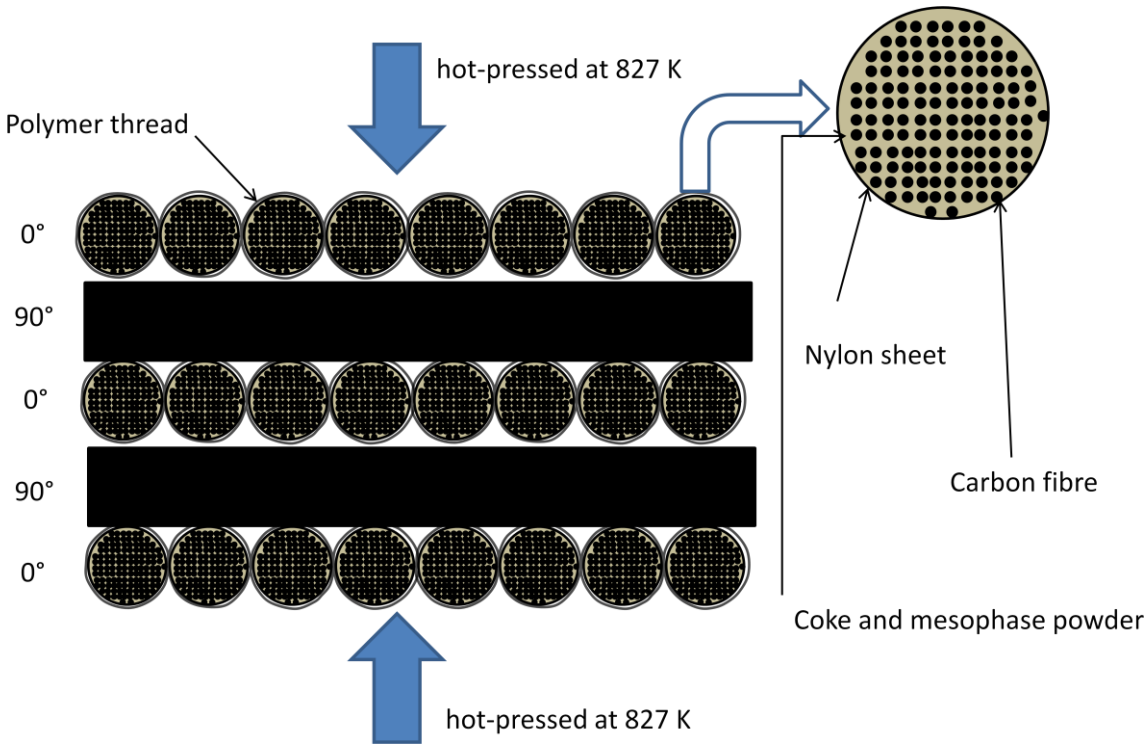

Fig. 1.8: The preformed yearn (PY) method.

1.6 Specific advantages and resulting applications of C/C composites

The appreciated properties of the C/C composites lie in its

- high (specific) strength and high wear resistance at elevated temperatures,
- high thermal shock resistance
- low coefficient of friction at elevated temperatures
- high thermal conductivity, and
- high biocompatibility,

leading to applications as outlined in the following.

The most intensive use of carbon-carbon composites is in brakes of aeroplanes and race cars. The rapid deceleration occurring in brakes generates a substantial amount of frictional heat. Carbon-carbon composites have a high wear resistance and retain strength at high temperatures. In addition, they maintain a more consistent performance over the life of the part, and they are much lighter than their steel counterparts saving,

for example, up to 800 kg on a Boeing 747. Well-known applications of C/Cs are rocket nozzles where the C/C's high temperature erosion and abrasion resistance is appreciated. Similar to the rocket, C/Cs are used for the nose cone and leading edges of the space shuttle wings and the heat shields of ballistic missiles because of their high temperature resistance. C/Cs are also used in the glass bottle industry as transfer pads in contact with the molten glass. Emerging applications are in fusion reactors because of the C/C's high temperature strength and thermal shock resistance and bone transplants because of its extremely good bio-compatibility[18].

1.7 Specific drawbacks of C/C composites

Despite its superior high temperature behaviour, the C/C composite has some important drawbacks which are their

- high cost,
- susceptibility to oxidation at elevated temperatures, and
- not fully clarified fracture behaviour which presently permits only applications in secondary structures.

It goes without saying that the fracture behaviour of carbon-carbon composites must be fully understood in order to make full use of its high strength and to broaden the field of applications substantially. Thus, while the developments of more cost-effective production routes and of oxidation inhibitors are large research fields themselves, this work will concentrate on the fracture behaviour of C/C composites.

1.8 Route of discussion

The route of discussion will be as follows: At first, the shear band effect we will introduce the shear band model in Ch. 2, which, according to their inventors explains the high toughness of C/C composites. In addition, some basic facts about the C/C composite will be introduced in this chapter. In the following Ch. 3, actual shear band observation will be carried out. Since shear fracture is essential for shear band formation, this topic will be examined in Ch.4. As we will find out, shear damage has a substantial effect on the strength of C/C composites so that we will discuss this issue more in detail in Ch. 5. In the following Ch. 6, a basic strength enhancing model will be established. In Chapter 7, the effect of shear damage at stress concentration sources will be examined by use of a multi-holed geometry. Finally, in chapter 8, all results will be gathered to establish a basic model explaining the high toughness of C/C composites.

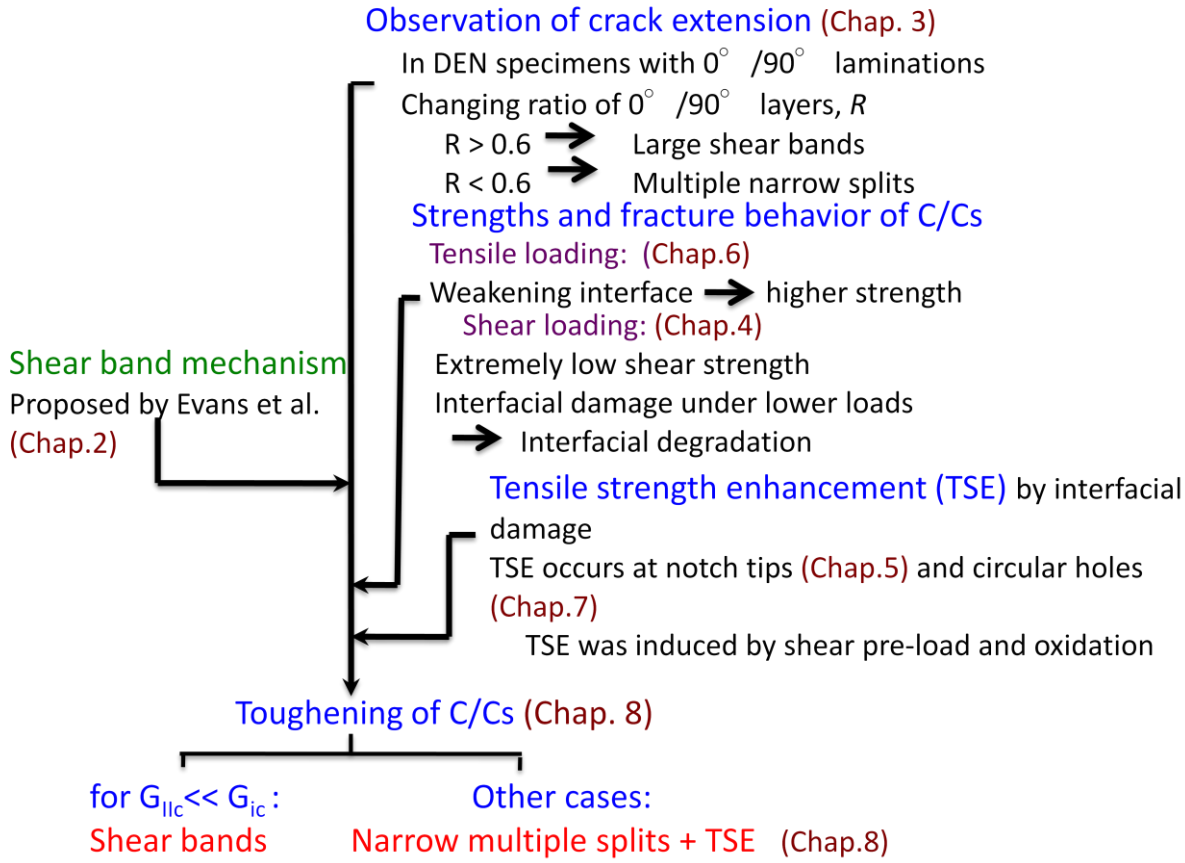

Fig. 1.9: Route of discussion.

---

[1] Fitzer E, Heym M. High temperature mechanical properties of carbon and graphite (a review). High Temp-High Pressures 1978; 10: 29-66

[2] Fitzer E, Gkogkidis A, Heine M. Carbon fibres and their composites (a review). High Temp-High Pressures 1984; 16: 363-392

[3] J.H. Brahney, Aeros. Eng., 7(6), pp. 15 (1987)

[4] E. Fitzer, L. M. Manocha, Carbon reinforcements and carbon/carbon composites, Springer-Verlag (1998)

[5] R. M. Gill, Carbon fibers in composite materials, ILIFFE books (1972)

[6] J. D. Buckley, Ceramic Bulletin, 67(2), pp. 364 (1988)

[7] G. Lubin, Handbook of composite materials, Reinhold Pub (1974)

[8] J. D. Buckley, Ceramic Bulletin, 67(2), pp. 364 (1988)

[9] C. R. Collins, in: C. R. Collins (eds) Essentials of carbon-carbon composites, The Royal Society of Chemistry (1993)

[10] S. Otani, Carbon, 3, pp. 31 (1965)

[11] E. Fitzer, L. M. Manocha, Carbon reinforcements and carbon/carbon composites, Springer-Verlag (1998)

[12] G. Savage, Carbon-carbon composites, Chapman & Hall (1993)

[13] D. Hull, An introduction to composite materials, Cambridge University Press (1981)

[14] R. M. Jones, Mechanics of composite materials, McGraw-Hill, (1975)
[15] E. Fitzer, L. M. Manocha, Carbon reinforcements and carbon/carbon composites, Springer-Verlag (1998)
[16] B. Rand, in: C. R. Collins (eds) Essentials of carbon-carbon composites, The Royal Society of Chemistry (1993)
[17] H. Nagao, T. Nakagawa, H. Hirai, Manufacture of unidirectional carbon fiber reinforced carbon composites by preformed-yearn method, Tanso, 186, pp. 7 (1999)
[18] G. Savage, Carbon-carbon composites, Chapman & Hall (1993)

2. State of research on the fracture of C/C

2.1 Fracture

Fracture describes an event, in which a structure is separated into two or more pieces due to overloading, and, of the various structure failure modes (buckling, fracture, excessive plastic deformation), fracture is one of them. In most cases fracture does not occur due to an unforeseen overload but due to crack extension under "normal" service loads. Fracture might occur in very different ways depending on the material types. For example, glasses behave at first perfectly elastic to fail then suddenly due to their tensile load. In contrast, many metallic solids deform extensively by plastic flow prior to rupture under shear. The process of fracture can be differentiated into crack initiation and ultimate fracture. While the process of crack initiation is very difficult to treat, several concepts exist to predict fracture once a crack of finite length has evolved. Producing a "natural" crack of finite length is very difficult in case of CCs. The problem is generally solved by cutting, for example with a diamond cutting blade, a narrow notch into the test specimen. It is then assumed that once a small crack has evolved from the notch tip the same conditions apply as for a naturally grown crack.

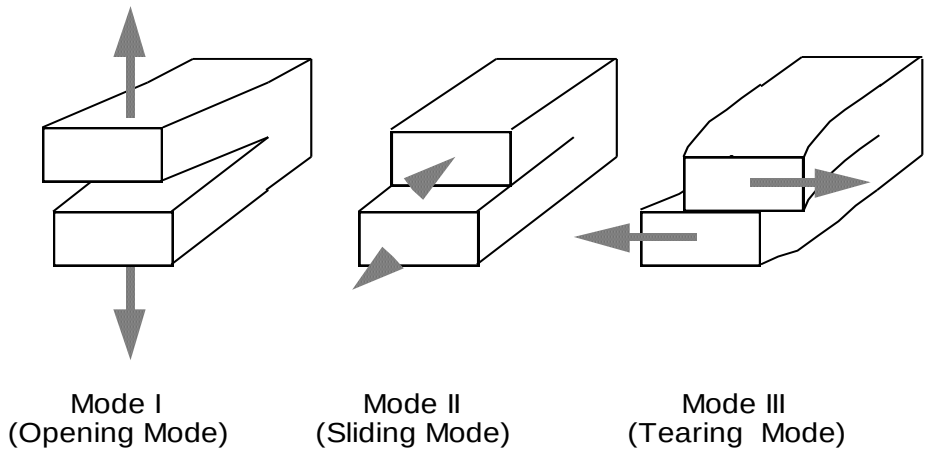

Fig. 2.1: Modes of loading

Since a specimen can be loaded under shear or tension it is necessary to differentiate the basic modes of loading under which fracture can occur. There exist 3 basic modes of loading as shown in Fig. 2.1 and all other loading conditions are simply a combination of the three. In Fig. 2.1, mode I refers to cleavage (opening) mode I,

while the other two are in-plane shear (sliding) mode II, and out-of-plane shear (tearing) mode III.

2.2 The shear band effect

In actual load bearing applications, C/C composites are most likely to be used under tension, and thus, by far the most research has been concentrated on mode I fracture. It was then found that the fracture phenomenon largely changes with the fibre orientation as shown in Fig. 2.2 for double-edge notched (DEN) specimens. In the cases of fibre orientation normal to the loading UD90, quasi-isotropic, or cross-ply (CP) $(0/90)_n$ fibre orientation, fracture occurs normal to the loading direction between the notches. On the other hand, in case of uni-directionally reinforced C/C with fibres parallel to the loading direction UD0, splitting crack formation parallel to the loading direction occurs first. Finally, ultimate fracture occurs in the net section between the parallel cracks in a random fashion.

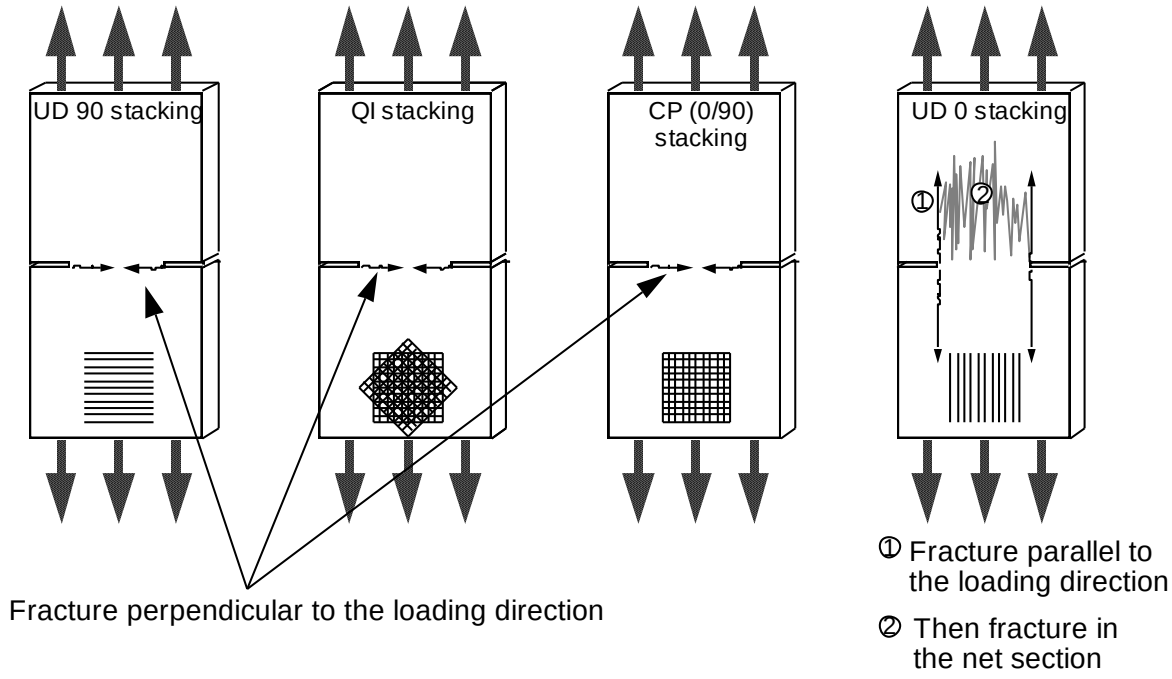

Fig. 2.2: Fracture pattern of C/C composites

In the past, in particular the UD0 with fibres only in loading direction and the cross-ply $(0/90)_n$ cases have been studied. The UD90 case having only fibres normal to the loading direction is due to its low tensile strength of no practical interest. The quasi-isotropic case reveals a much higher shear strength than the UD0 and the CP 0/90

cases. However, its tensile strength is lower which may be the reason why this configuration has drawn less attention in the past than the first two.

According to findings by Evans et al.[19] a major stress relaxation mechanism exists in form of a so-called "shear bands". This result is primarily based on experiments with cross-ply laminated C/C composites. The shear bands can be imagined as follows: Tensile stress concentrations at cracks, (notch) tips, or holes inevitably cause shear stresses as shown in Fig. 2.3 (a). These shear stresses can lead to shear damage propagating parallel to the loading direction in form of a band if the shear stress exceeds the shear strength of the material. Since the occurring shear stresses at holes or notch tips are usually substantially smaller than the tensile component, shear band formation can only occur if the material's tensile strength is much higher than its shear strength. Otherwise, the specimen fails under mode I without prior shear damage. A typical shear band formation is shown in Fig. 2.3 (b).

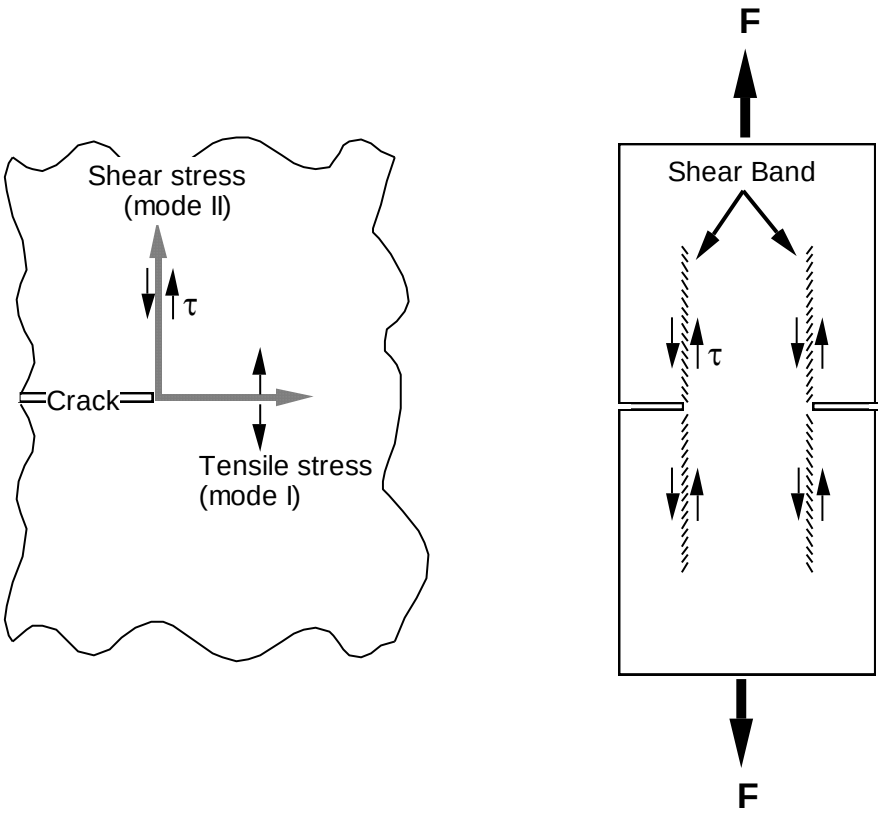

Fig. 2.3: Stress state at cracks and shear band formation

The original shear band concept is based on an analytical model developed by

Fleck[20]. Fleck pointed out that brittle materials, as for example C/C composites, can have strong non-linear shear stress-strain behaviour due to tensile micro-cracking caused by remote shear loading. In such cases shear failure occurs due to the nucleation, growth and coalescence of voids or cracks under a localised concentrated stress, with the material outside the damage zone behaving rigidly. This failure process of shear localisation is in qualitative terms similar to the shear localisation phenomenon previously reported in metals.

Chan et al.[21] examined analytically the shear band in a centre-cracked infinite plate under remote tensile loading. Assuming a constant yield shear stress, they calculated the shear band extension length as a function of the applied load. Chan et al. found that the tensile stress concentration at the crack tip diminishes when the shear band extents. Evans[22] pointed out that a shear band length over three times longer than that of the pre-crack (notch) length makes the specimen essentially notch insensitive. Recently, Turner[23] and Brønstedt[24] categorised brittle matrix composite (CMC) materials into 3 groups, shown in Fig. 2.4, by comparing the material's shear modulus G_{12} and the fibres ultimate tensile strength S. They arranged the 3 categories in a mechanism map as shown in Fig. 2.5 and concluded that materials with $G_{12} / S \leq 80$ exhibit tensile stress redistribution due to shear band formation and defined them as class III materials. From their experimental results they concluded that C/C composite falls into the group of class III materials.

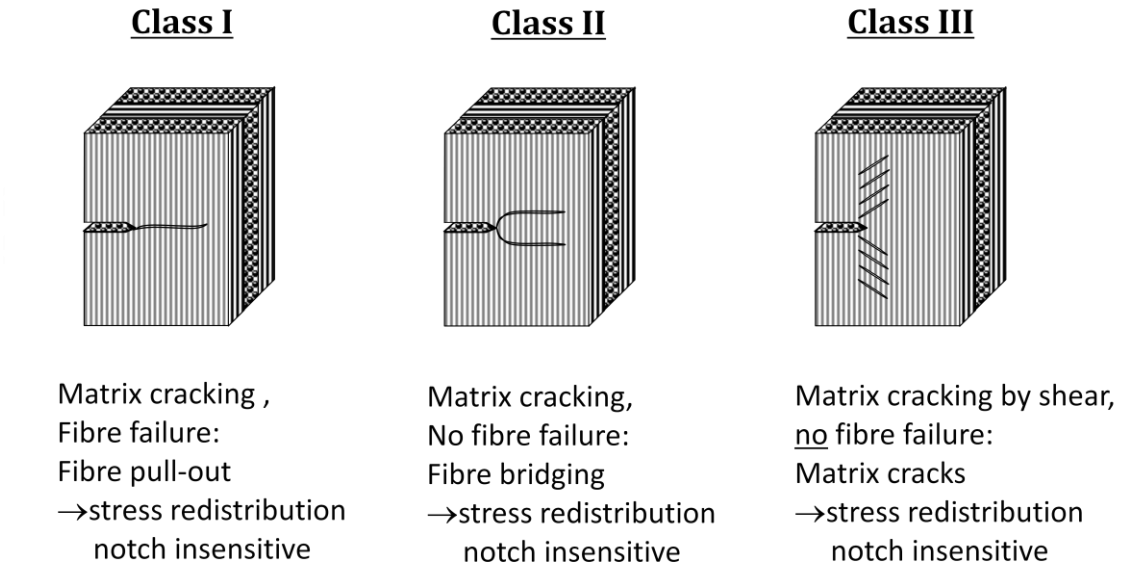

Fig. 2.4: Three classes of toughening mechanism of brittle matrix composites (CMC) by Evans et. al.

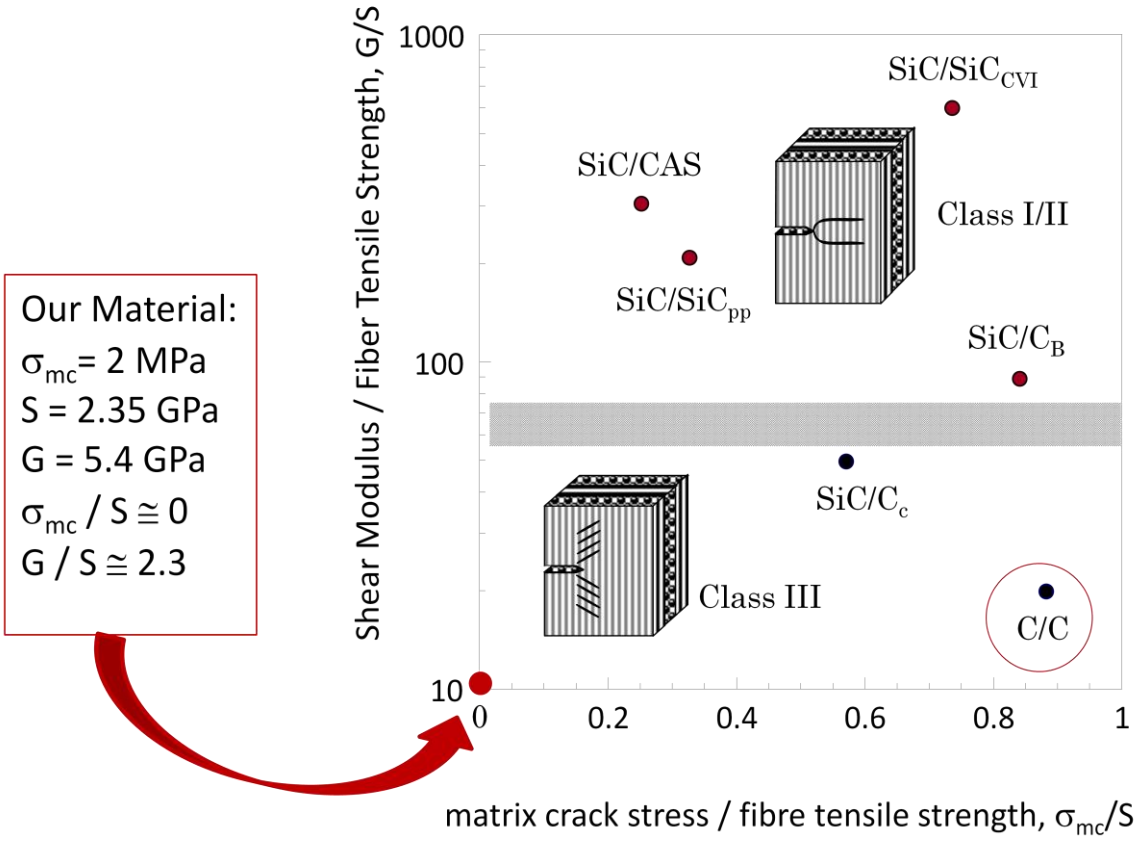

Fig. 2.5: Proposed mechanism map by Evans et al.

Inserting the examined C/C's data into the required equation, we must locate our C/C material at a different location on the mechanism map, nevertheless it would still fall into class III so that shear band formation should be the prevailing mechanism.

Kogo et al.[25] examined the fracture toughness of C/C composites by use of a double-edge notched (DEN) geometry. They pointed out that shear band formation could not be observed, although their C/C material would have clearly been categorised as a class III member. In their experiments with cross-ply 0/90 laminated C/C composites, the C/C showed a high degree of toughness. The net fracture stress was found to be slightly lower that that of un-notched specimen. However, if the net sectional width was small, higher net fracture stresses that those of their un-notched counterparts could be observed, as shown in Fig. 2.6. Consequently, the damage occurring around notches has a positive effect on the materials strength. However, this mechanism cannot be explained by a stress relaxation mechanism as shear band formation. Fig. 2.7 shows experimental results of the strength and fracture pattern of their UD 0 counterparts. In this case, shear band formation in form of a shear crack

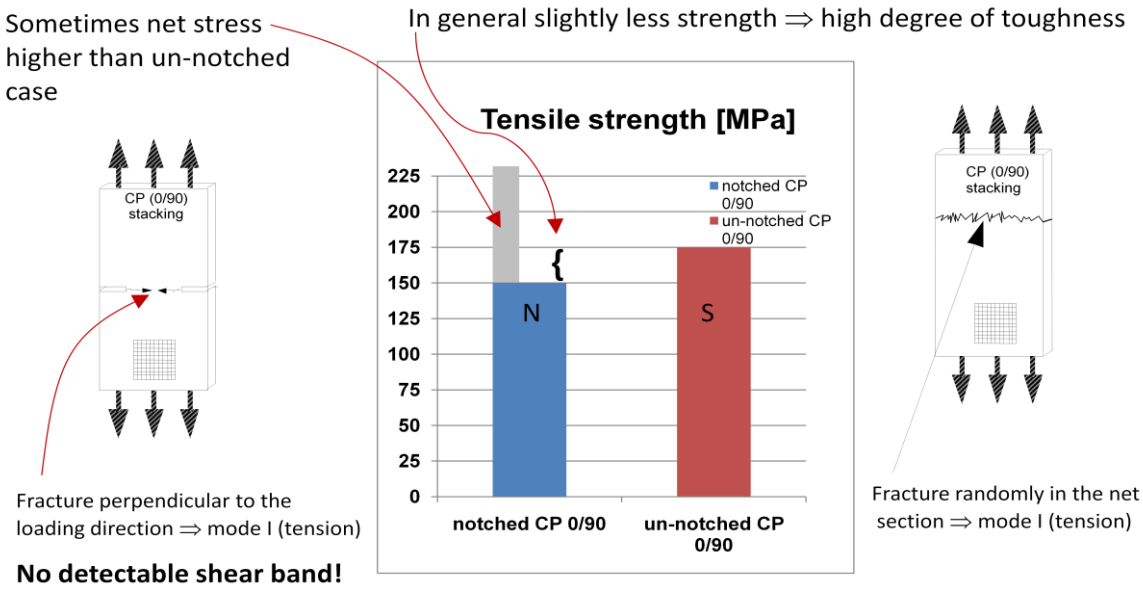

Fig. 2.6: Fracture pattern and strength of cross-ply 0/90 C/C composites.

propagating parallel to the loading direction can be observed. In addition, the net fracture stress of the notched C/C and the tensile strength of the un-notched specimens were the same. Thus, the notched C/C reveals complete notch insensitivity in the UD 0 case. We can summarize, that the C/C reveals different fracture patterns and different

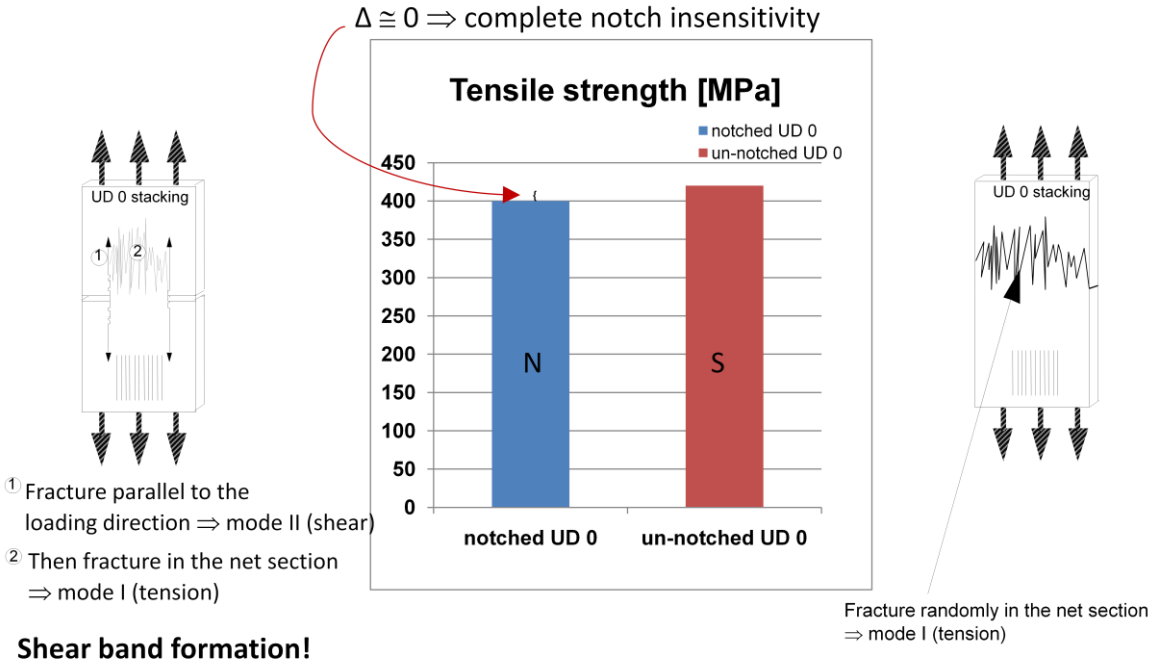

Fig. 2.7: Fracture pattern and strength of UD 0 C/C composites.

degrees of fracture toughness depending on the fibre orientation although its position on the Evans' mechanism map would not change. This casts doubt on the universal applicability of this model.

2.3 Tensile fracture criteria to predict failure of C/C

While the effect of shear band formation is still in the discussion, there exists less tendency towards one particular fracture criterion[26,27,28,29,30,31,32,33,34]. Instead, several fracture criteria have been shown to predict the fracture of C/Cs successfully. The most common ones are examined in the following.

2.3.1 Fracture toughness criterion

It has been mentioned above that fracture can occur in very different fashions ranging from perfectly brittle to plastic yielding. Figure 2.8 shows the typical tensile stress-strain behaviour of carbon-carbon composites. In this figure, the stress-strain behaviour in tension is linear almost up to ultimate fracture which implies that plastic deformation prior to tensile failure is small. In such cases fracture can be analysed on the basis of elastic concepts. For such occasions, the most prominent is the Linear Elastic Fracture Mechanics (LEFM)[35,36] in which the stress field at the crack tip is evaluated. We will introduce here only the mode I case, the other two cases can be readily obtained from the literature[37].

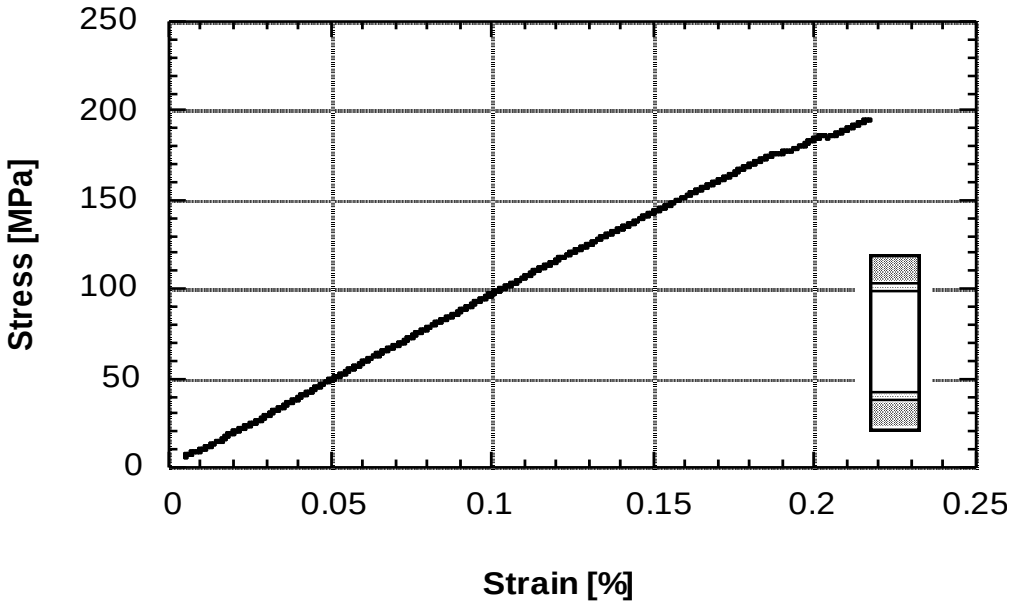

Fig. 2.8: Typical tensile stress-strain curve of 0/90 cross-ply laminated C/C

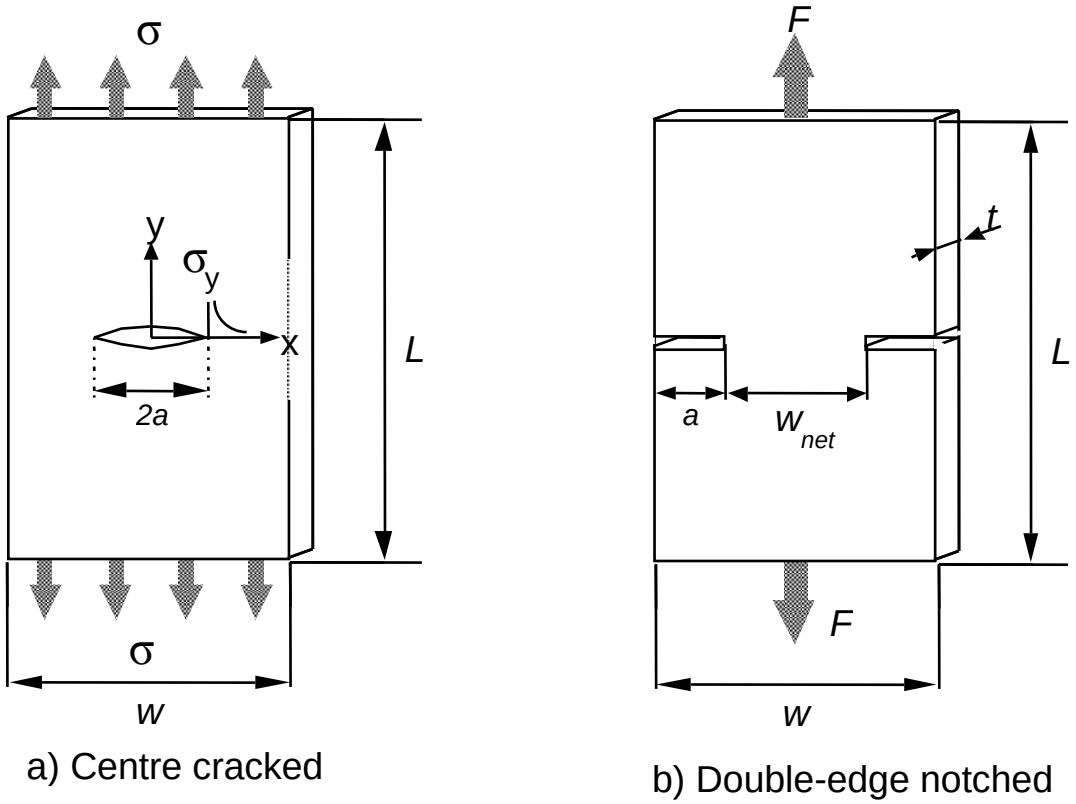

Fig. 2.9: Dimensions of centre-cracked and double-edge notched specimen.

Let us consider a elastic centre cracked body as depicted in Fig. 2.9(a) loaded under mode I by a remote stress σ

$$\sigma = \frac{F}{w \cdot t} \qquad (2.1),$$

where load is denoted by F, the specimen width by w, and the specimen thickness by t. When the material is isotropic and its response is linear-elastic, the stress field just ahead of the crack tip can be determined[38], and σ_x and σ_y are given by

$$\sigma_x = \frac{K_I}{\sqrt{2\pi x}}, \qquad \text{and} \qquad (2.2)$$

$$\sigma_y = \frac{K_I}{\sqrt{2\pi x}}. \qquad (2.3)$$

Thus, σ_x and σ_y depend only on the distance from the crack tip x and a constant parameter K_I, the so-called stress intensity factor under mode I[39]. K_I itself is defined as

$$K_I = \sigma\sqrt{\pi a} F\left(\frac{a}{w}\right), \qquad (2.4)$$

with a and σ denoting the crack length and the remote loading stress, respectively, and

$F\left(\frac{a}{w}\right)$ being a geometry factor which accounts for the finite width of the specimen. Evaluating Eq. (2.2) and (2.3) we find that the stresses σ_x and σ_y at the crack tip, as $x \to 0$, are proportional to the stress intensity factor K_I. Assuming that fracture occurs once the stress field at the crack tip becomes too high for the specimen to bear we might as well say that fracture occurs once the actual stress field exceeds a critical K-value, K_{IC}, the so-called (fracture) toughness of the material,

$$K_I \geq K_{IC} . \tag{2.5}$$

Thus, the fracture toughness of a material can be interpreted as the highest stress intensity K that can be supported by a cracked component. This is the core concept of the fracture toughness criterion.

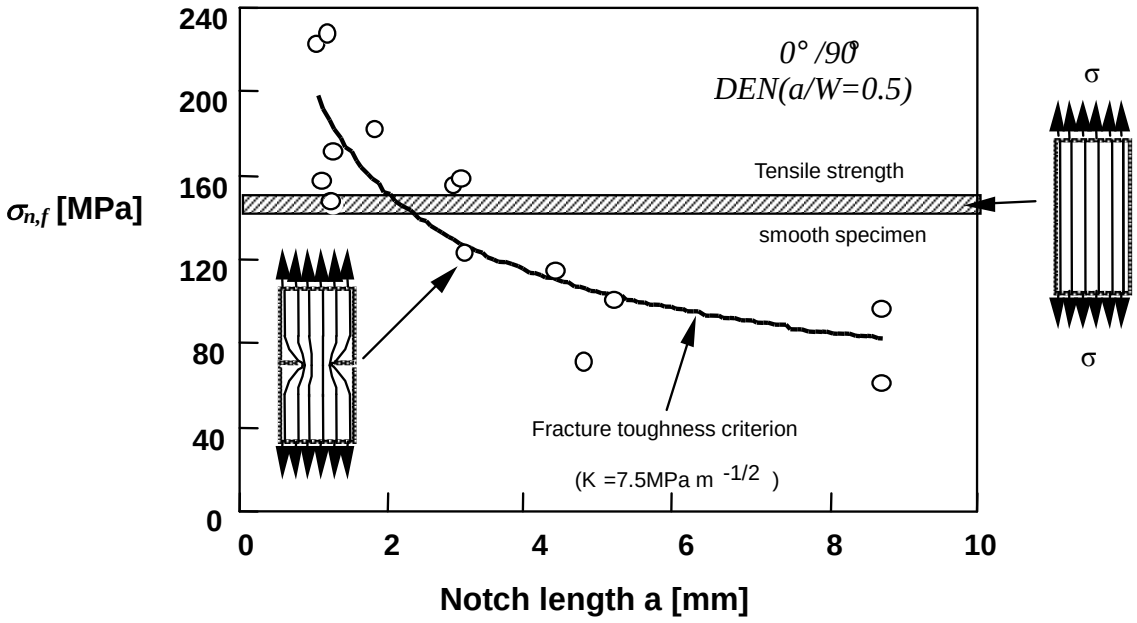

Fig. 2.10: Net fracture stress of double-edge notched (DEN) C/C composite specimen [Hatta et al.].

The fracture toughness criterion has been successfully applied for example by Evans[40] and Hatta[41] as shown in Fig. 2.10 using cross-ply laminated C/Cs. In this figure experimental results of DEN specimens with constant ratio of a over w are arranged in terms of the net fracture stress $\sigma_{n,f}$

$$\sigma_{n,f} = \frac{F_{\max}}{w_{net} \cdot t} \tag{2.6}$$

as a function of the notch length a. In equ. (2.6), F_{max}, t, and w_{net} denote the load at

fracture, the thickness, and the net sectional width, as depicted in Fig. 2.9 (b). Two aspects are worth noting in this figure: All specimen fail roughly at the same critical stress intensity K_c. Thus, K can be used to determine the fracture of cracked specimen. In addition, at small notch lengths, net fracture stresses higher than that of smooth specimens, shown in Fig. 2.10 as a vertical shaded band, are measured. This indicates that the stress concentration at the notches can, in some cases positively affect the strength of the material.

One of the criterion's disadvantages is that, from a strict perspective, it is only valid for cracked specimens and thus not for cases with mild stress concentrations like holes. However, Kostopolous and Pappas [42] showed that the fracture toughness criterion can be applied by substituting holes with notches of the same length as the hole's diameter. This can reasonably be justified if one assumes that cracks emerge from the hole resulting in a similar stress field at the crack tip as a "perfect" crack.

2.3.2 Point stress criterion

The point stress criterion is based on a linear-elastic concept, which was originally used to predict the ultimate fracture in polymer matrix composites with stress concentration sources. In the point stress criterion [43], a presumed material constant, the characteristic distance d_0, is introduced, as shown in Fig. 2.11. Fracture is assumed to occur once the stress σ_y reaches at the characteristic distance d_0 from the notch tip the material's ultimate tensile strength (UTS) σ_{max}. Though the physical meaning of the characteristic distance d_0 is not fully understood, it is considered that d_0 is related to a damaged area in which stress relaxation due to sub-critical local fracture occurs.

The applicability of the point stress criterion was examined by Hatta et al. [44] using cross-ply (0/90) and quasi-isotropic stacking sequences. It was shown that the point stress criterion can be applied and that it gives practically the same results as the fracture toughness criterion. The major advantage of the point stress criterion is that it is not restricted to cracked specimens. It can be used as long as the material's fracture is brittle. However, Kogo et al. [45] later found different characteristic distances for notched and holed specimen which limits the universal usage of this criterion.

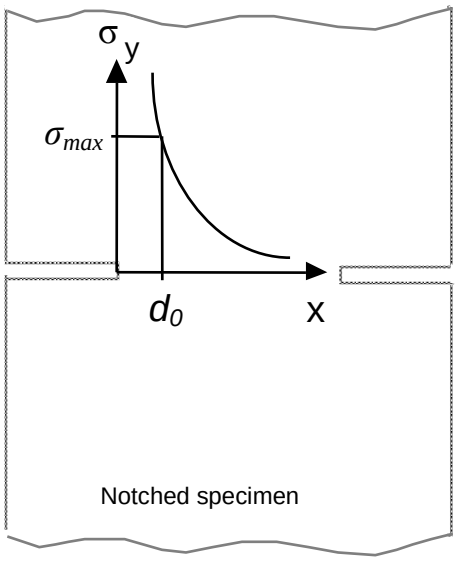

Fig. 2.11: Point-stress criterion (PS)

2.3.3 Net stress criterion

If substantial plastic yielding occurs, the stress concentration at the notch or crack tip might almost disappear. Such an idealistic structure with uniform stress field is said to be "notch insensitive". Failure is in this case suspected to occur when the uniform stress $\sigma_{n,f}$ of Eq. (2.6) reaches the material's ultimate tensile strength σ_{max},

$$\sigma_{n,f} = \sigma_{max}. \qquad (2.7)$$

Although somehow contradicting to the aforementioned brittle nature of the C/C composite, it was shown by Kiuchi et al.[46] that in some occasions, this criterion can be used to predict failure of the C/C composite.

2.4 Summary

In this chapter, the shear band formation model and the most common fracture criteria relevant to carbon-carbon composites were summarized. We found that the examined C/C can be categorised as so-called class III material in the Evans et al. terminology for which shear band formation is the prevailing mechanism. Observation of the fracture pattern in the CP 0/90 and UD 0 cases reveal that these to configurations reveal different fracture pattern and degrees of toughness. In special cases of the CP 0/90 configuration even higher strength than that of un-notched specimens was observed. All this is hard to fit into the shear band approach. In particular, higher

strength than that of smooth (un-notched) specimens cannot be explained by a concept which is based on stress relaxation.

The fracture toughness criterion and the point stress criterion showed roughly the same performance to predict the fracture of notched and holed C/C composites with cross-ply (0/90) fibre orientation. Since fracture toughness data can be obtained in a straight-forward manner, this criterion is preferable. In addition to the two criteria, it was found that the net stress criterion can also be partly applied. However; this is in strong contrast to the above two criteria. While the fracture toughness and the point stress criteria assume negligible plastic deformation around the crack tip the net stress criterion implies that the damage around the notch tip is so large that the stress concentration disappears.

---

[19] A. G. Evans, F. W. Zok, Review, The physics and mechanics of fibre-reinforced brittle matrix composites, J. Mater. Sci., 29, pp. 3857 (1994)

[20] N. A. Fleck, Brittle fracture due to an array of microcracks, Proc. R. Soc. Lond., A 432, pp.55 (1993)

[21] K. S. Chan, M.Y. He, J. W. Hutchinson, Cracking and stress redistribution in ceramic layered composites, Mater. Sci. Eng., A 167(1-2), pp. 57 (1993)

[22] A. G. Evans, F. W. Zok, Review, The physics and mechanics of fibre-reinforced brittle matrix composites, J. Mater. Sci., 29, pp. 3857 (1994)

[23] K. R. Turner, J. S. Speck, A. G. Evans, Mechanisms of deformation and failure in carbon-matrix composites subject to tensile and shear loading, J. Am. Ceram. Soc., 78(7), pp. 1841 (1995)

[24] P. Bronstedt, F.E. Heredia, A. G. Evans, In-plane shear properties of 2-D ceramic matrix composites, J. Am. Ceram. Soc., 77(10), pp. 2569 (1994)

[25] Y. Kogo, H. Hatta, H. Kawada, et al., Effect of stress concentration on tensile fracture behaviour of carbon-carbon composites, J. Comp. Mater., 32(13), pp. 1273 (1998)

[26] G. E, Griesheimer, P. B. Pollock, S. C. Yen, Notch strength and fracture behaviour of 2-D carbon-carbon composites, J. Am. Ceram. Soc., 76(4), pp. 944 (1993); CT

[27] A. G. Evans, F. W. Zok, Review, The physics and mechanics of fibre-reinforced brittle matrix composites, J. Mater. Sci., 29, pp. 3857 (1994)

[28] F. E. Heredia, M. Spearing, T. J. Mackin, et al., Notch effects in carbon matrix composites, J. Am. Ceram. Soc., 77(11), pp. 2817 (1994); DEN, CN, CH

[29] T. J. Mackin, T.E. Purcell, M. Y. He, et al., Notch sensitivity and stress redistribution in three ceramic-matrix composites, J. Am. Ceram. Soc., 78(7), pp. 1719 (1995); DEN

[30] K. R. Turner, J. S. Speck, A. G. Evans, Mechanisms of deformation and failure in carbon-matrix composites subject to tensile and shear loading, J. Am. Ceram. Soc., 78(7), pp. 1841 (1995); DEN, CN, CH

[31] M. Hojo, S. Ochiai, N. Joyama, et al., Fracture mechanism of cross-ply carbon/carbon composites, ACM, 5(1), (1995); CT, 3-PSEB

[32] Y. Kogo, H. Hatta, H. Kawada, et al., Effect of stress concentration on tensile fracture behaviour of carbon-carbon composites, J. Comp. Mater., 32(13), pp. 1273 (1998); DEN, CH

[33] V. Kostopolous, Y. Z. Pappas, Notched strength prediction of centre-hole carbon/carbon composites, Mater. Sci. Eng., A250, pp.320 (1998); CH

[34] H. Hatta, Y. Kogo, H. Asano, et al, Applicability of fracture toughness concept to fracture

behaviour of carbon/carbon composites, JSME International Journal, A42(2), pp. 265 (1999); DEN, CT, 4PSEB

[35] D. Broek, The practical use of fracture mechanics, Kluwer Academic Publishers (1988)

[36] B. Lawn, Fracture of brittle solids – second edition, Cambridge University Press (1993)

[37] H. Tada, P. C. Paris, G. R. Irwin, The stress analysis of cracks handbook, Del Research Corporation (1973)

[38] cf. D. Broek, Elementary engineering fracture mechanics, 4th Edition (1985)
M. F. Kanninen, C. H. Poppelar, Advanced fracture mechanics, Oxford University Press (1985)
J. F. Knott, Fundamentals of fracture mechanics, Butterworths (1973)

[39] D. Broek, The practical use of fracture mechanics, Kluwer Academic Publishers (1988)

[40] A. G. Evans, F. W. Zok, Review, The physics and mechanics of fibre-reinforced brittle matrix composites, J. Mater. Sci., 29, pp. 3857 (1994)

[41] H. Hatta, Y. Kogo, H. Asano, et al, Applicability of fracture toughness concept to fracture behaviour of carbon/carbon composites, JSME International Journal, A42(2), pp. 265 (1999)

[42] V. Kostopolous, Y. Z. Pappas, Notched strength prediction of centre-hole carbon/carbon composites, Mater. Sci. Eng., A250, pp.320 (1998)

[43] J. M. Whitney, R. J. Nuismer, Stress fracture criteria for laminate composites containing stress concentrations, J. Comp. Mater., 8(7), pp. 253 (1974)

[44] H. Hatta, Y. Kogo, H. Asano, et al, Applicability of fracture toughness concept to fracture behaviour of carbon/carbon composites, JSME International Journal, A42(2), pp. 265 (1999)

[45] Y. Kogo, H. Hatta, H. Kawada, et al., Effect of stress concentration on tensile fracture behaviour of carbon-carbon Composites, J. Comp. Mater., 32(13), pp. 1273 (1998)

[46] A. Kiuchi, I. Iwata, N. Nakano, Proc. 4th Symp. High Performance Mater. for Severe Environments, pp. 37-45, (1993) Tokyo

3. Observation of crack extension

3.1 Introduction

As discussed in the introduction several different attempts have been made to explain the notch insensitive behaviour of C/C composites. These will be examined in the following section more in detail. One major concept leading to notch insensitive behaviour is the formation of "shear bands" as proposed by Evans et al.[47]. However, let us recall that there exist with mode I and mode II two types of fracture occurring in notched C/Cs depending on the fibre orientation.

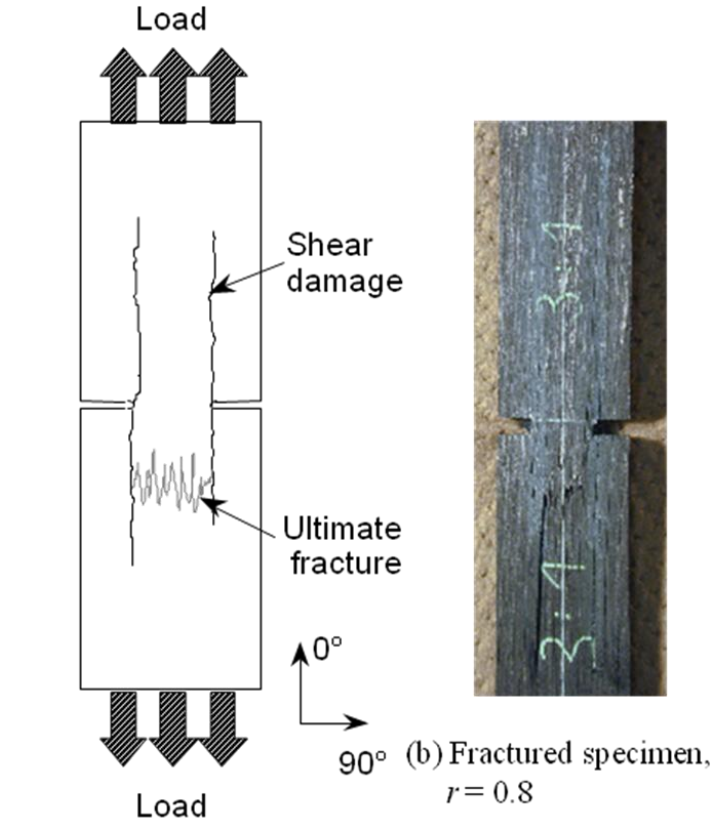

Fig. 3.1: Typical shear and ultimate tensile fracture patterns appeared in the DEN specimens when 0° ply fraction r is higher than 0.71 (a) and a fractured specimen at $\Upsilon = 0{,}8$ (b).

When sharp notches are introduced into uni-directionally reinforced C/Cs in direction normal to the fibre orientation, shear damage like that shown in Fig. 3.1 occurs. The shear damage easily extends from the notch tips in direction parallel to the fibres due to the extremely low shear strength. However, when sharp notches are introduced parallel to the fibre axis, cleavage type fracture without shear-damage is observed as for example shown in Fig. 2.2 on the left.

Thus, if various intermediate cases between the above two extremes are examined, the shear damage can be precisely observed and the effect of the shear damage on notch sensitivity can be clearly evaluated.

The procedure in this chapter was as follows: First, the basic tensile properties of C/C were examined. Then, based on the above concept, notched specimens with various 0° and 90°-layer ratios were fractured, and the shear damages in these specimens were observed. Thereafter, the relation between the shear damage obtained in this study and the "shear band" found in previous reports was compared. Finally, based on these results, the controlling mechanisms for the notch insensitivity of C/C composites are discussed.

3.2 Experimental procedure

3.2.1 Material

The carbon-carbon composite (C/C) used in the present and all following chapters was of a cross-ply laminate type, made by means of the preformed yarn process[48], and supplied by Across Co. Ltd. A primary feature of the preformed yarn process is the use of preformed yarns, PYs, as a source material of C/C. The PY consists of matrix source particles (coke and bulk mesophase powders) dispersed within the carbon fibre bundle and sheathed with a thin nylon sheet. In the C/C forming process, preformed sheets, in which the PYs had been uni-directionally aligned and tied by thin polymer threads, were stacked in a predetermined lamination pattern, set in a die, hot-pressed at 827 K for carbonization, and finally heat-treated at 2273 K for graphitization in an inert atmosphere. The C/C material was reinforced with high modulus carbon fibres, Torayca M-40, and the fibre volume fraction of the C/C material was always 50%. The C/Cs were composed of systematically changed ratios of 0° and 90° layers, as shown in Table 3.1. In the following, the specimens will be identified by the ratio of the 0° and 90° layers, as shown in the column of Table 3.1, where 0° was set to the loading direction in the fracture tests.

stacking sequence	number of plies			0° ply ratio *r*
	0° plies	90° plies	total	
UD 90	0	14	14	0
1:4	2	12	14	0.14
1:3	3	12	15	0.20
1:2	4	10	14	0.29
1:1	7	8	15	0.47
1:1	8	7	15	0.53
2:1	10	4	14	0.71
3:1	12	3	15	0.80
4:1	12	2	14	0.86
UD 0	14	0	14	1

Table 3.1: Examined stacking sequences.

3.2.2 Experiments

All mechanical tests were performed using a screw driven mechanical testing machine Autograph AG-5000A of Shimadzu Co. Japan under a crosshead speed of 0,1 mm/min unless noted otherwise.

3.2.2.1 Tensile properties

Owing to the importance of tensile strength, the influence of the specimen's geometry on the tensile fracture stress was first studied. Tensile tests were carried out using coupon and dog bone shaped specimens as shown in Fig 3.2. In order to determine the optimum geometry, the gage length was varied from 20 mm to 150 mm in the coupon (smooth) specimens, and the shoulder radius was changed in the "dog bone" specimens up to 100 mm. Strain gages were attached to both surfaces of the specimen parallel and normal to the loading direction in order to calculate the Young's modulus and the Poisson's ration. A screw driven testing machine, AG-5000 made by Shimadzu Seisakusho, Japan, was used for tensile loading of the C/C specimens. In order to investigate the effect of interfacial debonding stress τ_d on the ultimate tensile fracture strain ε_u fibre bundle push-out tests were carried out. In these tests several

different bulk densities were examined. The tests were carried out by use of a fibre bundle push-out test machine as described by Hatta et al.[49]

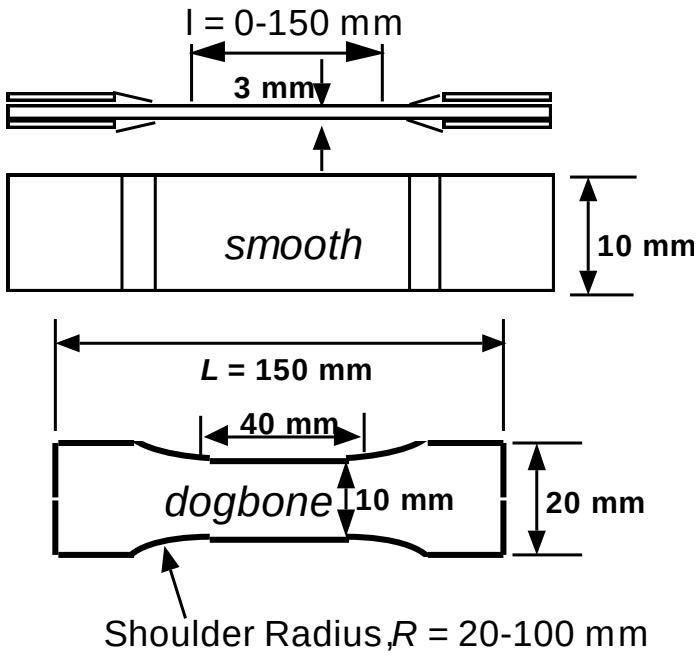

Fig. 3.2: Specimens for tensile test

3.2.2.2 DEN test

Notch sensitivity of the C/C composite was evaluated based on the test results of double-edge notched (DEN) specimens. The geometry of the DEN specimens is shown in Fig. 3.3. The two notches in the DEN specimens were introduced by a diamond wheel with a 0.2 mm tip radius. In previous studies, the DEN specimens of the present material revealed insensitivity to the notch tip radius when the radius was less than 1 mm[50,51,52]. Thus, the present results can be regarded the same as values of cases with ideal sharp notches. Shear damage (Mode II cracks) and its extension near the notch tips was monitored on the front and back sides using travelling microscopes with a 25x magnification. The net fracture stresses in the minimum cross section $\sigma_{f,net}$ and the critical energy release rate under the assumption of ideal sharp cracks were determined from the fracture load of the DEN tests. The critical energy release rates for mode I (G_{Ic}) and mode II (G_{IIc}) crack extensions were calculated in terms of ultimate fracture load for the mode I cracks and the onset loads for mode II cracks with the aid of finite element calculations.

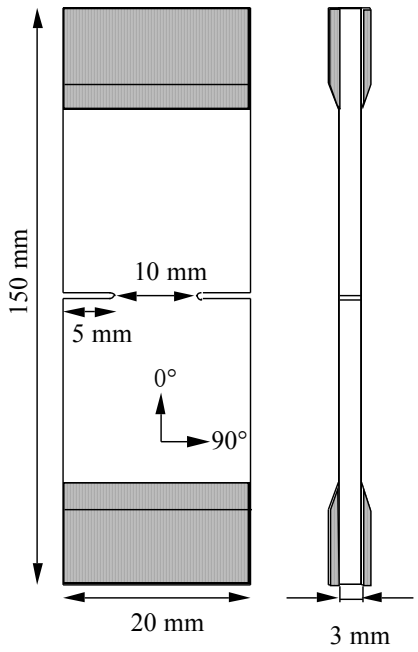

Fig. 3.3: Specimen dimensions of double-edge-notched (DEN) specimens

3.2.2.3 3-point bending tests of pre-loaded DEN tensile test specimens

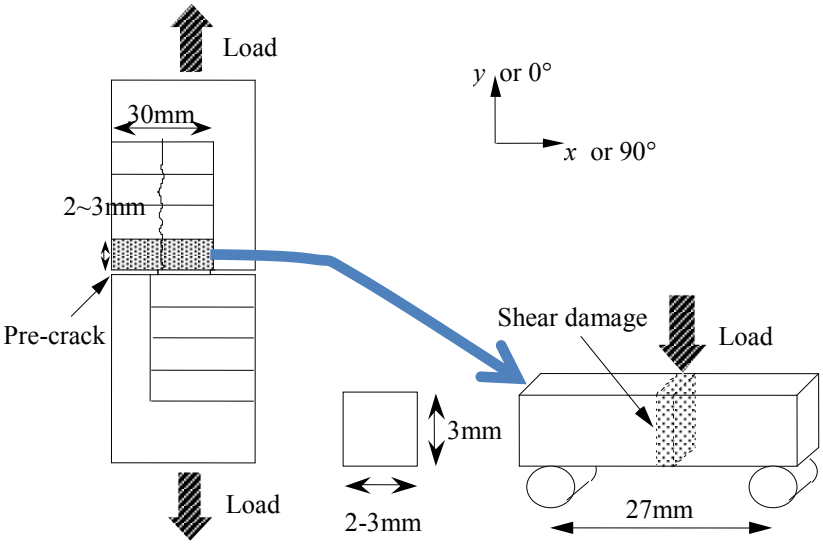

Fig. 3.4: Schematic drawing of 3-point bending tests after crack propagation for the evaluation of fibre fracture in shear-damaged regions.

In order to confirm fibre fracture in the shear-damaged region, special wide DEN

specimens (width = 40mm, notch length on each side = 15 mm) were prepared for materials with a 0° ply ratio $r > 0.7$. After the shear cracks propagated, small specimens with a length of 30 mm and a width of 2-3 mm were cut from DEN specimens, as shown in Fig. 3.4 Subsequently, three-point bending tests with a span/depth ratio of about 10 were conducted.

3.2.2.4 Compact Tension (CT) Tests

Compact Tension (CT) tests were carried out to observe clearly the shear crack extension behaviour and to obtain crack-propagation resistance curves (R-curves). The geometry of the CT specimens was based on the ASTM standard[53] and is shown in Fig. 3.5. The pre-crack was first introduced in the CT specimen by a diamond wheel with a thickness of 0,4 mm, and the final notch tip was then completed using a sharp knife edge. The crack extension length was determined using a travelling microscope from each side. For easy observation of the crack tip, the surfaces of the specimens were polished and thinly painted white. The crack opening displacement (COD) at the pre-crack tip was continuously monitored using a clip gage.

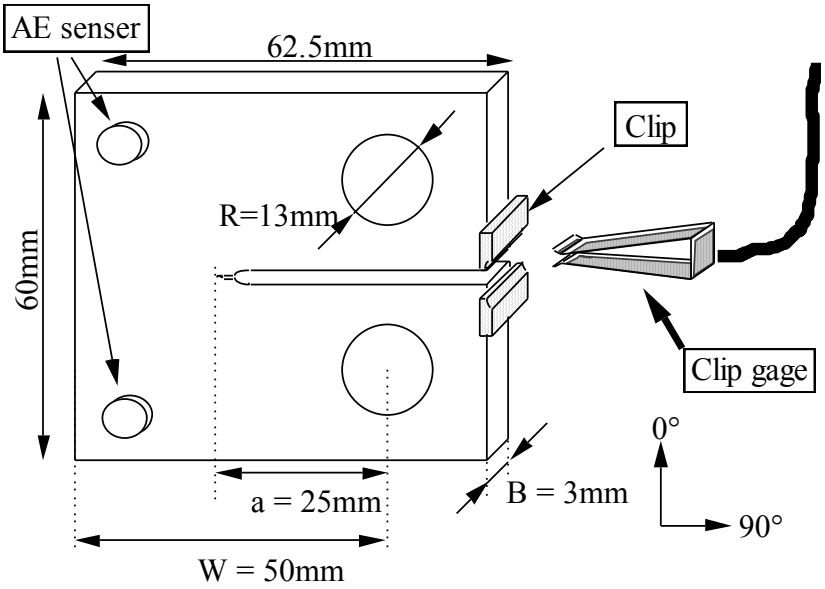

Fig. 3.5: Specimen geometry for compact tension (CT) tests

The crack extension resistance, G_R, under stable crack growth was determined using equation

$$G_R = \frac{p^2}{2B}\frac{dC_{pin}}{da} \tag{3.1}$$

where C_{pin}, P, a, and B are the compliance point, load, crack length, and specimen thickness respectively. Loading and unloading cycles were repeated to determine C_{pin} as a function of a. The observed crack length, a_{exp}, was found to be different from the calculated one, a_{calc}, which was determined from the compliance-crack length relation obtained by the finite element calculations. Using both, a_{exp} and a_{calc}, G_R was determined.

3.2.3 Finite element calculations

Finite element calculations were carried out to determine G_{Ic} and G_{IIc} from the DEN test results and the crack length in the CT tests using linear orthotropic material constants shown in Table 3.2. A commercial code of ABAQUS®, version 5.7.1, was used in these calculations under the assumption of plane stress fields using 8-node iso-parametric elements. The virtual crack-closure-force method[54,55] was used to calculate G_{Ic} and G_{IIc}.

Stacking sequence	E_1 [GPa]	E_2 [GPa]	ν_{12}	G_{12} [GPa]
UD90	200	3.65	0.00785	5.4
1:4	145	30.0	0.00913	5.4
1:3	141	38.7	0.00976	5.4
1:2	106	71.0	0.0109	5.4
1:1	104	80.1	0.0145	5.4
3:1	38.7	141	0.00976	5.4
UD0	3.65	200	0.00785	5.4

Table 3.2: Material constants for C/Cs used in FEM calculations

3.3 Results

3.3.1 Basic tensile test results of smooth CP 0/90 specimens

The tensile fracture stress obtained using smooth specimens with a changing gage length, l, and "dog bone" specimens with a changing shoulder Radius, R, are compared in Fig. 3.6 and Fig. 3.7, respectively. It was concluded from these figures that the tensile fracture stresses obtained using the various specimens were almost identical. Thus, the effects of the gripping and of the stress concentration from the curvature of the specimen shoulder are negligibly small. The fracture stress of all specimens ranged between 152 and 206 MPa with an average fracture stress of 186 MPa. In spite of insensitivity to stress concentration sources at the gripping or the shoulder radius, all tensile stress-strain curves were linear up to the ultimate fracture, as shown in Fig. 3.8.

This tendency is a well known characteristic of C/C composites[56,57] and differs greatly from that of ceramic matrix composites[58,59]. The Young's moduli E in x and y-direction were determined as

$E_{xx} = E_{yy} = 96.5$ GPa

and the Poisson ratio ν was found to be

$\nu_{12} = 0{,}026$.

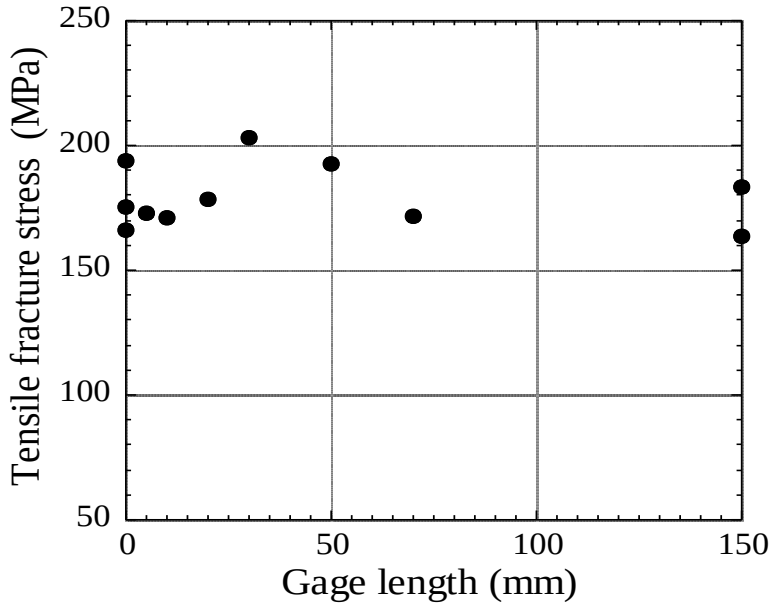

Fig. 3.6: Tensile fracture stress of smooth specimens with a changing gage length, l,

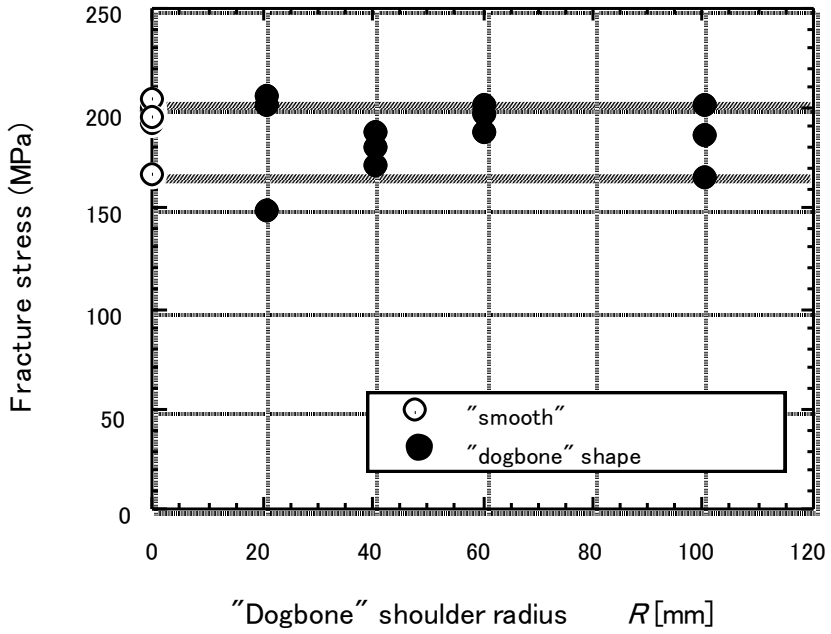

Fig. 3.7: Tensile fracture stress of "dog bone" specimens with a changing shoulder Radius, R,

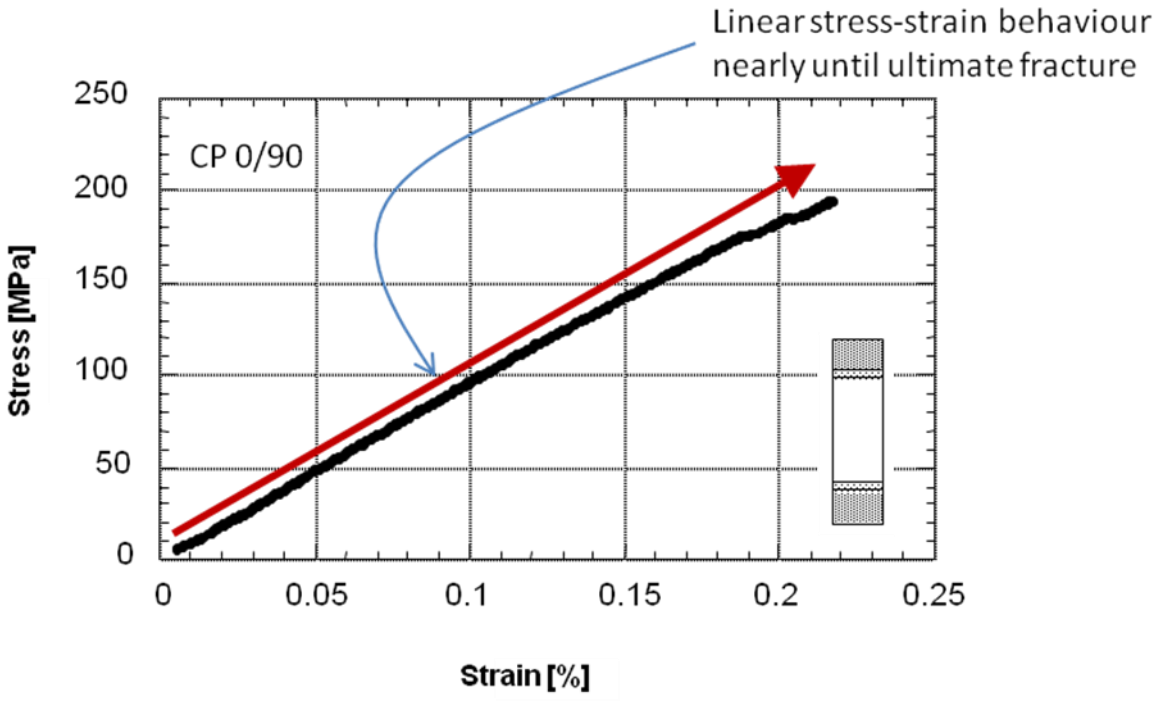

Fig. 3.8: Nearly linear tensile stress-strain behaviour of C/C composites

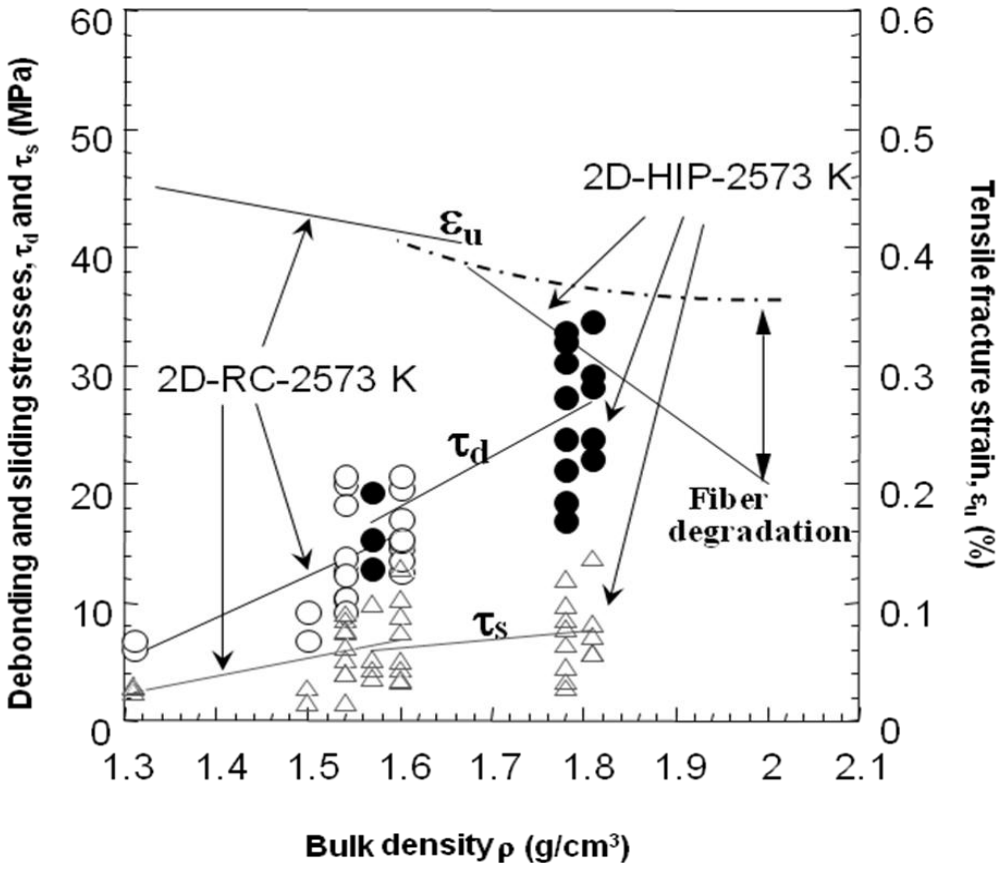

Fig. 3.9: Tensile fracture strain, e_u, interfacial debonding stress, t_d, and interfacial sliding stress, t_s, of the 2D-C/C composite as a function of bulk density, ρ.

Interfacial debonding stresses τ_d and ultimate tensile fracture strains ε_u are shown in Fig 3.9[60] as a function of the bulk density ρ. In this figure both, the interfacial debonding stress τ_d and the interfacial sliding stress τ_s increase with increasing bulk density ρ. At the same time the tensile fracture strain ε_u decreases with increasing ρ. Thus, we must conclude that high interfacial strength corresponds to low ultimate tensile fracture strains ε_u.

3.3.2 Results of smooth specimens with changing stacking sequence

All tensile stress-strain relations of the examined C/Cs remained linear up to ultimate fracture. This is a typical behaviour observed in most C/Cs[61].As expected, the tensile fracture strength increased linearly with the 0° ply fraction, *r*, as shown in Fig. 3.10 and the tensile fracture strain did not depend on *r*. The slightly higher values than expected from the solid line for r =1 might be due to the variations in the volume fraction of the fibre.

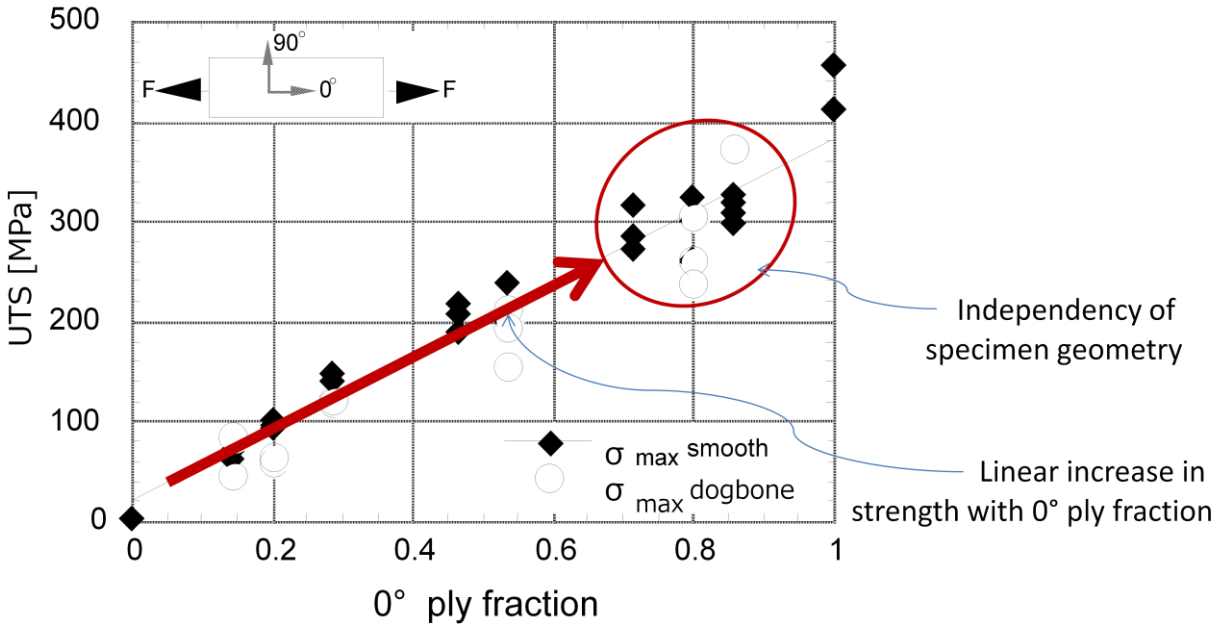

Fig. 3.10: Tensile fracture strength obtained using un-notched specimens as a function of the 0°-ply ratio.

3.3.3 Tensile test results of DEN type-specimens

The net fracture stresses of all materials obtained by the DEN tests are shown in Fig. 3.11 as a function of the 0° ply fraction, r. When $r \geq 0.71$, large scale shear fracture, as typically shown in Fig. 3.1, first appeared. In this case, the ultimate tensile fracture occurred at random in the region between the shear cracks. In contrast, when $r \leq 0.53$, shear cracks could not be identified before ultimate fracture, and catastrophic tensile fracture occurred between the pre-cracks. Note that the fracture load was proportional to r when $r \leq 0.53$. Thus, the critical stress intensity factor K_{Ic} is also proportional to r.
In Fig. 3.11, the tensile strengths obtained from the un-notched specimens, shown by "X" symbols and a solid line coincide with the net fracture stresses of the DEN specimens in the region of $r \geq 0.71$. These results suggest that once the shear fractures are formed, the effect of the material outside of the shear cracks is negligibly small regarding the stress distribution in the region between the shear cracks. In contrast, the net fracture stresses at $r \leq 0.53$ were slightly lower than the tensile strength due to the influence of stress concentrations.

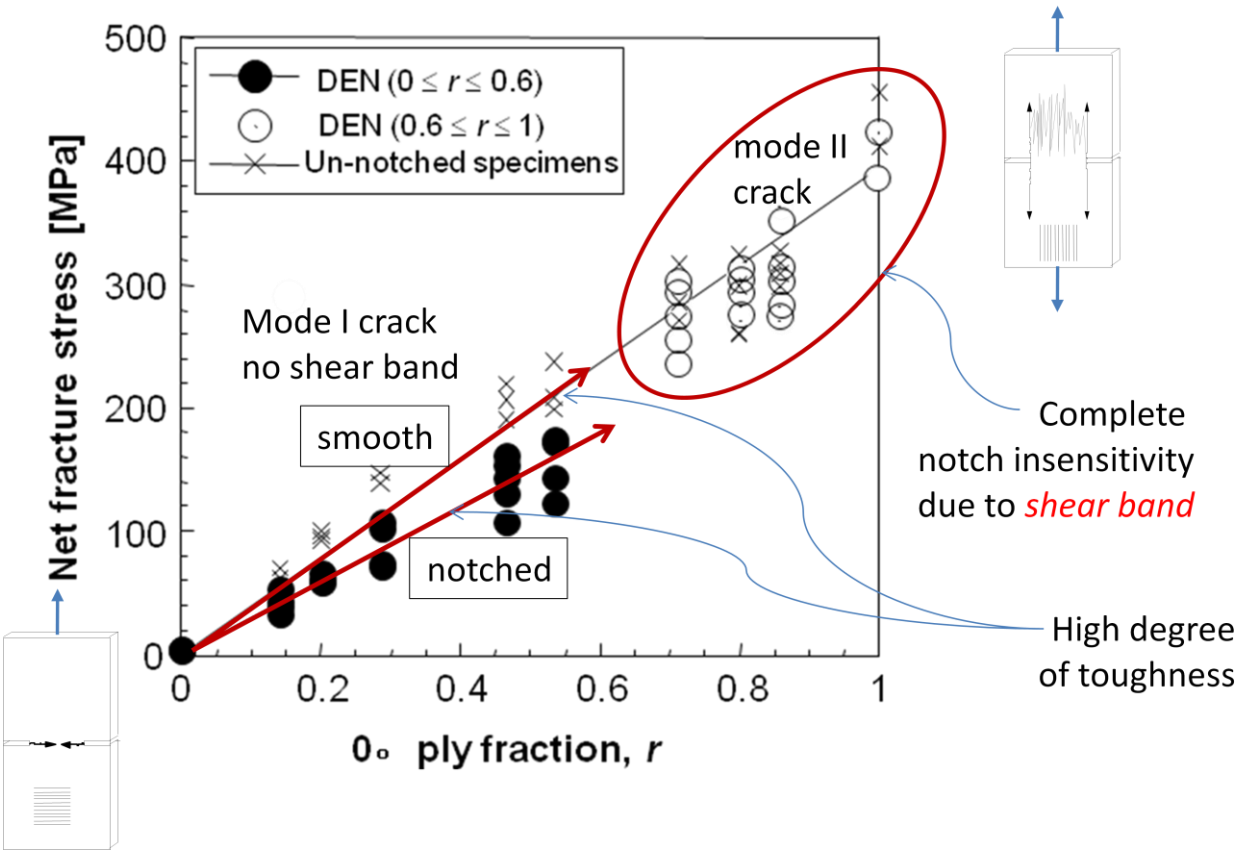

Fig. 3.11: Net fracture stresses of DEN and un-notched specimens.

Optical inspection of the shear cracks by travelling microscope revealed that the shear cracks originated often in transverse cracks from the cooling stage. As load increased splitting cracks appeared ahead of the crack tip as shown in Fig. 3.12. Several of these splitting cracks formed a band in a straight line ahead of the crack in direction parallel to loading. Each of the splitting cracks was arranged at an angle of around 45° to the tensile direction. When the load increased further, the crack grew into the splitting cracks and new splitting cracks appeared ahead of the splitting crack band.

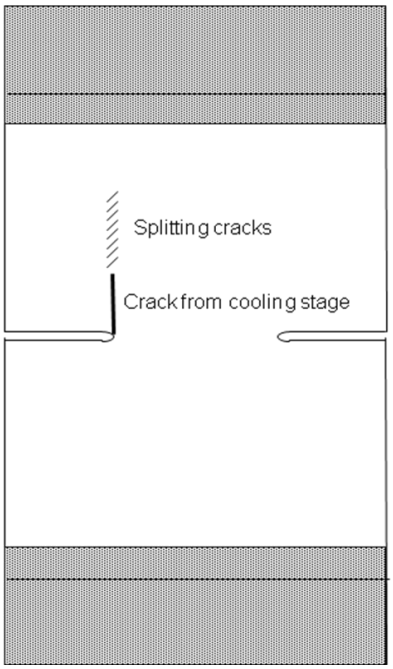

Fig. 3.12: Splitting crack formation.

A typical relation between the shear crack length and the net tensile stress obtained in a DEN test is shown in Fig. 3.13 for the CP 3:1 specimen. In this figure, the lengths of the four shear cracks observed from the front and the back sides are included. Once a shear crack began to propagate, the stress distribution became asymmetric around the centreline of the specimen. This facilitated further extension of the existing shear crack. Consequently, the crack lengths had a large amount of scattering. Physically meaningful data in Fig. 3.13 is only the initiation of the shear crack.

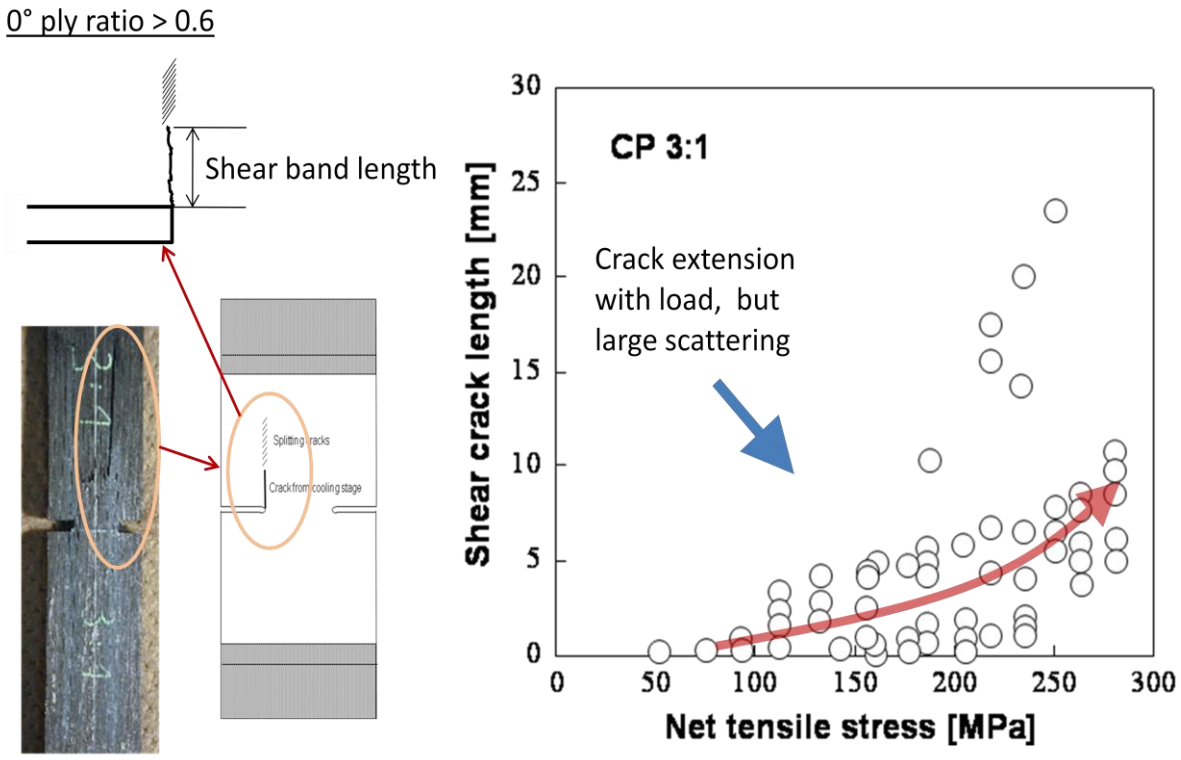

Fig. 3.13: Typical relation between net tensile stress and shear-crack length for the 3:1 specimen.

In Fig. 3.14, the initiation load of the shear crack is plotted as a function of the 0° ply fraction, *r*. In the DEN tests, the shear cracks grew rapidly, and their initiation was rather difficult to identify during the tests. Thus, the plots in Fig. 3.14 were determined by extrapolation of the existing data, such as those shown in Fig. 3.13, to the horizontal axis. In Fig. 3.14, the tensile stresses at crack initiation, shown as black squares, decrease nearly linearly with *r*. The grey squares and blue line show the tensile stresses at crack initiation when the Evans formula for crack extension is employed. The relationship is similar to our experimental results but Evans et al. determine crack initiation at substantially lower tensile stresses. The shear band length in *italic* describes the shear band extension length according to Evans at crack initiation of our specimens. Evans' crack length is at this stage around 1.5 – 4 mm long. Considering the large scattering, our observations are in very good agreement with the Evans' calculations, which at this stage do not have a linear but parabolic relationship.

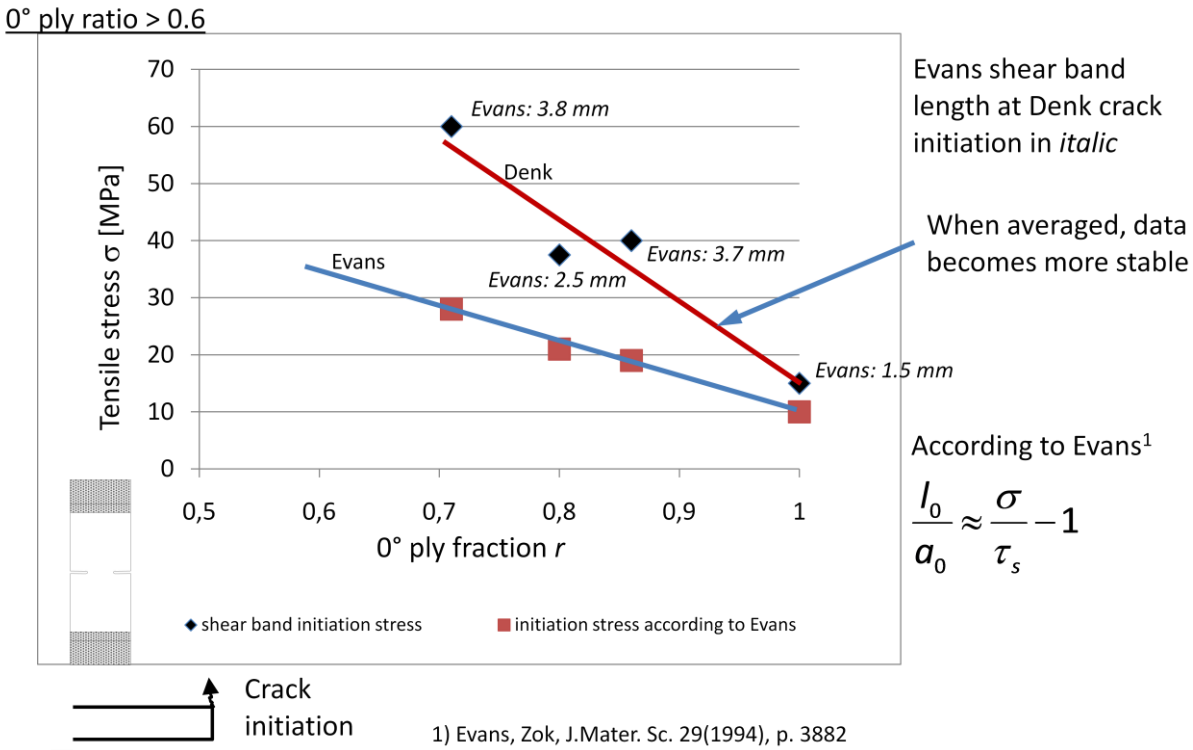

Fig. 3.14:Onset load of shear damage obtained by the DEN tests as a function of the 0° ply fraction *r*.

3.3.4 3-point bending test results of preloaded DEN-type specimens

In order to evaluate the shear crack effect, the type of damage must be identified. To confirm fibre fracture in the shear cracks, three point bending tests, using the specimen's cut out after the DEN tests, were carried out, as shown in Fig. 3.4. Typical results of such bending tests are shown in Fig. 3.15 for two CP 4:1 specimens, No. 1 and No.2, in which x = 0 represents the location of the pre-cracks. The areas in which shear cracks extend in the specimens are indicated at the top of the figure. As can be seen the bending strength of specimens with shear cracks is nearly the same as that without damage. This indicates that the fibres bridging the shear cracks were not seriously damaged.

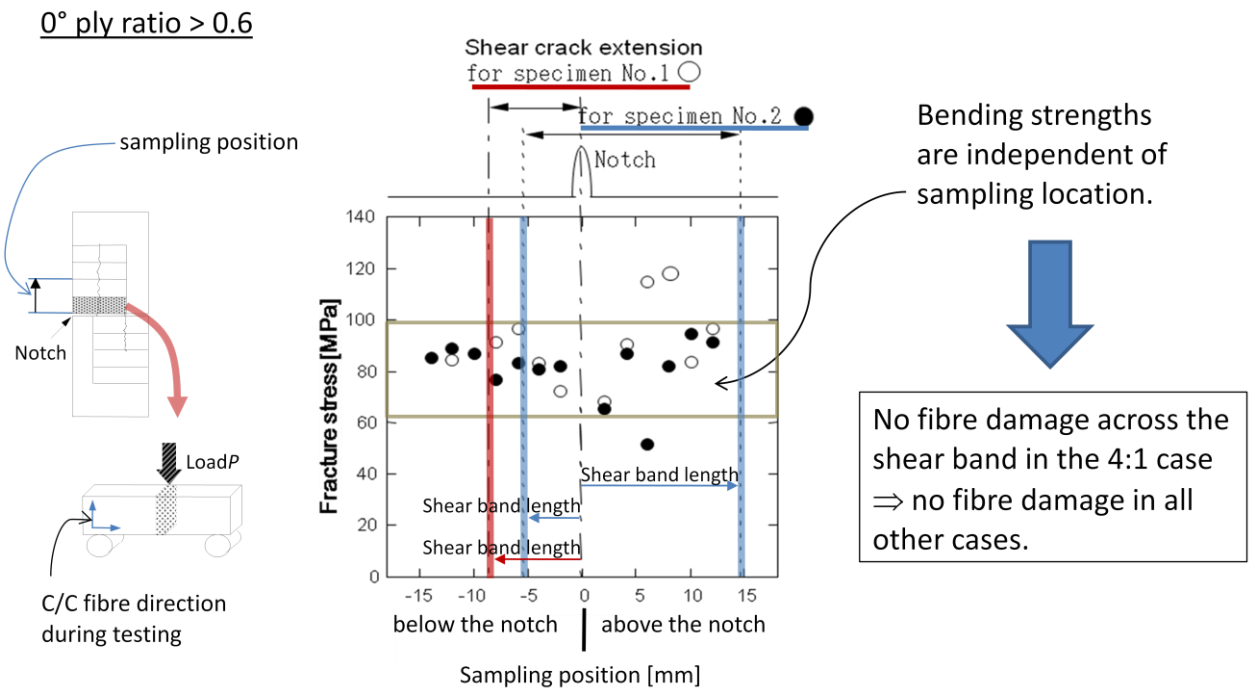

Fig. 3.15: Fracture stresses obtained by three-point bending tests using small specimens cut from 4:1 specimens with shear damage near the notch tips as a function of the sampling position. The sampling position describes the original distance of the cut-out specimen from the notch tip of the previous DEN specimen.

3.3.5 Tensile test results of CT–type specimens

In the CT tests, the same fracture modes as those in the DEN tests were observed; i.e., the mode I crack extension occurred for $r \leq 0.53$, and mode II for $r \geq 0.71$. One difference from the DEN tests was that the CT tests exhibited stable crack growth, and crack extension behaviour could be observed clearly. Typical crack extension resistance (R-) curves for mode I and II crack propagation are shown in Fig. 3.16 and Fig. 3.17 respectively as a function of the crack extension length, a. In this figure, the R-curves were determined

(1) based on the crack lengths by means of direct observations, the micro-crack initiation for mode I, a_{exp}, and in case of the CP 0/90 by

(2) FEM calculations based on the experimentally determined compliance, a_{calc}.

Since only a part of the fibres fractured in the micro-cracked regions and a_{calc} was estimated under implicit assumption of complete fibre fracture, the R-curves based on a_{calc} were thought to be more physically meaningful and a_{calc} will be used in the following discussion.

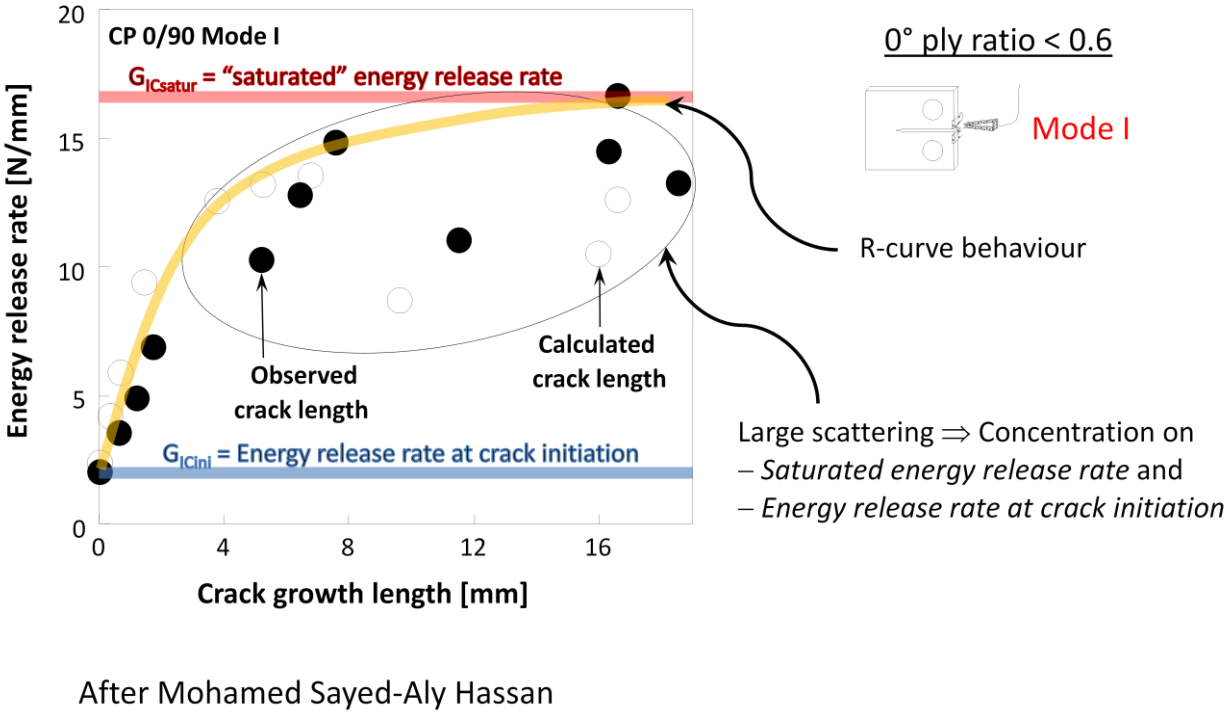

Fig. 3.16: Mode I crack extension resistance (R-) curves of CP 1:1 specimen

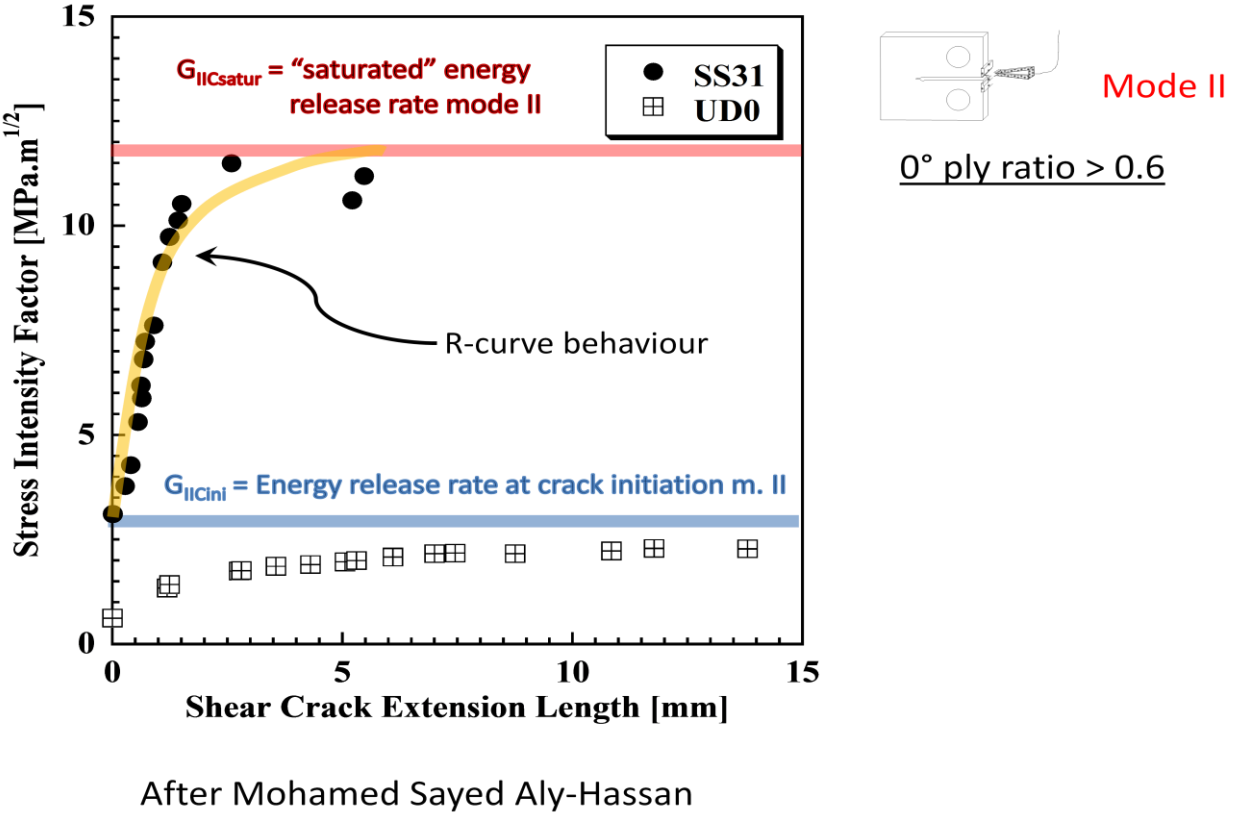

Fig. 3.17: Mode II crack extension resistance (R-) curves of UD 0° specimen

As shown in Figs. 3.16 and 3.17, both the mode I and II cracks show typical R-curve behaviour, i.e., the crack extension resistance *R* increased with crack length. Similar R-curve behaviour has been already reported for mode I fracture[62,63]. As can be seen from these figures, the energy release rates reveal large scattering. Thus, in the following, the discussion will concentrate on the energy release rate at *crack initiation*, G_{ICini}, shown in Fig. 3.16 as blue line and on the energy release rate of a saturated crack, $G_{ICsatur}$, shown in Fig. 3.16 as red line for mode I and equivalent for mode II.

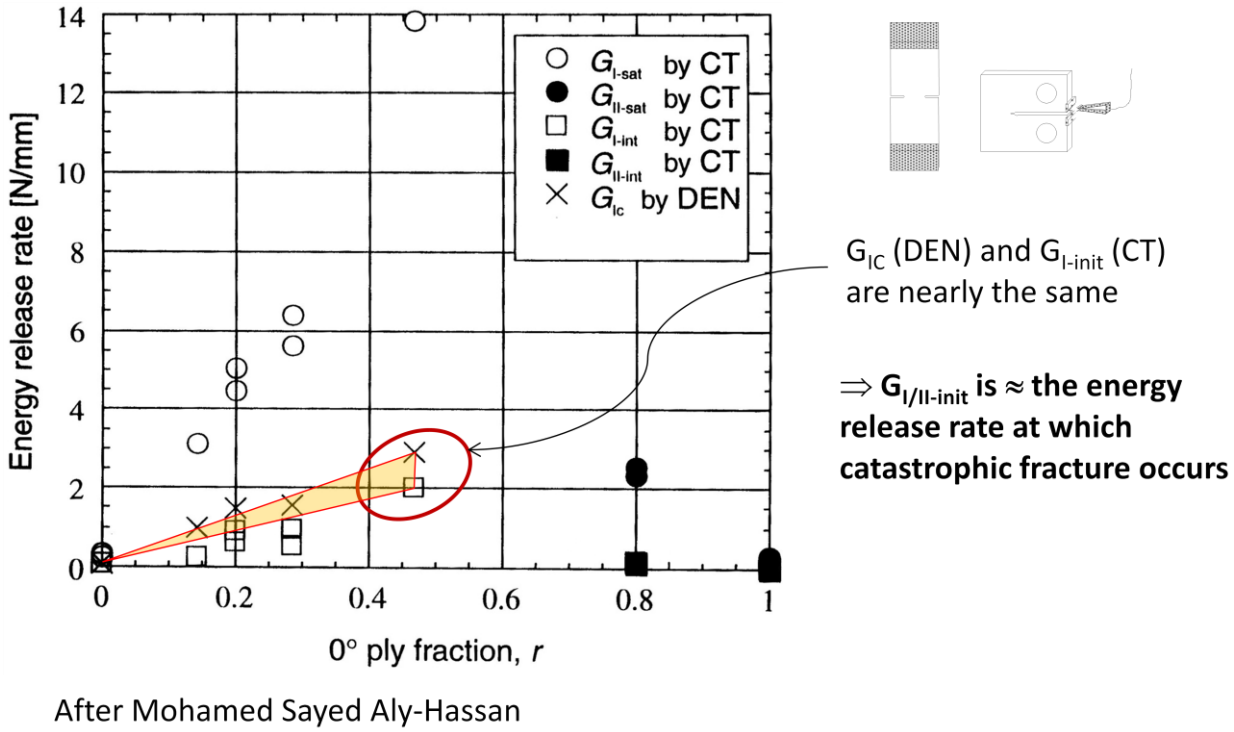

Fig. 3.18: Initiation and saturation crack extension resistances determined for mode I and mode II fractures by CT tests compared with the critical energy release rates obtained by DEN tests, G_{Ic}.

In Fig. 3.18**,** the initial values and the saturated values of R-curves obtained by Compact Tension tests are plotted as a function of *r*. In this figure, the critical energy release rates under mode I, G_{Ic}, obtained by DEN tests were also plotted. These values were calculated by finite element method using the ultimate fracture loads of the DEN results for $r \leq 0.53$. As shown in Fig. 3.18, G_{Ic}s at $r \leq 0.53$ (symbols X) coincide quite well with the initiation values of the *R*-curves. Thus, the energy release rate at crack

initiation of the CT test is approximately equivalent with the critical energy release rate of the corresponding DEN case. Consequently, the DEN specimen fails under mode I approximately at crack initiation because the loading condition does not allow stable crack growth before ultimate fracture. In case of the CT test on the other hand, the test configuration allows stable crack growth and thus, the energy release rate at final fracture is much higher. Thus, the *same* C/C material can fracture at two different energy release rates, $G_{I\text{-}init}$ and $G_{I\text{-}sat}$, depending on the actual loading conditions.

Next, using these *R*-curve values, crack extension loads for the DEN specimens were calculated, and these results were compared with experimental values of the DEN tests, as shown in Fig. 3.19. As expected from the above, the observed DEN fracture loads are slightly higher than the calculated loads on the basis of initiation and are substantially lower than the values at saturation of the *R*-curves. A possible explanation for the low G_{Ic} values of the DEN specimen with respect to the saturated *R*-curve values of the CT specimens is that the mechanism providing *R*-curve behaviour takes a finite amount of time. When the specimens fail catastrophically, time is too short to generate R-curve behaviour so that the DEN specimens fail near the initiation point.

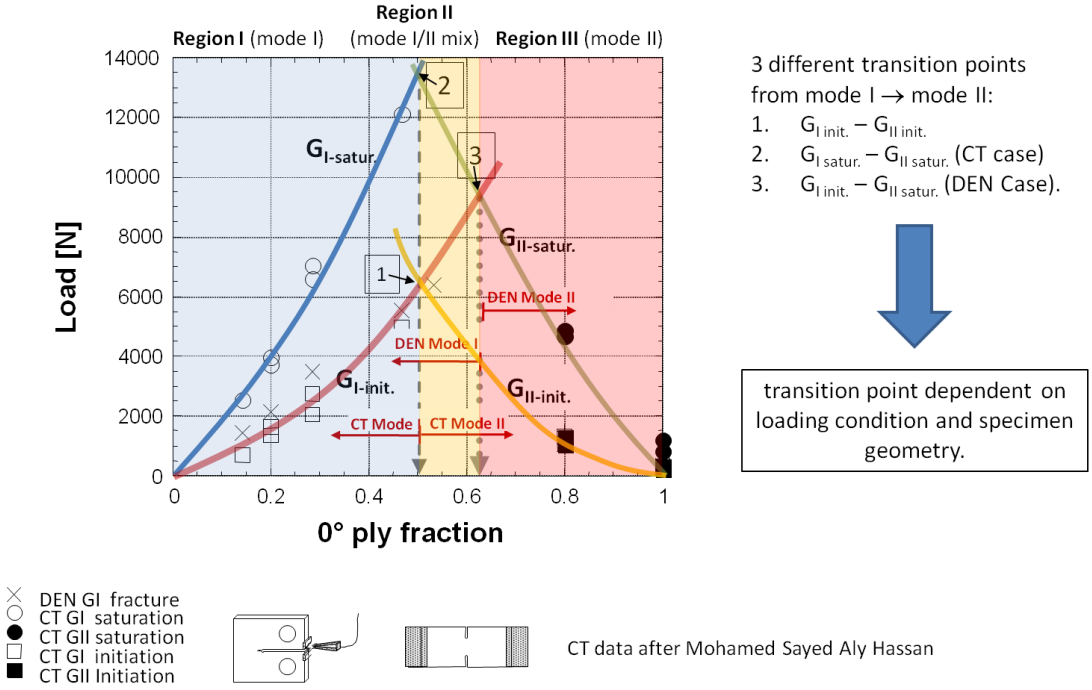

Fig. 3.19: Ultimate fracture loads in mode I fracture and crack initiation loads in mode II fracture determined by DEN tests compared with DEN loads at the initiation and saturation of crack extension resistance obtained by CT tests.

3.4 Discussion

3.4.1 Transition from mode I to mode II fracture

Next, using the CT's *R*-curve values at crack initiation and saturation, G_{ICini} and $G_{ICsatur}$, theoretical crack initiation and crack saturation loads were calculated for a DEN specimen, and these results were added to the experimental values of the DEN tests, as shown in Fig. 3.19. As pointed out in the section 3.3.5 DEN test results shown in Fig. 3.19 are located very close to the initial values of the CT test specimens. This observation indicates that the initial and saturated values of the CT test results may function as upper and lower boundaries for the ultimate fracture of C/C specimens. In particular the C/C material may fail at saturated energy release rates of the CT specimens if slow and stable crack growth occurs prior to ultimate fracture. On the other hand, the specimens fail close to the much lower CT's initial energy release rate $G_{Ic}i$ if ultimate fracture occurs catastrophic as observed in the DEN case. Thus, the initial and saturated CT test results under mode I and II of Fig. 3.19 will be used in the following discussion.

Depending on the loading conditions, catastrophic fracture or stable crack growth may occur under mode I and/or mode II. Thus, the following 3 different cases must be considered:

Case 1: Stable crack growth before ultimate fracture does neither occur under mode I nor under mode II. Instead, the specimen fractures under mode I and II catastrophically, thus the extremely low energy release rates at crack initiation, $G_{Ic}i$ and $G_{IIc}i$, must be considered. The corresponding transition point is marked by "Case 1" in Fig. 3.19. As shown in this figure, the fracture load is the lowest of all cases. The transition point is located at $r \approx 0.5$. At 0° ply fractions lower than 0.5, fracture will occur first under mode I.

Case 2, marked by "Case 2" in Fig. 3.19, represents the opposite of case 1. In this configuration the specimen develops a stable crack growth before final fracture. Final fracture occurs under mode I if r is roughly less than 0.5 while mode II fracture will occur approximately at $r \geq 0.5$. This case corresponds to the examined CT specimens.

In case 3 marked by "Case 3" in Fig. 3.19, the specimen fractures catastrophically under mode I and after formation of stable crack growth under mode II. Thus, the energy release rates at crack initiation under mode I, $G_{Ic}i$, and at crack saturation under mode II, $G_{IIc}s$, must be examined. In this configuration initial cracking may occur under mode II but final fracture occurs catastrophically under mode I if r is less than roughly 0.6. In

case of r ≥ 0.6, the specimen will fail first under mode II after stable crack propagation. This case corresponds to the examined DEN specimens.

3.4.2 Shear bands

As pointed out in the previous chapter, the transition from mode I to mode II cracking depends on the specimen geometry and the loading condition, which either permits or does not permit stable crack growth prior to ultimate fracture.
The fracture of the C/C composites can be separated into 3 distinct regions.

Region I: The specimen fractures under pure mode I. The crack propagates on top of a transverse crack originating from the C/C's cooling stage in a straight line without any deflection as shown in Fig. 3.20. This fracture pattern occurs in the region $r < 0.5$.

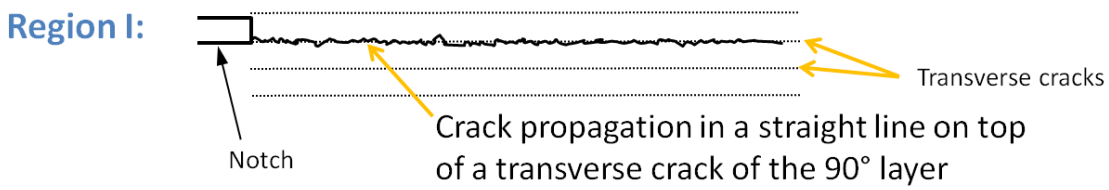

Fig.3.20: Crack propagation under mode I

Region II: Region II defines a transition region in which a crack might deflect several times from mode I to mode II and vice versa before ultimate fracture. Final fracture might occur either under mode I or mode II. This fracture pattern occurs in the region $0.5 < r < 0.6$. Fig. 3.21 shows the crack propagation of a CT specimen in cross-ply 0/90 configuration. The main crack propagation in this configuration is under mode I. However, the crack deflects several times under mode II due to R-curve behaviour prior to ultimate fracture under mode I. Careful observation revealed that damage began as longitudinal crack (splitting) in the vicinity of the notch tips as shown in Fig. 3.21. The splitting was much shorter than the shear cracks shown in Fig. 3.22, and was identified as widely opened transverse cracks. The transverse cracks were induced during the cooling stage after processing of the C/Cs, and could be observed in 0° and 90° plies.

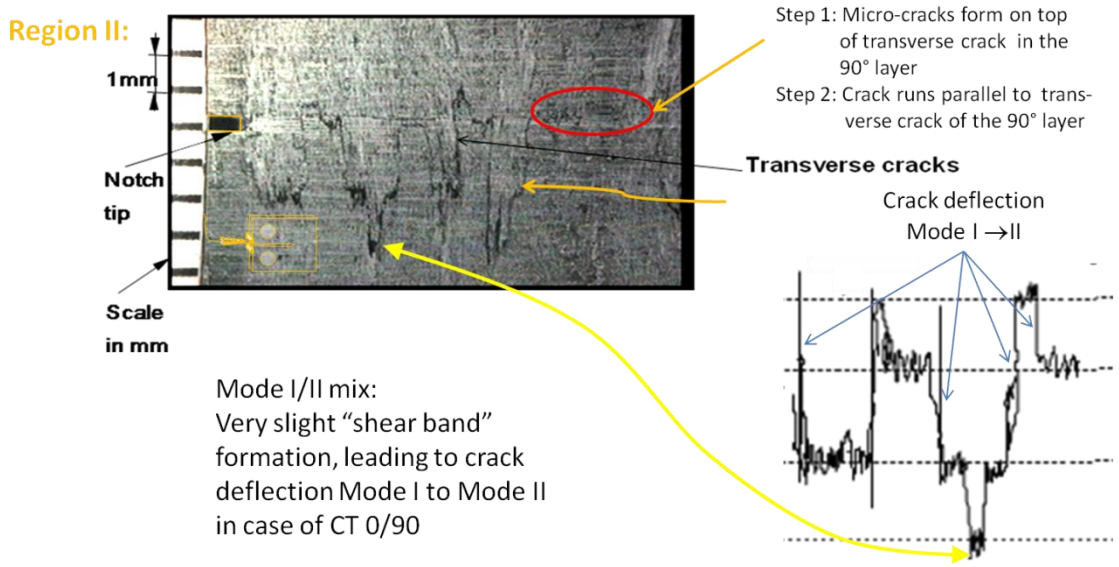

Fig.3.21: Crack propagation in the transition Region II.

Region III: The specimen fractures under pure mode II. The crack propagates on top of a transverse crack originating from the C/C's cooling stage in a straight line without any deflection as shown in Fig.3.22.

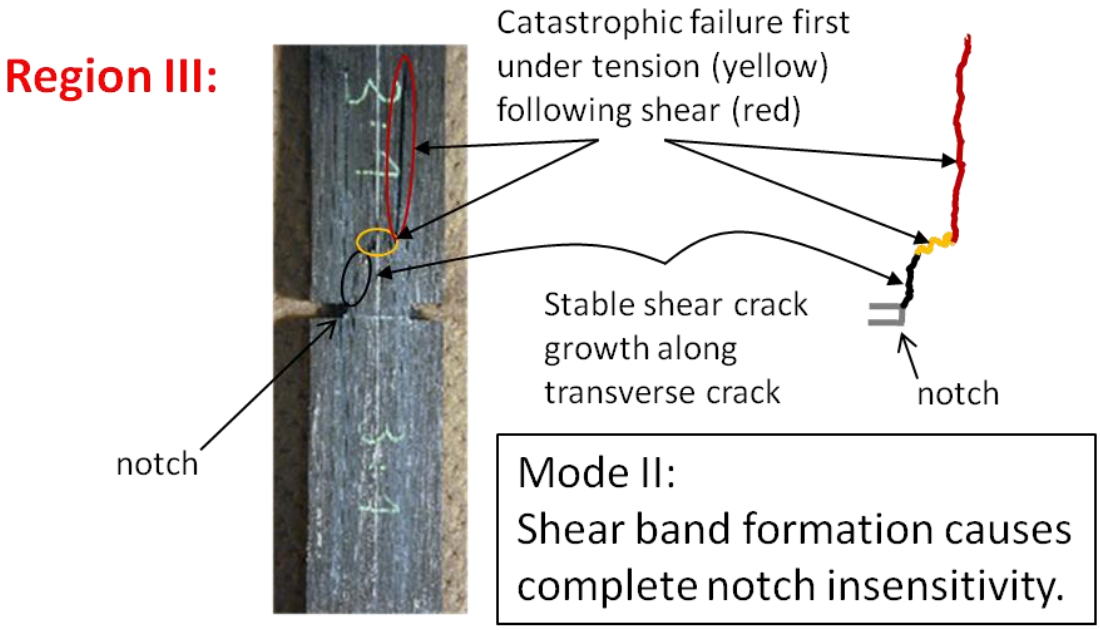

Fig.3.22: Crack propagation under mode II

We can conclude that transition from mode I to mode II depends on the specimen

geometry and loading condition. Clear mode I fracture will occur if $r < 0.5$. Above $r \approx 0.6$, fracture occurs under mode II. The range $0.5 < r < 0.6$ describes a transition region in which crack deflection might occur several times before ultimate fracture under mode I or II.

3.5 Conclusion

Fracture-toughness tests for C/Cs with 0°/90° lamination and with various ply ratios *r* were carried out, and the fracture behaviour of the specimens was compared. From these results, we drew the following conclusions:

1. The fracture mode of DEN-C/Cs with 0°/90° lamination changed from mode I to mode II when the 0° ply fraction *r* increased.
2. Three distinct regions can be identified, which are called region I, II and III.
3. Region I: The crack propagates under pure mode I on top of a transverse crack of the 90° layer. This fracture phenomenon occurs if $r < 0.4$.
4. Region II: Transition region in which mode I or mode II fracture may occur. Also, the crack might be deflected several times before ultimate fracture. This fracture phenomenon occurs if $0.5 < r < 0.6$.
5. Region III: The crack propagates prior to ultimate fracture at first under pure mode II. Final fracture occurs in the net section between 2 cracks under tension (mode I). The damage in the shear band region is rather slight. Serious fibre fracture does not occur. This fracture phenomenon occurs if $r > 0.6$.
6. Mode I fracture stresses obtained by DEN tests could roughly be estimated from the initial fracture toughness determined by CT tests.
7. The change in fracture mode from I to II caused by changing the 0°-ply fraction can be explained in terms of fracture toughness.
8. The main source of notch insensitivity in C/C composites was damage near the notch tips, which consisted of two kinds of cracks, splitting and tensile micro-cracks.
9. Mode I fracture in laminated C/Cs proceeded in the following order: splitting near the notch tips, accumulation of micro-cracks between the splitting, and finally, fibre bundle fracture.
10. Mode II fracture in laminated C/Cs proceeded in the following order: splitting near the notch tips, and extension of shear cracks from the splitting.

[47] A. G. Evans, F. W. Zok, Review, The physics and mechanics of fibre-reinforced brittle

matrix composites, J. Mater. Sci., 29, pp. 3857 (1994)
[48] A. Okura, T. Chou, Advanced Composites in Emerging Technologies, 348-353, (1992)
[49] H. Hatta, T. Aoki, I. Kawahara, Y.Kogo, I.Shiota, Tensile strength of Carbon/Carbon Composites I:Effect of Density and Interfacial Strength, J. Compos. Mater., 38(19) 1667-1689 (2004)
[50] Y. Kogo, H. Hatta, H. Kawada, et al., Effect of stress concentration on tensile fracture behaviour of carbon-carbon Composites, J. Comp. Mater., 32(13), pp. 1273-1294 (1998)
[51] H. Hatta, Y. Kogo, H. Asano, et al, Applicability of fracture toughness concept to fracture behaviour of carbon/carbon composites, JSME International Journal, A42(2), pp. 265 (1999)
[52] K. Goto, H. Hatta, H. Takahashi, H. Kawada, Effect of shear damage on the fracture behaviour of C/C composites, J. Am. Ceram. Soc. 84(6) 1327-1333 (2001)
[53] ASTM standard e-399-72
[54] E.F. Rybicki, M.F. Kanninen, Engineering Fracture Mechanics, 9, 931-938 (1977)
[55] K.N. Shivakumar, P.W. Tan, J.C. Newman, International Journal of Fracture 36, (1988)
[56] Y. Kogo, H. Hatta, H. Kawada, et al., Effect of stress concentration on tensile fracture behaviour of carbon-carbon Composites, J. Comp. Mater., 32(13), pp. 1273 (1998)
[57] H. Hatta, K. Suzuki, T. Sigei, S. Somiya, A. Sawada, Strength improvement by densification of C/C composites, Carbon, 39, 83-90 (2001)
[58] A. G. Evans, F. W. Zok, Review, The physics and mechanics of fibre-reinforced brittle matrix composites, J. Mater. Sci., 29, pp. 3857-3896 (1994)
[59] M.D. Thouless, O. Sbaizero, L.S. Sigl, A. Evans, J. Am. Ceram. Soc., 72(4), pp. 525-532 (1989)
[60] H. Hatta, T. Aoki, I. Kawahara, Y.Kogo, I.Shiota, Tensile strength of Carbon/Carbon Composites I:Effect of Density and Interfacial Strength, J. Compos. Mater., 38(19) 1667-1689 (2004)
[61] H. Hatta, K. Suzuki, T. Sigei, S. Somiya, A. Sawada, Strength improvement by densification of C/C composites, Carbon, 39, 83-90 (2001)
[62] K. Goto, H. Hatta, H. Takahashi, H. Kawada, Effect of shear damage on the fracture behaviour of C/C composites, J. Am. Ceram. Soc. 84(6) 1327-1333 (2001)
[63] H. Hatta, Y. Kogo, H. Asano, et al, Applicability of fracture toughness concept to fracture behaviour of carbon/carbon composites, JSME International Journal, A42(2), pp. 265 (1999)

4. Shear Properties of C/C composites

4.1 Introduction

As pointed out in section 2.2, shear damage in the form of shear band is considered to play an important role as a stress relaxation mechanism particularly in case of the uni-directionally reinforced C/C composite. According to the shear band theory, shear damage is supposed to play the most important role in all other configurations. In order to understand the effect of shear band formation and its effect, a deep understanding of the C/Cs shear failure is indispensable. The following chapter serves this purpose.

In spite of the importance of the shear properties, rather little has been reported in the literature regarding the material failure, e.g. the damage of fibres and matrix, and the inter-laminar failure of C/C composites. Manocha et al.[64] and Oh et al.[65] directly examined the inter-laminar shear properties of C/C composites using the short beam method. In these tests, the inter-laminar shear strength of a C/C composite was found to be extremely low. Anand et al.[66] used a testing apparatus which roughly resembles the Iosipescu test fixture, and examined weaved fabric C/C in contrast to the here tested laminates composed of uni-directionally reinforced lamina. Brønstedt et al.[67] discussed shortly the fracture mechanism under shear. However, there is still no comprehensive knowledge about the fracture mechanisms under shear loading.

In this chapter, an attempt was made to clarify the sequence of failure during the in-plane shear tests of C/C composites to obtain precise input data for a later numerical simulation of the shear band effect. To do so, the adequacy of several shear testing methods was at first examined. Then, using the chosen test method, the in-plane shear failure mechanisms were discussed for C/C specimens with a 0°/90°-fibre orientation but changing ratio of 0° and 90° layers. A second purpose of this chapter is the generation of sufficient shear input data for a following FEM simulation of shear damage and its effect on the stress concentration at stress concentration sources like holes or notches.

4.1 Experimental Procedure

4.1.1 Material

The carbon-carbon composites used in this chapter were produced by the preformed yarn process[68], and supplied by Across Co. Ltd. They consisted of lamina

with fibres placed in either 0° or 90° direction. However, the ratio of the 0° and 90° plies changed as tabulated in Fig. 4.1. As shown by example for the 1:3 stacking sequence in Fig. 4.2, the stacking sequences were symmetric. To identify these materials, the ratio of the number plies with fibres in 0° relative to the specimen's total plies, i.e., the 0° ply ratio v(f), was used as shown in the last column in Fig. 4.1. Occasionally, we also used the stacking ratio, denoted in the 1st column in Fig. 4.1 as "stacking sequence". The total thickness of the material varied between 3 and 3.3 mm depending on the stacking sequences. The reinforcing fibres were PAN based high modulus type TORAYCA® M40 with 6000 fibres per bundle and the fibre volume fraction was in all cases 50%.

stacking sequence	number of plies			0° ply ratio
	0° plies	90° plies	total	
UD 90	0	14	14	0
1:4	2	12	14	0.14
1:3	3	12	15	0.20
1:2	4	10	14	0.29
1:1	7	8	15	0.47
1:1	8	7	15	0.53
2:1	10	4	14	0.71
3:1	12	3	15	0.80
4:1	12	2	14	0.86
UD 0	14	0	14	1

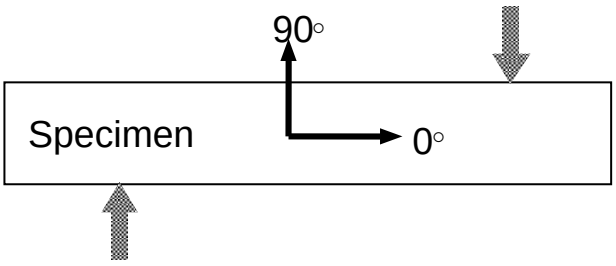

Fig. 4.1: Examined stacking sequences

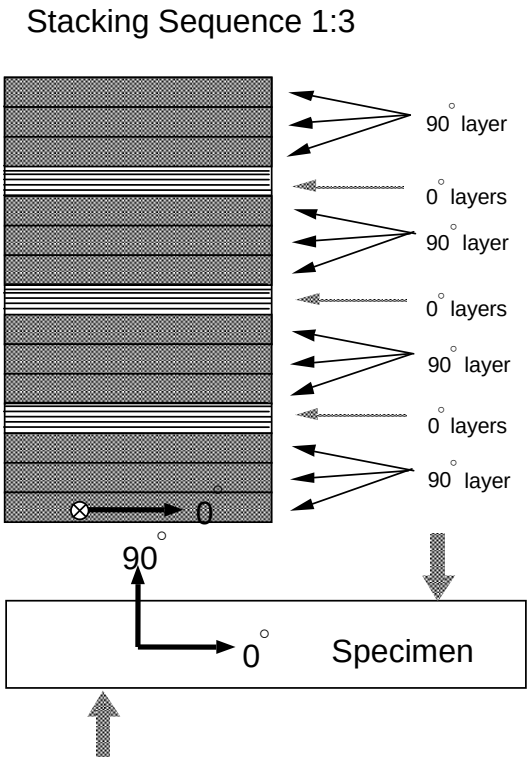

Fig. 4.2: Example of a 1:3 stacking sequence

4.1.2 Shear Tests

Among the shear tests which were introduced for the testing of composite materials, the Iosipescu[69,70,71,72,73,74,75,76,77,78,79], the ±45° tensile and the 10° off-axis[80,81,82,83,84] tests have been shown to be superior[85] in terms of data accuracy and cost effectiveness. However, to our knowledge, all existing data concerning in-plane shear properties of C/C composites was generated using the Iosipescu test. Thus, the three tests have never been comparatively examined using a C/C composite.

4.1.2.1 Iosipescu Test

The test fixture for the Iosipescu shear test is shown in Fig. 4.3. During this test, a constant displacement rate of 0.1 mm/min was applied on the right side of the specimen which generated a pure shear stress in the centre portion between the v-notches. The specimen for the Iosipescu test consisted of a rectangular coupon, in which v-shaped

notches with an angle of 110° were engraved on both sides as shown in Fig. 4.4. Strain gages were attached between the notches in the centre at angles of ±45° to the loading (90°) axis.

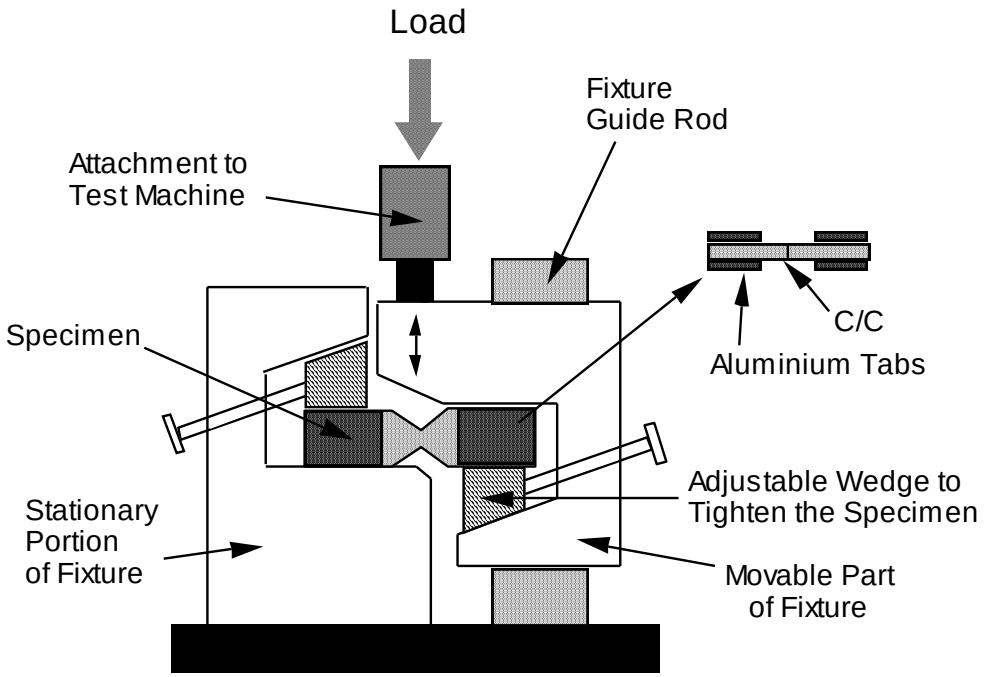

Fig. 4.3: Test fixture for the Iosipescu shear test

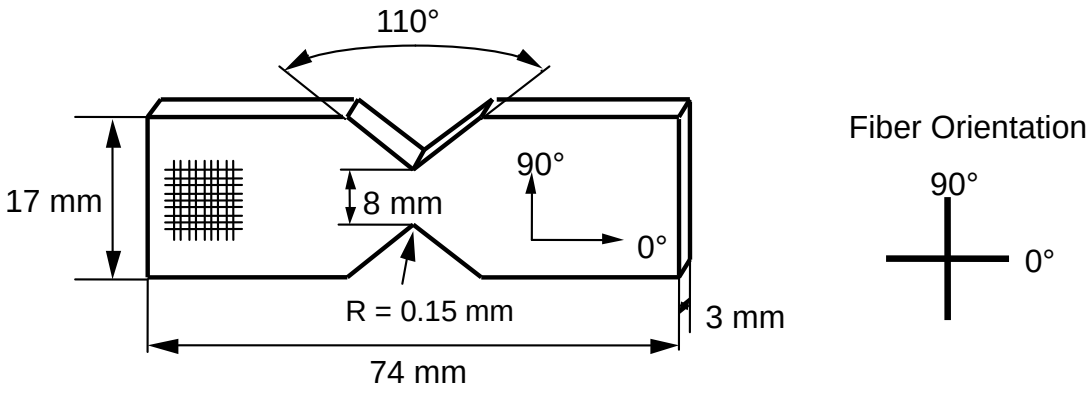

Fig. 4.4: Test specimen for the Iosipescu shear test

The stresses τ_{12} and strains γ_{12} were calculated according to the equations;

$$\tau_{12} = P / A_{min} , \qquad (4.1)$$

$$\gamma_{12} = \varepsilon_{+45} - \varepsilon_{-45} \tag{4.2}$$

where P denotes the applied load, A_{min} the minimum cross-sectional area between the two notches, and ε_{+45}, ε_{-45} the measured strains in ±45° directions.

4.1.2.2 ±45° Off-Axis and 10° Off-Axis Shear Test

In the ±45° off-axis shear test, a tensile load was applied to rectangular coupons with the fibres arranged at angles of ±45° to the loading axis as shown in Fig. 4.5 a. Strain gages were attached in the 0° and 90° directions to measure the shear stress-strain relation obtained by the following equations[86];

$$\tau_{12} = 0.5 P/A \tag{4.3}$$

$$\gamma_{12} = \varepsilon_0 - \varepsilon_{90} \tag{4.4}$$

with P, A, ε_0, and ε_{90} denoting the applied tensile load, the specimen cross-sectional area, and the strains in 0° and 90° directions.

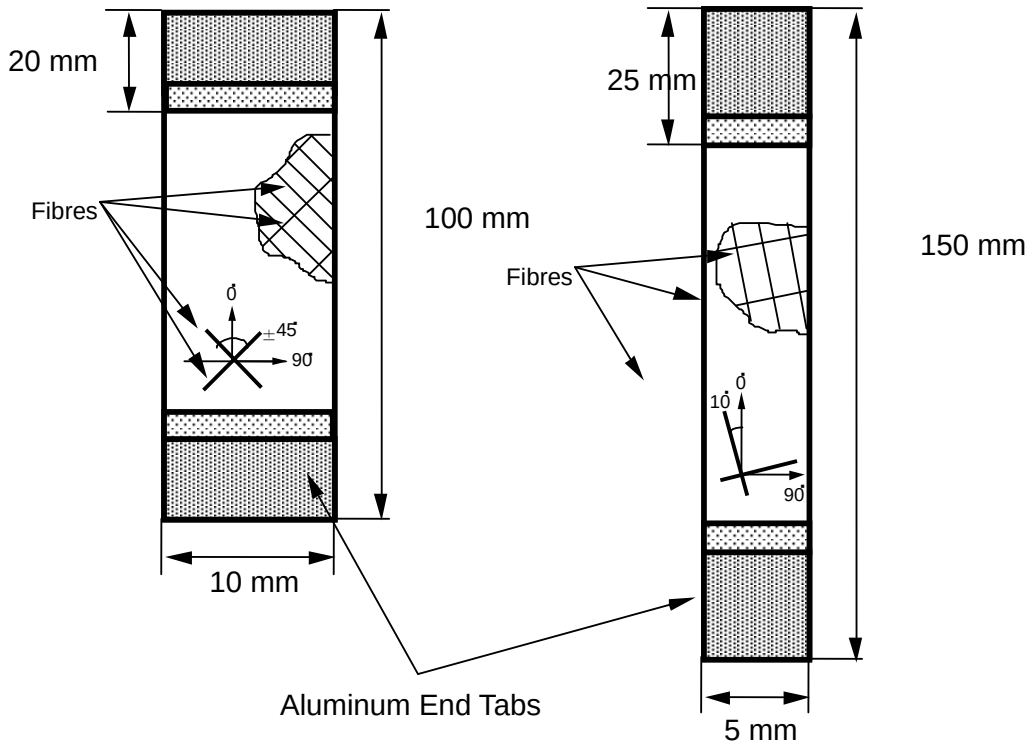

a) ±45° off-axis
tensile shear specimen

b) 10° off-axis axis
tensile shear specimen

Fig. 4.5: Tensile shear test specimen configuration.

In case of the 10° off-axis shear test specimens, the fibre orientation was set at an angle of 10° to the loading axis as shown in Fig. 4.5 b. In this test, strain gages were attached in the 0°, 90°, and ±45° directions and the shear stress-strain response was calculated from [87]

$$\tau_{12} = 0.171 P/A \tag{4.5}$$

$$\gamma_{12} = 0.342(\varepsilon_0 - \varepsilon_{90}) - 0.940\gamma_{0/90} \tag{4.6}$$

where $\gamma_{0/90}$ refers to the shear strain in the 0°/90° co-ordinate system.

Aluminium tabs were attached on both sides of all specimens to avoid stress concentration and damage near the specimen gripping region. The specimens were fractured under tension by use of a screw driven testing machine, AG-5000 made by Shimadzu Seisakusho, Japan under a crosshead speed of 0.1 mm/min.

4.1.3 Experiments to Determine the Failure Mechanisms

4.1.3.1 Detection of Fibre Failure

In order to identify fibre failure during shear tests, tensile tests were performed after shear loads had been applied to the specimens shown in Fig. 4.6. Since the fibres oriented in the loading direction carry the main tensile load, the residual tensile strength must significantly decrease if a substantial amount of fibres damaged during shear loading. The specimen configuration shown in Fig. 4.6 was chosen for the following two reasons:

1) The residual tensile strength after shear damage is expected to increase after slight shear damage [88]. Thus, to confirm tensile fracture in the pre-damaged mid cross-section, the test section must have the smallest width.

2) The introduced notches should be mild to avoid too sharp and local stress concentrations.

4.1.3.2 Detection of Inter-laminar Shear Failure

During shear testing, the specimens might be subjected to inter-laminar shear

failure. To detect this mode of fracture, short beam bending tests were conducted after different in-plane shear pre-loading levels. In these tests, specimens shown in Fig. 4.6 were first pre-loaded in shear by the Iosipescu shear test fixture. Then, smaller specimen with a length of 20 mm and width of 6.5 mm were cut out from the centre of the previously loaded Iosipescu test specimen. Finally, the inter-laminar shear strength (ILSS) of these pre-loaded coupons was measured by the three-point bending test. The maximum shear stress in the bending tests $\tau_{\#}$ appears in the mid-plane and was calculated from the applied load P by

$$\tau_{\#} = {}^{3P}\!/_{4ab} \tag{4.7}$$

where a and b are the thickness and the width of the specimen, respectively.

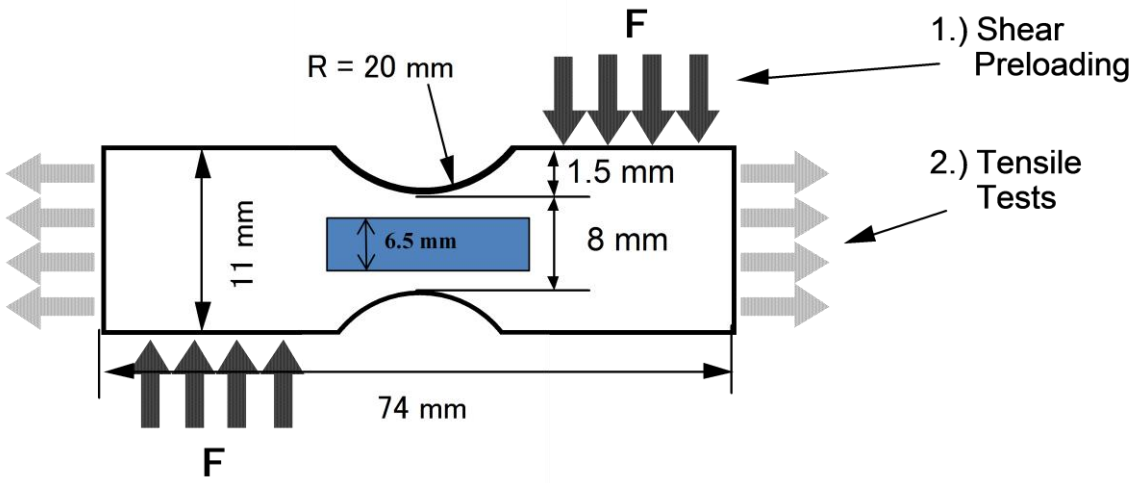

Fig. 4.6: Specimen for tensile test after shear pre-loading

4.1.3.3 Determination of the Onset of Matrix Cracking

Preliminary experiments revealed that the initiation of fibre damage and inter-laminar failure occurred at a rather late stage of the loading, but acoustic emissions had been detected much earlier. Thus, the onset of acoustic emission must be related to the beginning of matrix cracking. To verify this hypothesis, shear tests were conducted using the ±45° off-axis tensile test specimens shown in Fig. 4.5 a). During testing, the acoustic emissions were recorded using an AE sensor with a threshold level of 40 dB to suppress undesirable noise. The AE signals were then related to the measured strains.

4.2 Experimental Results

4.2.1 Comparison of the Shear Tests

The stress-strain curves obtained by the Iosipescu, 10° off-axis, and ±45° off-axis shear tests are compared in Fig. 4.7 using material with the 1:4 stacking sequence. In this figure, the shear stress is arranged on the vertical axis in MPa as a function of the engineering shear strain. The Iosipescu specimen has the highest shear strength and shows a long "tail" of nearly constant stress behind the peak. The stress-strain curves of the ±45° and +10° cases on the other hand revealed catastrophic failure. The stress-strain curves were similar in all three tests up to the fracture stress of the off-axes shear tests. However, at very small strains, Iosipescu specimens showed a stronger non-linearity. The initial strong non-linearity in the Iosipescu-test was caused by misalignment of the soft specimen introduced during tightening in the test fixture by the wedges. The misalignment could be substantially reduced by gluing thick aluminium plates on each side of a specimen. However, the stress-strain curves obtained by the off-axes shear tests were still more stable than those by the Iosipescu test. Among the 10° and ±45° off-axis shear tests, the latter method is superior due to a negligible gripping effect[8 9].

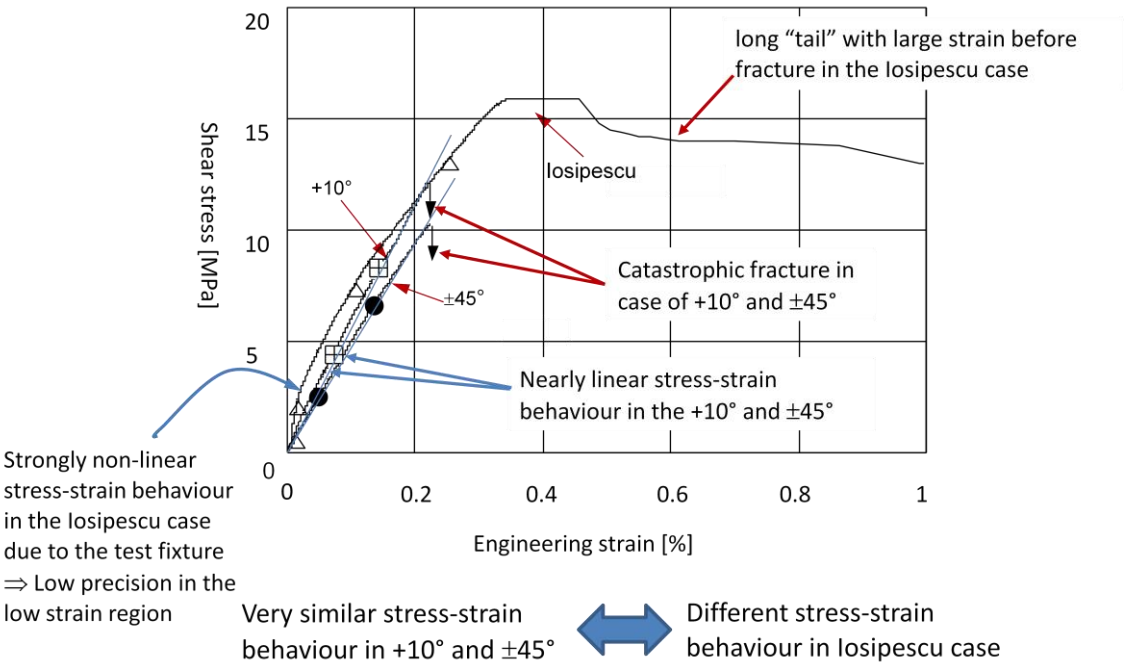

Fig. 4.7: Shear stress-strain curves obtained by Iosipescu, +10°, and ±45° tests in 1:4 stacking sequence, stresses denotes on the vertical axis in MPa.

Shear strengths obtained by the three test methods are compared in Fig. 4.8 with respect to the accompanying tensile stress component σ during shear loading. As shown in this figure, the shear strength decreases with increasing tensile component during shear loading, represented by the ratio σ/τ. The highest shear strengths were obtained by the Iosipescu test, which generates a pure shear stress distribution in the gage section. On the other hand, the 10° and ±45° off-axis shear tests induce an additional tensile component and owning to the tensile stress their test results were considerably lower. Thus, the Iosipescu configuration should be used to measure the shear strength.

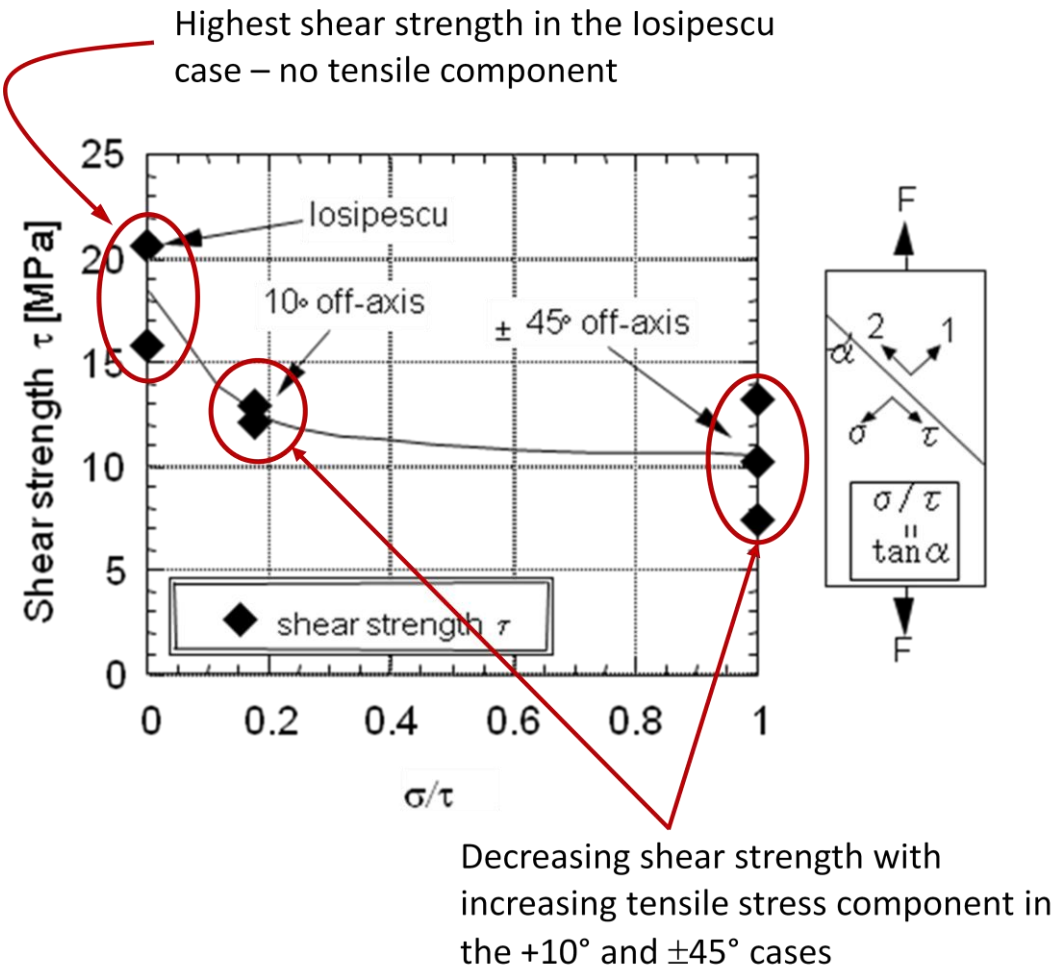

Fig. 4.8: Peak shear stress as a function of occurring tensile component, 1:4 stacking sequence.

4.2.2 Basic Shear Stress-Strain Data Acquisition for FEM

In order to obtain input data for future FEM simulations, the stress-strain behaviour of C/C composites with 1:1 stacking sequence was measured as shown in Fig. 4.9. Although stress-strain curves are more precise when obtained by the ±45° off-axis shear test, in this case the Iosipescu test was chosen. The Iosipescu test was used in order to obtain data in the high stress region above the strength of the off-axis shear tests. Analysing the stress-strain behaviour, it was found that the shear modulus G_{12} decreases nearly linear with the shear strain γ_{12} following the equation

$$G_{12} = 5{,}4 \text{ GPa} - 230 \text{ GPa } \gamma_{12} \tag{4.8}$$

in the region until $\gamma_{12} = 2\%$,
resulting in a shear stress-strain curve of the function

$$\tau_{12} = 5{,}4 \text{ GPa } \gamma_{12} - 230 \text{ GPa } \gamma_{12}^2 . \tag{4.9}$$

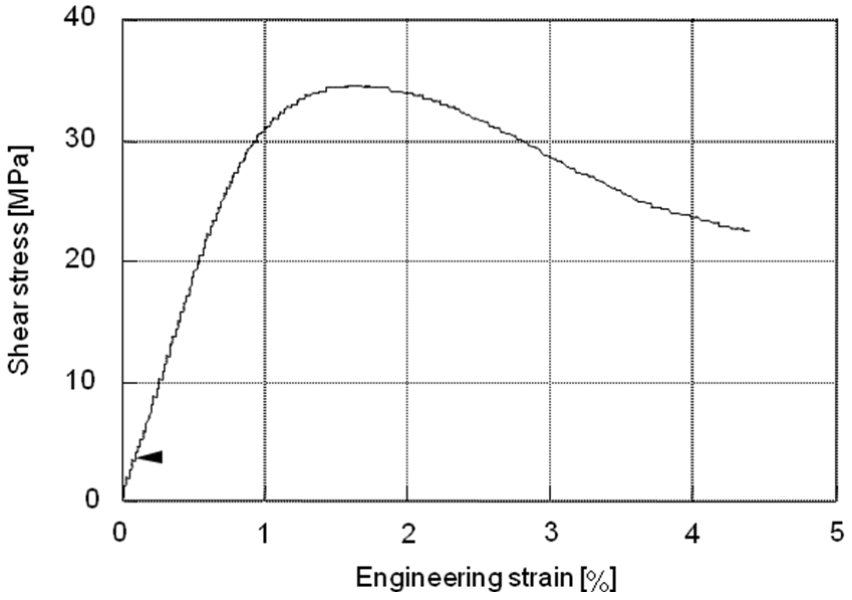

Fig. 4.9: stress-strain behaviour of C/C composites with 1:1 stacking sequence.

4.2.3 Shear Strength as a Function of the Stacking Sequence

Since the ±45° off-axis test generates a uniform stress distribution in the gage section, this configuration was used to measure the stress-strain behaviour. The test results for the specimens with a 0° ply ratio of 1:4, 1:2, and 1:1 are shown in Fig. 4.10. Although the shapes of the stress-strain curves for these specimens are nearly identical, the maximum stress of the three configurations differs significantly.

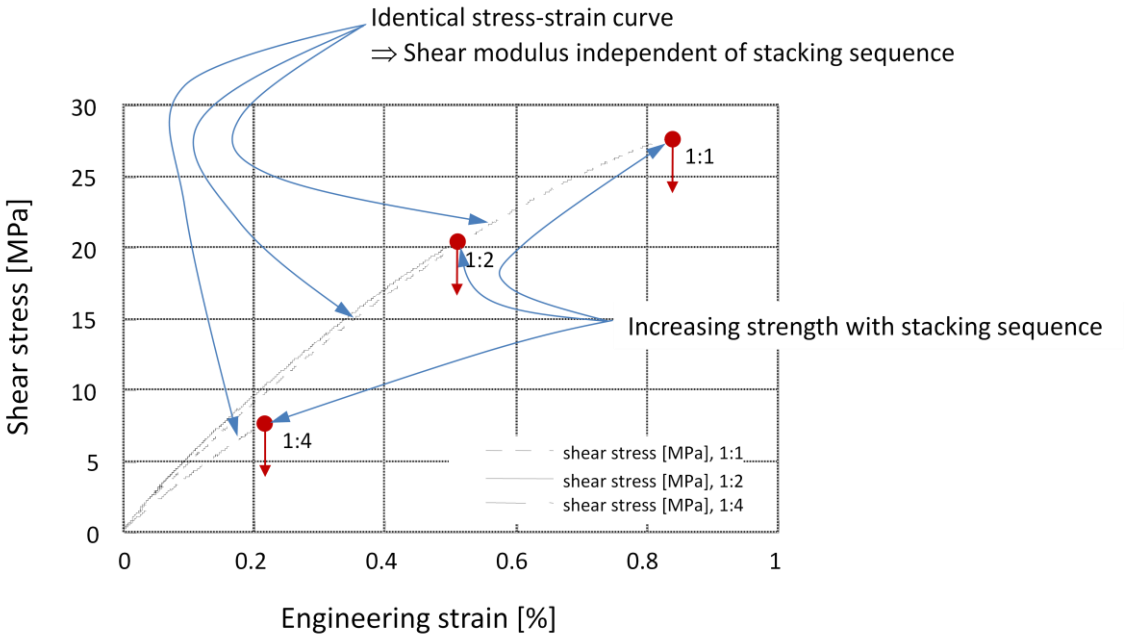

Fig. 4.10: Shear stress-strain curves in ±45° off-axis shear experiments.

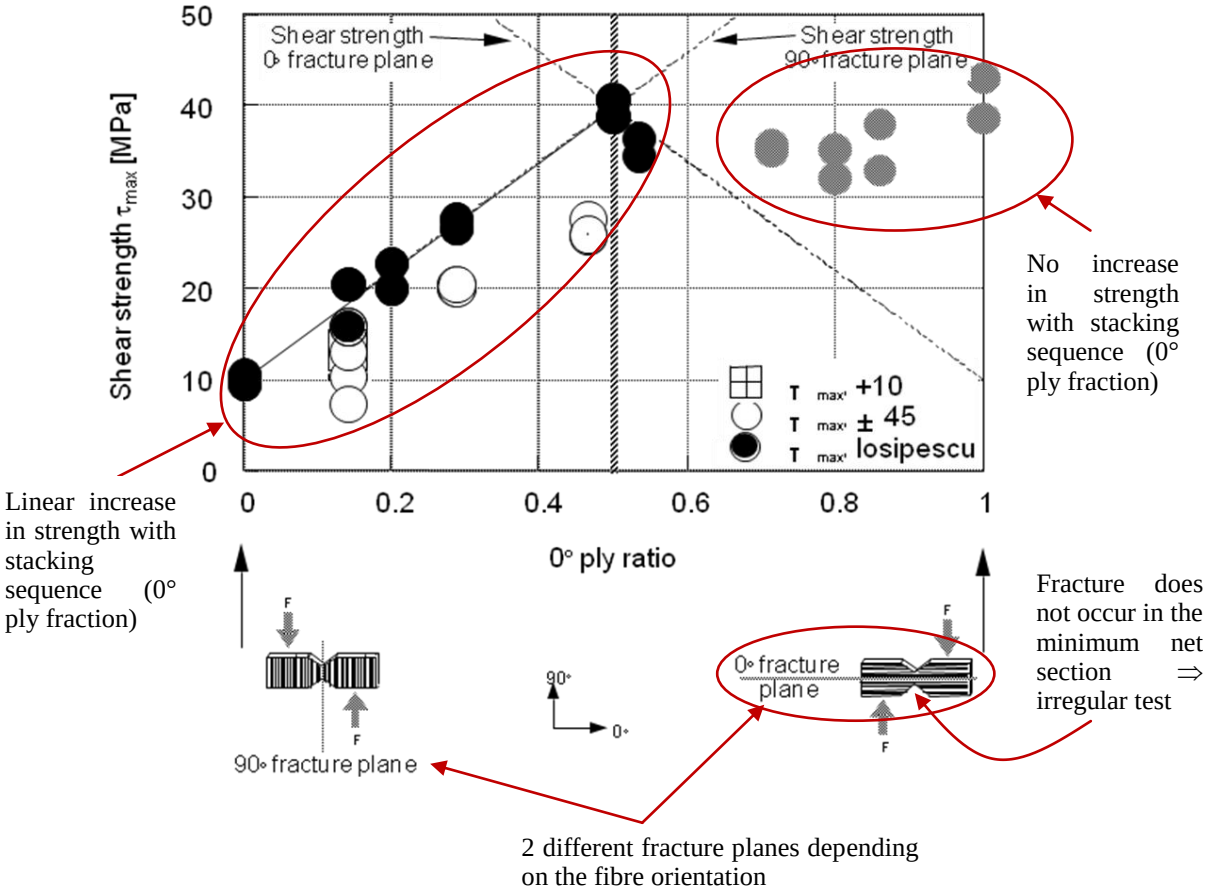

Fig. 4.11: Shear strength as a function of the stacking sequence

The shear strengths of all the specimens obtained by the three test methods are arranged in Fig. 4.11 as a function of the 0° ply ratio. As mentioned above the highest shear strengths, τ_{max}, were obtained by Iosipescu tests. This tendency was confirmed in all stacking sequences in Fig. 4.11. Thus the following discussions will focus on the Iosipescu geometry. In Fig. 4.11, two regions can be distinguished. In the left region, the shear strength, represented by the black filled circles, increases almost linearly with the 0° ply ratio. Since the shear modulus G_{12} for the same strain was independent of the 0° ply ratio, see Fig. 4.10, the maximum measured shear strain behaved essentially in the same fashion as the shear strength. Thus for the 0° ply ratio from 0 to 0.5, the measured shear strain at peak stress also increases linearly. On the other hand, on the right side of Fig. 4.11 with Iosipescu shear test results as grey dots, the measured shear strength is nearly constant albeit a further increase of the 0° ply ratio. In addition, the specimens don not fail anymore in the net section but normal to it in the 0° fracture plane. Thus, the measured values are irregular and do not represent the actual strength of the specimen configuration.

4.2.4 Shear Failure Mechanism

The upper figures in Fig. 4.12 show the residual tensile strength (RTS) after shear pre-loading for the 1:3, 1:1, and 3:1 stacking sequences. The corresponding shear pre-loading stress and strain levels are shown in the lower figures as a function of time. The filled and empty circles refer to pre-loading levels before and after the peak shear stress, respectively.

In case of loading levels prior to the peak shear stress, the RTS was found to be higher than the tensile strength of the undamaged specimen. Two conclusions can be drawn from this result:

1. The amount of fractured fibres is very small until the maximum shear stress, τ_{max}, is reached.
2. Slight shear damage has a positive effect on the strength of C/C composites.

After τ_{max}, the RTS decreased dramatically in the 1:3 and 1:1 specimens and slightly in the irregular case of the 3:1 configuration. It was concluded from these observations that significant fibre fracture occurred at the peak shear stress. Although the 1:3 and 1:1 specimens are broken once the peak shear load is attained, significant loads can still be carried due to friction, indicated by the blue area in Fig. 4.12 (a) and Fig. 4.12 (b). After the peak shear stress is reached in the 1:3 and 1:1 configuration, a sharp drop in shear

strength can be observed on the time/shear strength diagrams. The shear stress-strain curves on the other hand do not show this instable behaviour but reveal instead a long tail with nearly constant shear stress. This mismatch becomes clearer, when taking into account the time dependency in the Iosipescu shear stress-strain curve shown in Fig. 4.12 on lower right corner: While recording of the stress-strain behaviour takes approximately 260s until the peak shear stress is reached, the following 4% strain take less than one second. The shear stress-strain behaviour in shear is indeed extremely dynamic behind the peak but invisible at first glance.

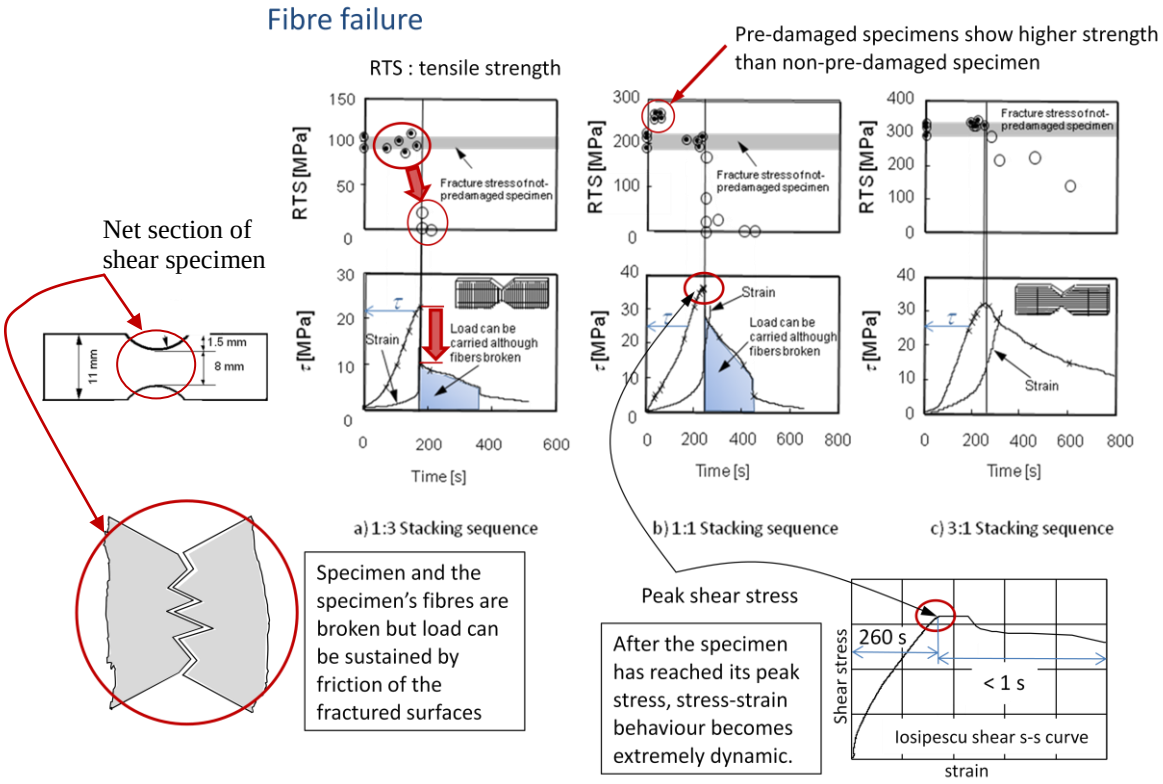

Fig. 4.12: Tensile strength after shear predamage

The residual inter-laminar shear strengths (RILSS) of shear pre-loaded 3:1 samples are shown in Fig. 4.13. The filled and dotted circles in this figure correspond to pre-loading levels before and after the peak shear stress τ_{max}, respectively. The RILSS of the 3:1 specimens reaches values between 12 and 16 MPa. In case of significant delamination induced by in-plane shear loading, RILSS should be considerably lower than that of the non-delaminated specimens. However, even after τ_{max}, such values could not be observed. Thus, substantial delamination does not occur, even at very large shear strains.

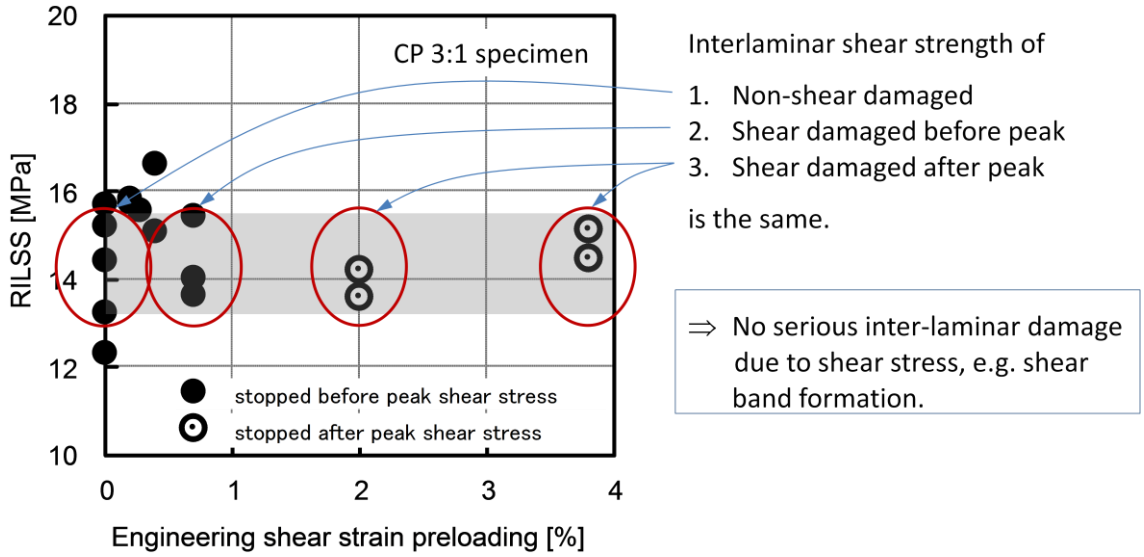

Fig. 4.13: RILSS after shear pre-loading on a 3:1 composite specimen.

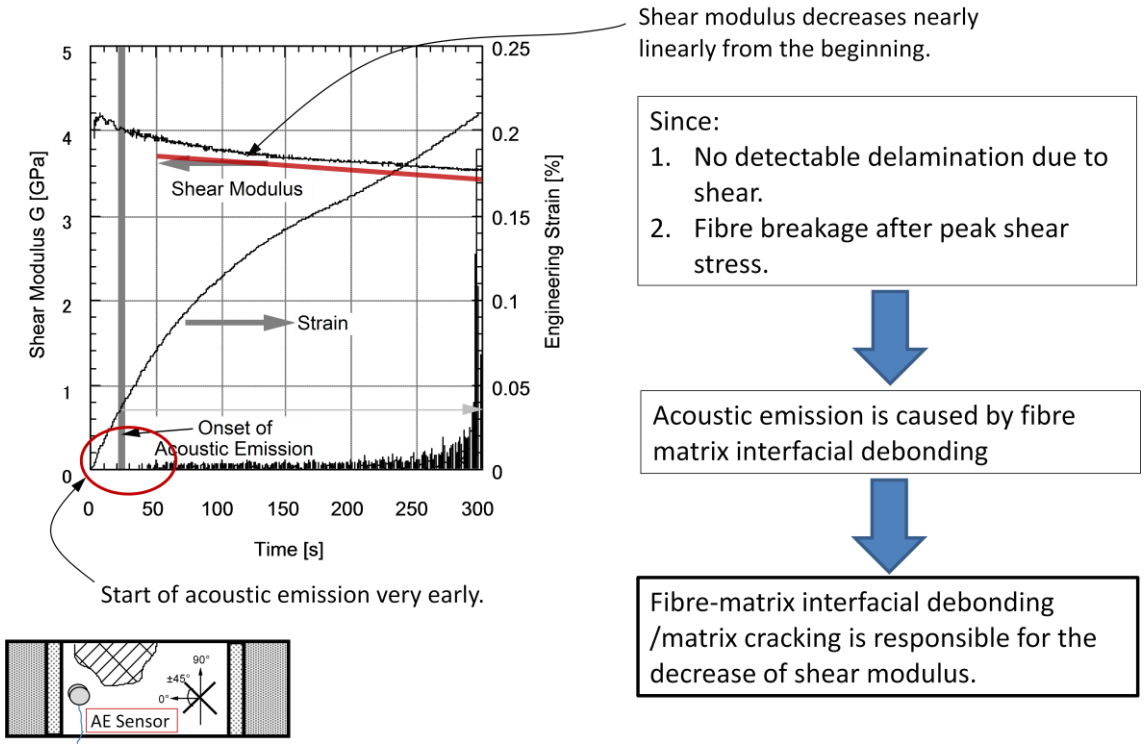

Fig. 4.14: Onset of matrix cracking

Figure 4.14 shows a typical relationship between the in-plane shear strain γ and shear modulus G_{12} superimposed on the event rate of the acoustic emission. The thick vertical bar indicates the onset of acoustic emission. The acoustic emission starts very early at a shear strain of 0.04 %, going along with a nearly linear decrease in shear

modulus G_{12}. Since fibre fracture and delamination were shown to initiate much later, the acoustic emission is related at that stage to nothing else than fibre/matrix interface debonding. Thus, the interfacial strength of the C/C determines the level of the shear modulus G_{12}. And, another important result can be drawn from this conclusion: At the beginning of this chapter we found that higher strength than that of smooth specimen could be obtained if slight shear damage was applied to the specimen. It follows from the above, that this "slight shear damage" is damage of the fibre-matrix interface. In other words, damage of the fibre-matrix interface leads to higher tensile strength of the C/C composite.

4.3 Discussion and Summary

4.3.1 Shear fracture process

From the above experimental results, the fracture process can be summarised as shown in Fig. 4.15: At a low shear strain of 0.04%, matrix cracking initiates causing the non-linearity of the shear stress-strain curve. Optical observation suggests that these matrix cracks preferably form along the fibre-matrix interface where most of the many voids are located, a feature typical for the brittle C/C Composite. As the shear load further increases these cracks eventually grow and coalesce into localised band damage as previously described by N.A. Fleck[90]. In case of the UD90 ultimate failure of the C/C occurs once large cracks have evolved.

In the cross-ply cases, the shear load is still carried after matrix/interface damage by the fibres in normal direction to the crack. Final composite fracture occurs once the local shear load exceeds the shear strength of those fibres bridging the cracked fibre-matrix interface.

In other words, shear failure of C/C composites occurs in 2 stages:

1st stage: The local shear stress leads at first to fibre-matrix debonding. The process of debonding occurs not discrete but continuous with increasing shear stress resulting in a nearly linear decrease of the shear modulus G_{12}.

2nd stage: On a microscopic level fibre-matrix debonding has proceeded so much that shear load is carried mainly by the bridging of fibres normal to the debonded fibre-matrix region.

The mechanism of stage 2 explains also why shear strength increases with 0° ply ratio as shown in Fig. 4.11. With increasing 0° ply ratio, there are simply more fibres normal to the debonded area available that can share local shear load once severe local fibre-matrix debonding has occurred.

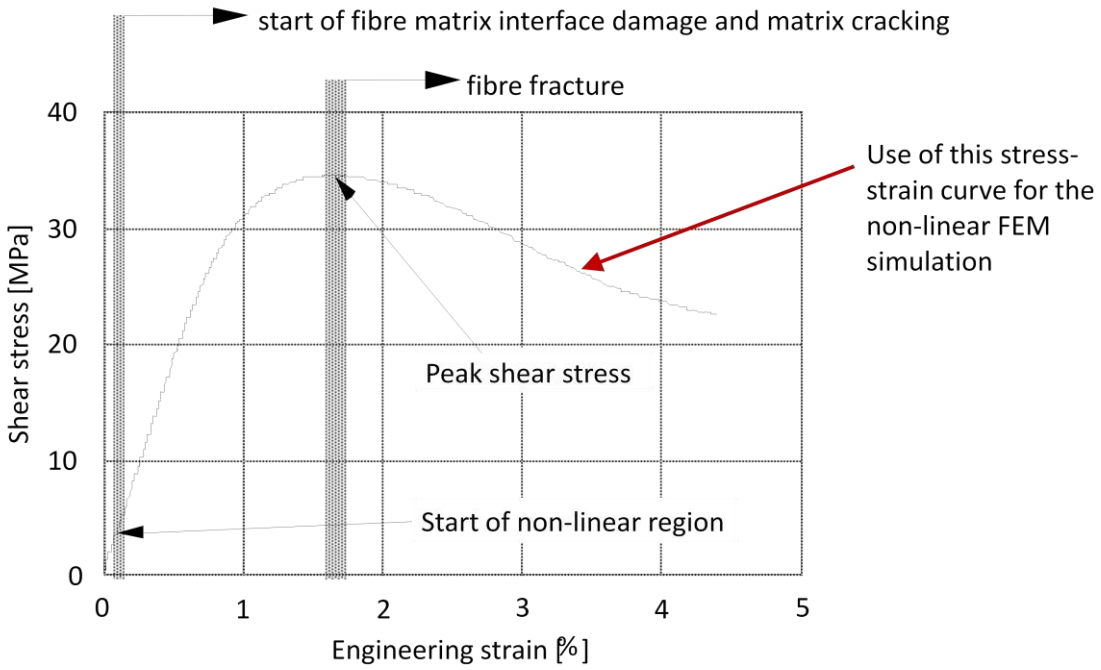

Fig. 4.15: Shear damage mechanism

Since the phenomenon is highly localised, the local strains in the debonded area cannot be measured well by the relatively large strain gages applied in our experiments. The measured strains represent the average strain of a relatively large region and have very little in common with those strains at which the C/C material actually fails locally under shear. Consequently, the measured strains at the specimen's shear fracture do not represent the fracture strain of the C/C composite. The real fracture strain of the C/C is instead determined by the fibre's shear fracture strain in its normal direction.

It was mentioned above that the shear strength does not increase for 0° ply ratios larger than 0.5 as depicted in Fig. 4.11. To understand this phenomenon, let us recall at first the shape of the Iosipescu shear test specimen shown in Fig. 4.4. In case of the Iosipescu shear test, it is generally assumed that fracture occurs in the minimum net section between the twin notches. This plane is shown in the lower section of Fig. 4.16 as vertical grey line and denoted as "assumed fracture plane". However, because of the symmetry of shear stress, $\tau_{xy} = \tau_{yx}$, there exist two fracture planes, i.e., in x-direction parallel to the 90° fibres and in the y-direction parallel to the 0° fibres.

As we pointed out above, ultimate shear fracture is determined by fibre failure. Thus, the fibre orientation determines, in which direction the specimen actually fractures. That means, if more fibres are arranged in the 90° than in the 0° direction as shown in Fig. 4.16 on the left by means of the 1:4 case, fibre fracture will occur along

the 90° direction leading to ultimate failure. On the other hand, if more fibres are arranged in the 0° than in the 90° direction, e.g. 0° ply ratios between 0.5 and 1 , fibre failure initiates along the 0° direction, as indicated in Fig. 4.16 on the right by the 4:1 case. In this case, the 0° cracks arrest after an initial extension to the increasing cross-sectional area. Fibre failure in the 90° direction, matrix cracking, and fibre/matrix debonding result in this case in a substantial "softening" of the net section. This "softening" causes a time-strain curve as shown in Fig. 4.12 on the right: The stacking sequences from 2:1 to UD0 do not reveal a sudden drop of shear stress. In addition, the fracture surface suggests that final failure occurred not under shear but under bending caused by the large deformation. Thus, in case of 0° ply ratios between 0.5 and 1, the measured shear strengths of Fig. 4.11, do not represent the actual shear strength of the material.

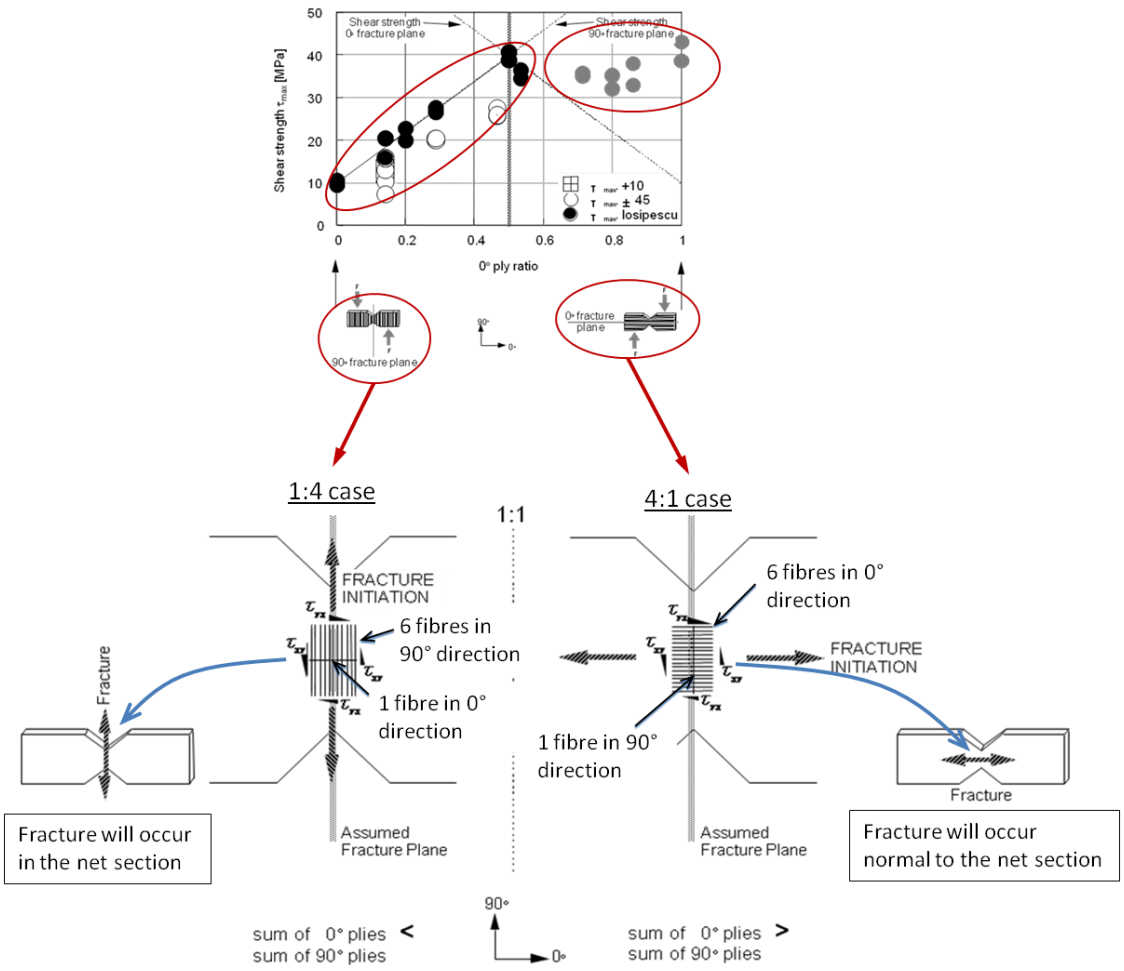

Fig. 4.16: Assumed fracture plane and actual fracture initiation of Iosipescu shear specimens.

Since the material can fracture in two planes under shear, the shear strength in

both directions must be considered. In the present specimens, an increasing fibre fraction in one plane essentially leads to a decreasing fibre fraction normal to that plane. Consequently, increasing shear strength in one direction corresponds inevitably with a decreasing strength in its normal direction. The material's overall shear strength should be, for safety considerations, that of the weaker direction. Accordingly, the optimum shear strength will be obtained if the shear strengths are identical in the 0° and 90° directions. This condition is realised for the cross ply $(0/90)_n$ case, meaning that the shear strength of the present materials is symmetric with respect to the 1:1 ply ratio, as shown in Fig. 4.11 by the two dotted lines.

4.3.2 Conclusion

The fracture mechanism of laminated C/C with changing stacking sequences was examined by three different shear tests.

Concerning the shear test method it was found that:

1. The Iosipescu method gave rise to the highest shear strengths. Thus, this method can be recommended to measure the shear strength of C/Cs.
2. The +10° and ±45° off-axis tests showed the most consistent shear stress-strain curves. In addition, the gripping effect can be neglected in the ±45° off-axis test. Consequently, these tests are recommended for the precise shear stress-strain and shear modulus measurements at low strain levels.

The fracture mechanism under shear can be summarised as follows:

3. Non-linearity in the stress-strain behaviour initiates at extremely low strains in the magnitude of 0.04 %.
4. Delamination even after the peak shear stress is insignificant.
5. Since fibre failure determines the shear strength, the shear strength increases linearly with an increase of fibres oriented transverse to the fracture plane.
6. In a shear test like for example the Iosipescu test, two fracture planes exist: One parallel to the longitudinal axis (0° direction), and the other one in the minimum net section between the two V-notches (90° direction).
7. As the 0° ply ratio increases, the shear strength increases in the 90° plane, and decreases in the 0° plane.
8. At a $(0/90)_n$ stacking sequence, the shear strength in both planes is the same. Thus, the overall shear strength is the highest in this configuration.

9. Shear failure of C/C composites occurs in 2 stages: In stage 1, the local shear stress leads at first to fibre-matrix debonding. The process of debonding does not occur discrete but continuous with increasing shear stress resulting in a nearly linear decrease of the shear modulus G_{12}. In stage 2, the fibre-matrix debonding has proceeded on a microscopic level so much that shear load is carried mainly by the bridging of those fibres normal to the debonded fibre-matrix region. Shear fracture occurs, once the local shear stress exceeds the shear strength in normal direction of those fibres bridging the fibre-matrix interface.
10. The interfacial strength of the C/C determines the level of the shear modulus G_{12}.
11. Slight shear damage with rather low strains around 0.5 mm leads to much higher net fracture stresses. Since fibre fracture and delamination under shear occur at much higher strains the mechanism leading to these high strengths must be fibre-matrix debonding. Commonly, the C/C composite fractures roughly at the same fracture strain as the pure matrix although the fracture strain of the fibres is much higher. Thus, the constraint of the matrix leads to strain degradation. The present result suggests that this matrix constraint was relaxed at low shear stresses due to damage of the fibre-matrix interface. Leaving the fibres intact this mechanism leads to a higher tensile fracture stain and residual tensile strength.

---

[64] L. M. Manocha, O. P. Bahl, Influence of carbon fiber type and weave pattern on the development of 2-D carbon-carbon composites, Carbon, 26(1), 13-21 (1988)
[65] S., M. Oh, J., Y. Lee, Fracture behaviour of two-dimensional carbon/carbon composites Carbon, 27(3), 423-430 (1989)
[66] K. Anand, V. Gupta, D. Dartford, Failure mechanisms oflaminated carbon-carbon composites-II. Under shear loads, Acta metall. mater., 42(1994), No.3, 797-809
[67] P. Bronstedt, F.E. Heredia, A. G. Evans, In-plane shear properties of 2-D ceramic matrix composites, J. Am. Ceram. Soc., 77(10), pp. 2569 (1994)
[68] A. Okura, T. Chou, Advanced Composites in Emerging Technologies, 348-353, (1992)
[69] Iosipescu, N., Rev. de Mec. Appl., Photoelastic investigations on an accurate procedure for the pure shear testing of materials, 1, 145-164 (1963)
[70] D., E. Walrath, D., F. Adams, The Iosipescu shear test as applied to composite material, Exp. Mech., 23, 105-110 (1983)
[71] D. F. Adams, D. E. Walrath, Further development of the Iosipescu shear test method, Exp. Mech., 27, 113-119 (1987)
[72] D. F. Adams, D. E. Walrath, Current status of the Iosipescu shear test method, J. Comp. Mater., 21, 494-507 (1987)
[73] J. Morton, H. Ho, M. Y. Tsai, G. L. Farley, An evaluation of the Iosipescu specimen for composite materials shear property measurement, J.Comp.Mater., 26(5), 708-750 (1992)
[74] H. Ho, M. Y. Tsai, J. Morton, G. L. Farley, An experimental investigation of Iosipescu specimen for composite materials, Exp. Mech., 33, 328-336 (1993)
[75] M. J. Pindera, P. Ifju, D. Post, Iosipescu shear characterization of polymeric and metal matrix composites, Exp. Mech., 30, 101-108 (1990)

[76] J., L. Sullivan, B., G. Kao, H. Van Oene, Shear properties and a stress analysis obtained from vinyl-ester Iosipescu specimens, Exp. Mech., 24, 223-232 (1984)
[77] S. Lee, M. Munro, R., F. Scott, Evaluation of three in-plane shear test methods for advanced composite materials, Composites, 21, 495-502 (1990)
[78] H. Ho, M. Y. Tsai, J. Morton, G. L. Farley, A comparison of three popular test methods for determining the shear modulus of composite materials, Comp. Eng., 3, 69-81 (1993)
[79] M. J. Pindera, G. Choksi, J. S. Hidde, C. T. Herakovich, A methodology for accurate shear characterization of unidirectional composites, J. Comp. Mater., 21, pp. 1164-1184 (1987)
[80] S. Lee, M. Munro, R., F. Scott, Evaluation of three in-plane shear test methods for advanced composite materials, Composites, 21, 495-502 (1990)
[81] H. Ho, M. Y. Tsai, J. Morton, G. L. Farley, A comparison of three popular test methods for determining the shear modulus of composite materials, Comp. Eng., 3, 69-81 (1993)
[82] M. J. Pindera, G. Choksi, J. S. Hidde, C. T. Herakovich, A methodology for accurate shear characterization of unidirectional composites, J. Comp. Mater., 21, pp. 1164-1184 (1987)
[83] M. J. Pindera, C. T. Herakovich, Shear characterization of unidirectional composites with off-axis tension tests, Exp. Mech., 24, 103-112 (1986)
[84] T. Dickson, M. Munro, S. Lee, Selection of an in-plane shear test method based on the shear sensitivity of laminate tensile modulus, Composites, 26(1), 17-32 (1995)
[85] S. Lee, M. Munro, Evaluation of in-plane shear test methods for advanced composite materials by the decision analysis technique, Composites, 17, pp.13-22 (1986)
[86] H. Ho, M. Y. Tsai, J. Morton, G. L. Farley, A comparison of three popular test methods for determining the shear modulus of composite materials, Comp. Eng., 3, 69-81 (1993)
[87] H. Ho, M. Y. Tsai, J. Morton, G. L. Farley, A comparison of three popular test methods for determining the shear modulus of composite materials, Comp. Eng., 3, 69-81 (1993)
[88] L.Denk, H. Hatta, S. Somiya, M. Hiroaki, Fracture behaviour of multi-holed C/C composites, Adv. Composite Mater., 12, 107-122 (2003)
[89] M. J. Pindera, C. T. Herakovich, Shear characterization of unidirectional composites with off-axis tension tests, Exp. Mech., 24, 103-112 (1986)
[90] N. A. Fleck, Brittle fracture due to an array of microcracks, Proc. R. Soc. Lond., A 432, pp.55 (1993)

5. Tensile strength enhancement (TSE)

5.1 Introduction

As found in the chapter 3.4.3, damage of the fibre-matrix interface increases the tensile strength of C/C composites. In the previous chapter the test results of DEN specimen with shear damaged prior to tensile testing were discussed. We found that those specimens revealed higher net fracture stresses $\sigma_{f,net}$ than the ultimate tensile strength of their smooth (un-notched) counter parts.

The ultimate tensile strain of the C/C composites (ε_{ult}), about 0.2~0.4%, is generally much lower than that of their reinforcing carbon fibres, 0.65~1.5%. This low ε_{ult} was believed to be caused by the constraint of the matrix, i.e., the ε_{ult} of C/Cs being nearly equal to that of the matrices[91]. Hence, if the matrix constraint is partly released by interfacial damage, the ε_{ult} of C/Cs can be recovered towards that of the reinforcing fibre. When the specimen width of a DEN specimen becomes smaller, the damage zones emanating from the two notches unite and cover the whole ligament. This allows us to understand the above-mentioned high tensile strength behaviour.

As discussed in the previous chapters, the C/C is known to have low interfacial bonding between the fibre and matrix[92], and interfacial damage appears in the early stage of loading. Hence, the above-described mechanism is especially plausible for C/Cs and governing such a behavior is extremely important, because it might provide a way to control tensile fracture of C/Cs.

In the following, enhancements of tensile strength are examined for C/Cs given various modes of micro-pre-damage. The pre-damage includes static shear, tensile fatigue, stress-concentrations, and slight oxidation. Following this introduction, the experimental procedures are briefly explained in section 2. The tensile and bending strengths of damaged and undamaged C/C specimens are shown in section 3. Then, in section 4 the controlling mechanisms of the strength-increasing phenomenon are discussed paying attention to fibre/matrix interfacial damage in C/Cs, and its influence on notch insensitivity. Finally, concluding remarks are provided in section 5.

5.2 Material

The C/Cs tested in the present study were fabricated like all other materials in this thesis by the preformed yarn method[93] and supplied by Across Co., Japan. The properties of C/Cs are rather unstable, so that tensile strength usually varies with fabrication lots. Two fabrication lots of C/Cs were used in the present study. The

material properties of these C/Cs are shown in Table 5.1, where materials are identified by Lot A and Lot B.

The Lot B C/C was used only for fatigue and related static tests, and the rest of experiments were conducted using the Lot A C/C.

Table 5.1 Properties of C/C composites

Notation	Lamination	density (g/cm^3)	Strength (MPa)	Young's Modulus (GPa)
Lot A	Cross ply	1.75	185	85
Lot B	Cross ply	1.80	229	95

5.3 Mechanical tests

The strength enhancement phenomena are assumed to be induced by micro-damage in the matrix, which does not completely appear in static tensile tests using smooth specimens. To study the effect of damage, various types of pre-damage in specimens were introduced before static tensile or bending fracture tests. The pre-damage involved shear, stress concentrations, fatigue, and oxidation. All the static tensile, shear, and bending tests were carried out using a screw-driven mechanical testing machine (by Shimadzu Co. model AG-5000A) with a fixed cross-head speed of 0.1 mm/min in air at 298 K. The strain during tensile testing was determined by two strain gages (an effective gage area of 2 x 5 mm^2) adhered parallel to the loading direction on both surfaces of a plate specimen. Two acoustic emission sensors (AE-900M-WE, NF Electric Instruments Co., Japan) were attached to the shoulders of dumbbell-shaped specimens in order to detect the micro-fractures occurring before the ultimate failure. The specimens for all the present tests were processed from 300 x 300 x 3 mm plates using a conventional milling machine. The fracture surfaces and polished cross-sections of the fractured specimens of both the original and fatigued C/Cs were observed via an optical microscope in order to monitor the micro-fracture during various mechanical tests. The following test procedures were carried out:

5.3.1 Static tensile, shear, and flexural tests

As base data, the static tensile, shear, and bending fracture stresses and their stress-strain relations in the C/Cs were determined. The geometry of the tensile test specimens is shown in Figure 5.1(a), in which the width *W* was varied from 4 mm to 36

mm. In order to avoid secondary damage, tapered aluminium tabs (thickness = 1.0 mm) were adhered at the grip areas using an epoxy adhesive. One of the fibre axes in the specimens was set parallel to the loading direction. The shear behaviour was obtained using an Iosipescu type fixture[94], shown in Fig. 4.3, and a test piece as shown in Figure 5.1(b) and Table 5.1. The geometry of this specimen was different from that used in ordinary Iosipescu tests[95] for the convenience of eventually thereafter following residual tensile strength measurements. The shear strain was obtained from the normal strains measured by strain gages bonded and at the centre of the specimen in the directions of ±45°[96]. In order to confirm a nearly uniform shear stress distribution in the region between the double notches, FEM calculations were performed for the Iosipescu shear specimen.

5.3.2 Tensile tests of double-edge notched (DEN) specimens

Double-edge-notched (DEN) specimens of various width, *W*, notch length, *a*, and notch root radii, ρ, were prepared keeping 2*a*/*W*=0.5, where *W* was set to 4, 8, or 36mm and ρ was varied from 0.15mm to 20mm as shown in Figure 5.1 (b) and Table 5.2. These specimen shapes were chosen for examining both, notch-sensitive and notch-insensitive behaviours. According to previous results[97,98,99], notch-sensitive fracture behaviour can be observed for the case of small ρ and notch-insensitive for large ρ.

Table 5.2 Dimensions of specimens for shear and double-edge-notched test

	Shear test (mm)		Notch sensitivity test (mm)		
ρ	0,15	5	0,15		20
a	4,5		1	5	9
W	18		4	20	36
L	120		150		

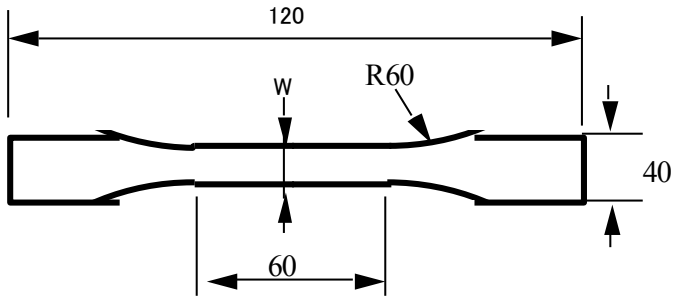

(a) Tensile test (t = 3 mm)

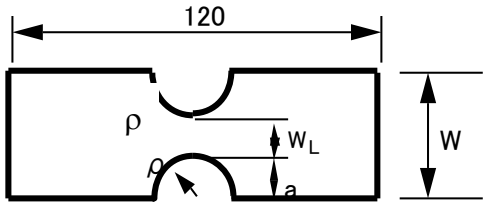

(b) DEN tensile and shear tests (t = 3 mm)

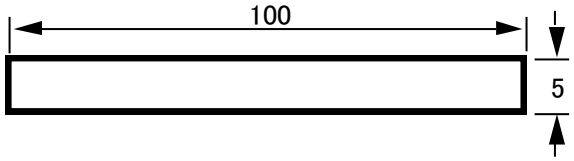

(c) Bending tests after oxidation (t = 1.5 mm)

Fig. 5.1: Geometry of specimen used during mechanical testing

5.3.3 Tensile tests after fatigue damage

Load-controlled tension-tension fatigue tests were conducted using a hydraulic-driven testing machine (EFH-FB01, Shimadzu Co., Japan) under a sinusoidal loading frequency of 10 Hz. The stress ratio (*R*), defined as the ratio of the minimum and maximum stresses in load cycles, was set to 0.1. The specimen geometry for fatigue tests is shown in Figure 5.1(a). Residual static tensile strengths were determined for the fatigue-loaded but not for the fractured C/Cs.

5.3.4 Tensile tests after shear damage

One of characteristics of the mechanical response of C/Cs is low shear strength and a strongly non-linear shear stress-strain relation[100,101,102,103,104]. Thus,

subcritical micro-damage should accompany shear loading of C/Cs. In order to study the effect of this damage on tensile strength, various levels of shear micro-damage were intentionally introduced in the DEN specimens using the Iosipescu test fixture. The geometry and dimensions of the DEN specimens are shown in Fig. 5.2, respectively. The residual tensile strengths of the damaged specimens were then measured. Note that an improvement of tensile strength was expected in the damaged area, so that the notches were introduced in order to establish the tensile fracture's location within the pre-damaged area. The notch root radius of the specimens was set to 0.15 or 5 mm. In order to identify the damage level induced by the shear pre-load, pure shear fracture tests were performed using the DEN specimens under monitoring AE signals.

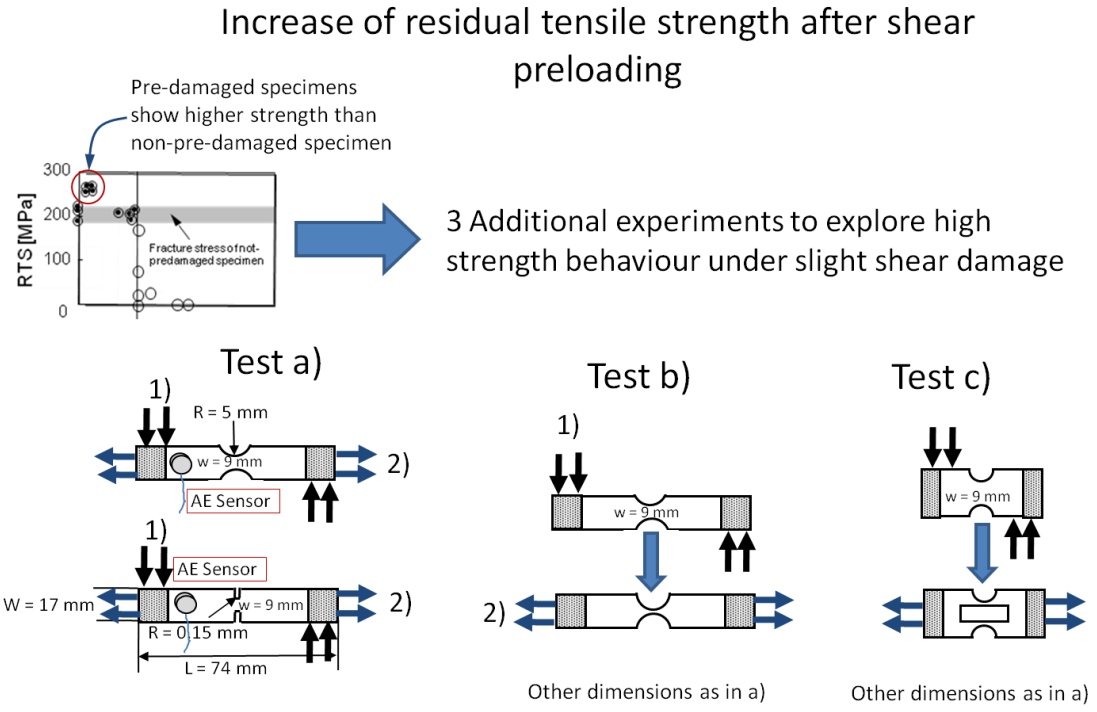

1) Shear preloading with different strain levels
2) Tensile test

Fig. 5.2: Increase of tensile strength after shear preloading – test configuration.

5.3.5 Bending strength after oxidation damage

Low oxidation resistance is the most serious shortcoming of C/Cs[105,106,107]. Oxidation resistance depends upon the location in C/Cs; the highest oxidation rate is along the fibre/matrix interfaces[108,109]. This suggests that a slightly oxidized C/C has weak interfaces especially near the surface. Hence, the effect of interface on the tensile

strength can be estimated by comparing the flexural strengths of as-received and slightly oxidized C/Cs[110]. Rectangular-shaped specimens as shown in Fig. 5.1 c) having length, width, and thickness of 100 mm, 5 mm, and 1.5 mm, respectively, were prepared for this test. The C/C specimens were oxidized at 733K, 850K, and 950 K up to a maximum mass loss ratio of 4%. In general, two oxidation regimes can be identified[111,112,113,114]. At low temperatures, the material oxidized at a uniform rate irrespective of the location in the material (chemical-reaction-rate-controlling regime). However, at high temperatures oxidation occurs only near the surfaces due to the complete consumption of diffused oxygen by the high oxidation reaction rate (oxygen-diffusion-rate controlling regime). In the present study, the oxidation of the C/C was performed within the temperature region of the former regime[115,116,117]. The strengths of oxidized C/Cs were determined by means of four-point-bending tests, where inner and outer spans were set to 27 and 81 mm, respectively.

5.4 Experimental results

5.4.1 Static tensile and shear behaviour of C/C composites

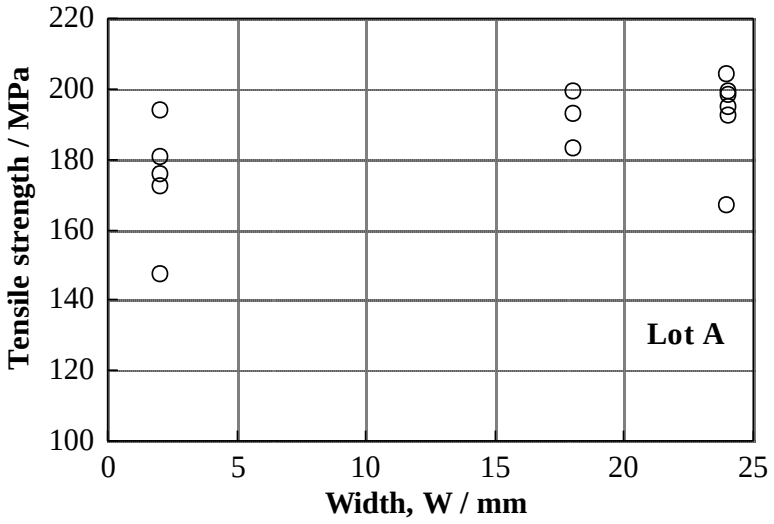

Fig. 5.3: Tensile strength of the Lot A C/C as a function of the gage section width of dog-bone type specimens.

The results of static tensile tests using the Lot A C/C are shown in Fig. 5.3 as a function of the width (*W*) in the gage section of the dog-bone shaped specimen of Fig. 7.1 (a). In spite of wide scattering, the ultimate fracture stress, σ_0, is almost

independent of *W*. This tendency was in accordance with that reported in our earlier works[118]. Thus, a representative tensile fracture stress σ_0 of the Lot A C/C was determined by the average value of all data, 185 MPa, and through a similar procedure, σ_0 of Lot B was determined to be 229 MPa. All the tensile stress-strain relations of the C/Cs were almost linear up to the ultimate fracture[119,120].

Figure 5.4 shows a typical shear stress-strain relation of the Lot A C/C. This curve was obtained by the Iosipescu tests using the DEN specimens with ρ = 5 mm. The horizontal axis of this figure is the principal normal strain, and the difference of the two normal strains is the shear strain, γ_{xy}. Only an initial part of the stress-strain relations is shown along with AE event rates to clearly represent the relation between damage development and nonlinearity in the stress strain curve. The non-linear stress-strain relation and AE events began at a stress of about 15 MPa. Intensive non-linear behaviour continued after this and the ultimate stress and strain reached 45 MPa and 2%, respectively. Low shear strength and strong non-linearity are salient features of C/Cs[121,122].

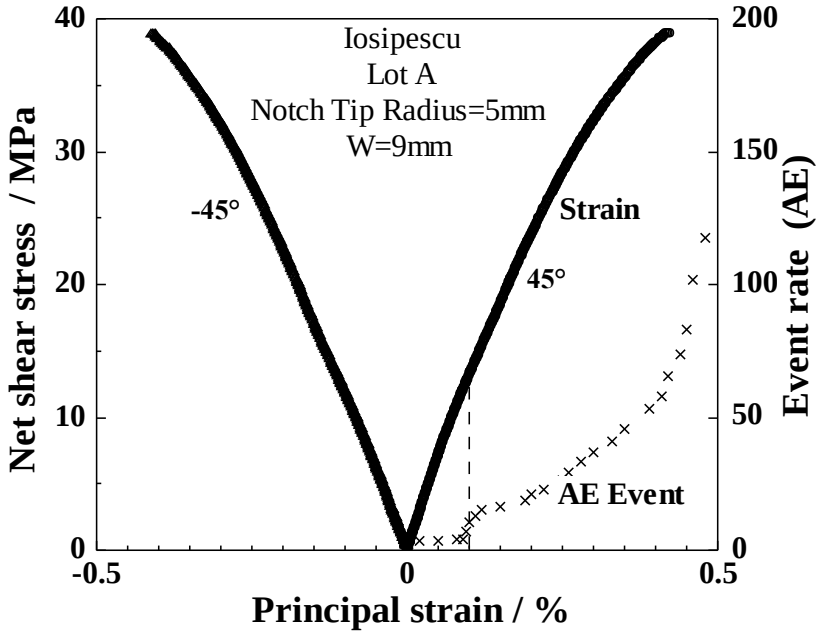

Fig. 5.4: Shear stress-strain relation of the Lot A C/C obtained using an Iosipescu type shear fixture.

5.4.2 Tensile strength of DEN specimens

Figure 5.5 shows the net tensile fracture stress, $\sigma_{f,net}$, of the DEN specimen made of the Lot A C/C as a function of the notch tip radius, ρ. When the specimen width is small, W = 4 mm, $\sigma_{f,net}$ is higher than the average fracture stress of smooth specimens (σ_0) shown by the shaded band. Since the tensile strength of smooth specimens did not exhibit width dependence as shown in Figure 5.3, the high strength behaviour is not due to such a dimensional effect as explained by the Weilbull distribution. No damage was observed near the notch tips before the ultimate fracture by using a travelling microscope of 30 times magnification. The fracture behaviour of notched C/Cs shown in Figure 5.5 is peculiar, i.e., insensitive to ρ but sensitive to W. Regarding W dependence, the net fracture stress was shown to almost obey the fracture toughness criterion[123124125126]. A similar but more enhanced behaviour was obtained for three-dimensionally reinforced C/C[127].

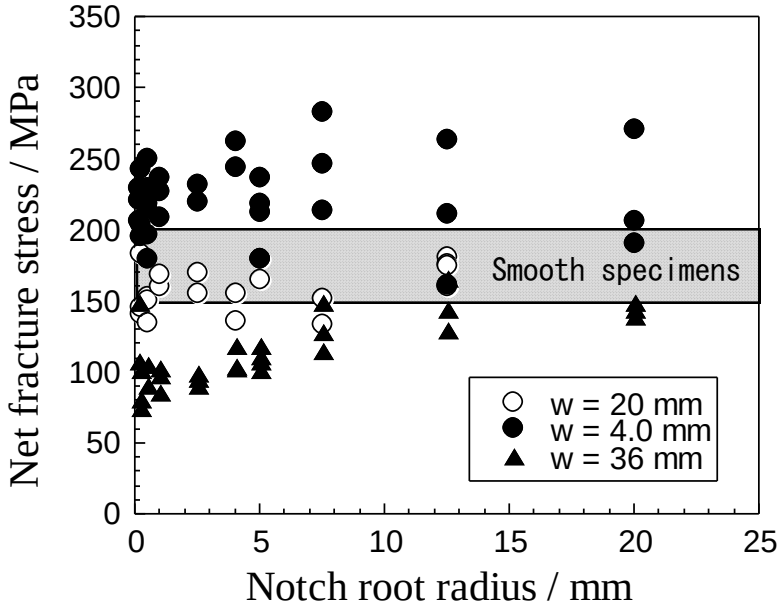

Fig. 5.5: Net fracture stress of double-edge-notched specimens as a function of the notch tip radius.

5.4.3 Residual strength of fatigue-loaded C/Cs

The maximum stress vs. number of cycles to failure, S-N, relation of the Lot B C/C obtained by the fatigue tests is shown in Figure 5.6, where residual strengths were plotted for specimens fatigue-loaded but not fractured with black filled circles. The shaded area indicates the scattering of the static tensile strength. As can be seen in this

figure, the C/C never failed during fatigue loading at a number of cycles over 10^4. This result implies that the tensile strength of the C/C was enhanced during fatigue loading. Slight strength degradation of the C/C during fatigue loading until 10^4 cycles might be caused by the fibre damages due to wear occurring at the interfaces [128129130].

The maximum applied fatigue stress of surviving fatigue-loaded specimens was 210 MPa. The residual strength of the then following static tensile test reached 117% of the original strength at the maximum. The residual strength increased linearly with maximum fatigue stress. The fracture surfaces of the strength-enhanced C/C after fatigue exhibited a large number of splits along the fibre axis with some of them being particularly long. On the other hand, the as-received C/C showed brittle fracture without splitting. The optical microscope observation revealed that a large amount of fibre/matrix interfacial debonding was newly produced during fatigue-loading [131].

Thus, the fatigue behaviour of the C/C can be understood as the competition of two types of damages: Interfacial damage enhancing but fibre damage degrading tensile fracture stress.

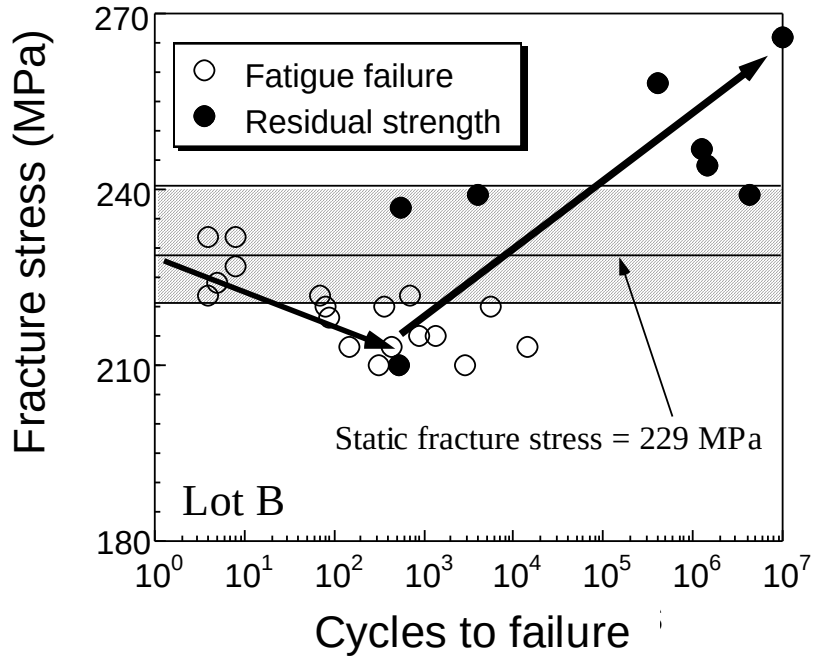

Fig. 5.6: Fatigue fracture stresses and residual fracture stresses after fatigue loading of lot B C/C as functions applied load cycles. The shaded area indicates the scattering of tensile strength of the original specimen.

5.4.4 Tensile strength of shear damaged specimens

Figure 5.7 shows the net tensile fracture stresses of the shear-damaged DEN specimens (Lot A C/C), $\sigma_{f,net}$, as a function of pre-applied shear strain, γ_{pre}. The $\sigma_{f,net}$ for W=18mm are estimated to be 166 MPa and 147 MPa for the specimens with the notch root radii, ρ, of 5 and 0.15 mm, respectively. As shown in Figure 5.7, $\sigma_{f,net}$ increases rapidly with increasing γ_{pre} up to about 300 με and 800 με for the cases of ρ = 0.15mm and 5 mm, respectively. At these maximums, $\sigma_{f,net}$ is about 220 MPa and thus it exceeds the strength of the smooth specimen, 185 MPa. When γ_{pre} surpassed the maximums, $\sigma_{f,net}$ gradually decreased with the increase in γ_{pre}. The solid line in Figure 5.7 represents the accumulation of corresponding AE events during shear loading for the sample with ρ = 5 mm. As this curve shows, the AE events start to increase drastically behind the shear pre-loading level at which the maximum $\sigma_{f,net}$ was reached. This result indicates that only slight shear damage, e.g. fibre-matrix debonding, enhances the residual tensile fracture stress of C/Cs. This corresponds well with findings made in the shear chapter of this thesis.

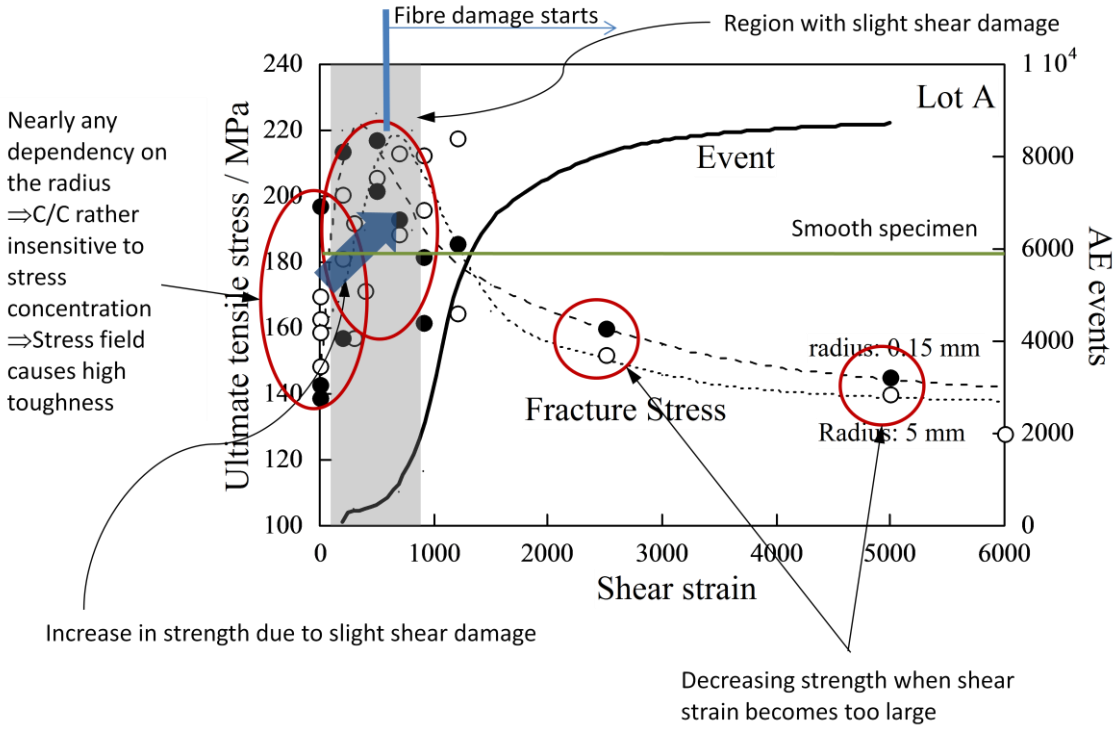

Fig. 5.7: Net tensile fracture stress of the pre-shear-damaged DEN specimens as a function of pre-loaded shear strain.

To understand the strength enhancement behaviour more clearly, two sets of experiments were performed. First, the notch length, a, of specimens which had been

shear-damaged by 2500 με or 5000 με was enlarged and then the residual tensile strength was measured. As shown in Figure 5.8, $\sigma_{net\text{-}ult}$ increases rapidly to a value of about 225 MPa by only a small amount of cut-out length of about 0.25 mm. This result implies that during shear pre-loading the reinforcing fibres near the notch tips were damaged.

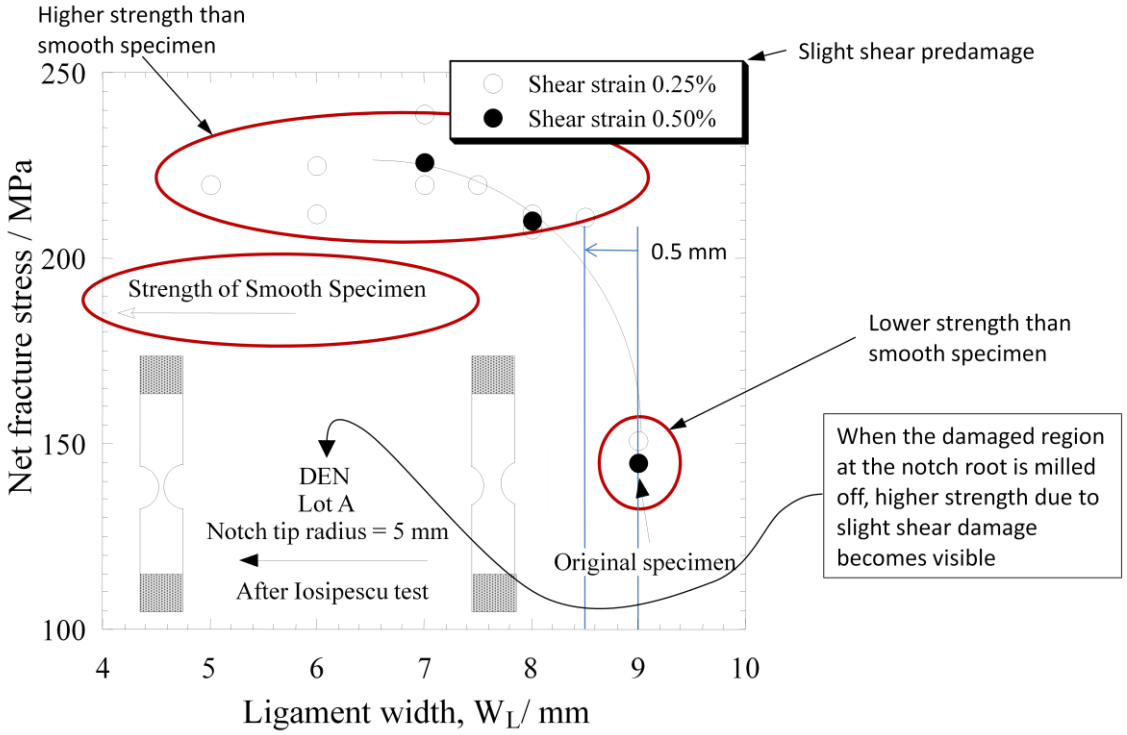

Fig. 5.8: Net tensile fracture stress of the pre-shear-loaded DEN specimen as a function of the residual ligament length after notch extension.

In the second set of experiments, a slot was engraved at the centre region of the shear-damaged specimens as shown in Figure 5.9. In this case the residual strength decreased with increasing slot width (decreasing total ligament length). This result also indicates that the fibres near the notch tips were subjected to degradation during shear loading. The strength in the fibre-damaged region should be less than 70 MPa.

Linear elastic finite element calculations had shown that the shear stress, $\tau_{xy,}$ is almost uniformly distributed along the line between the notch roots. This result indicates that uniform shear damage extended and the fibre damage in the vicinity of the notch roots should be caused by another source, probably tensile stress concentrations.

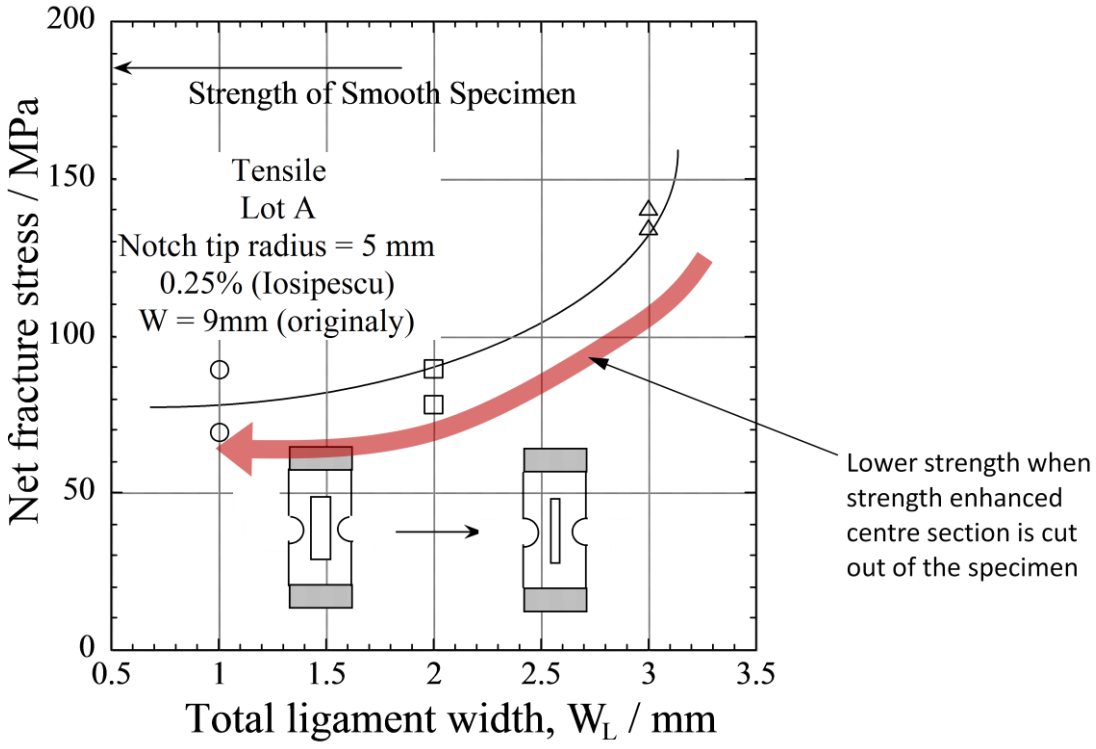

Fig. 5.9: Net tensile fracture stress of the pre-shear-loaded DEN specimen as a function of the total ligament length after engraving a slit in the centre of the specimen.

5.4.5 Bending strength of oxidation-damaged specimens

Figure 5.10 shows the bending strength of oxidation-damaged C/C as a function of the mass loss ratio, defined by the ratio of oxidized mass (δW) and initial mass (W_0). Oxidation damage was produced at temperatures up to 950 K. The bending strength was enhanced at small mass losses, but degraded at lager mass losses.

Figure 5.11 compares the micro-structure of an as-received C/C with that oxidized at 2.3% weight loss shown in Fig. 5.10 by the circled specimen. As can be seen in these photographs, the fibres and the fibre/matrix interfaces of the oxidized C/C were seriously damaged. Obviously, oxidation at first has a positive effect by damaging the fibre-matrix interface. However, under continued oxidation the fibres themselves start to suffer, reducing the strength of the C/C finally below the level of the non-oxidised reference specimens.

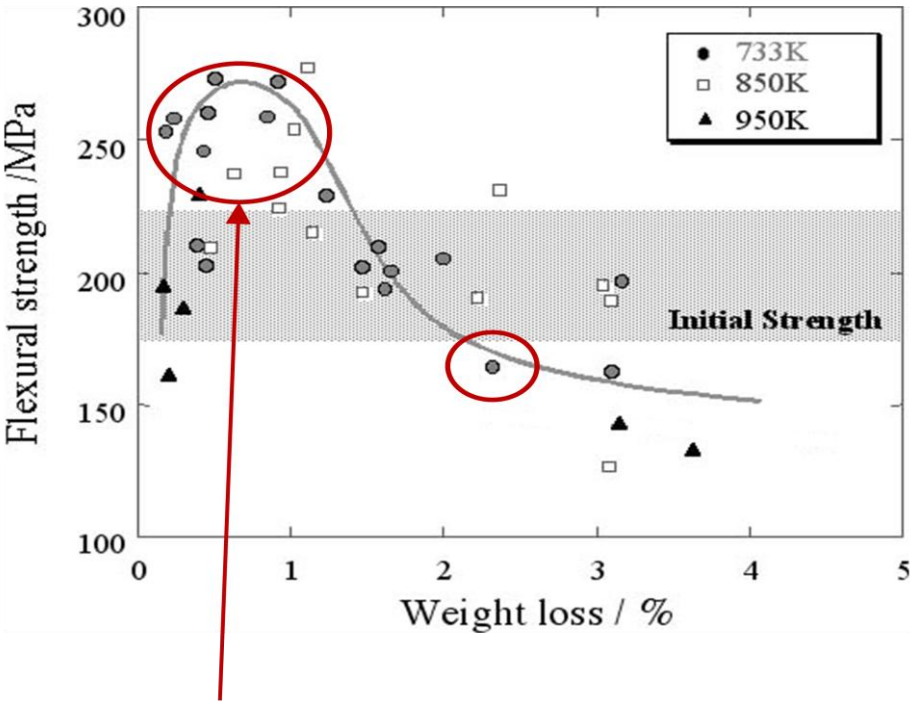

Fig. 5.10: Residual flexural stress of oxidized Lot A C/Cs as a function of mass loss during oxidation.

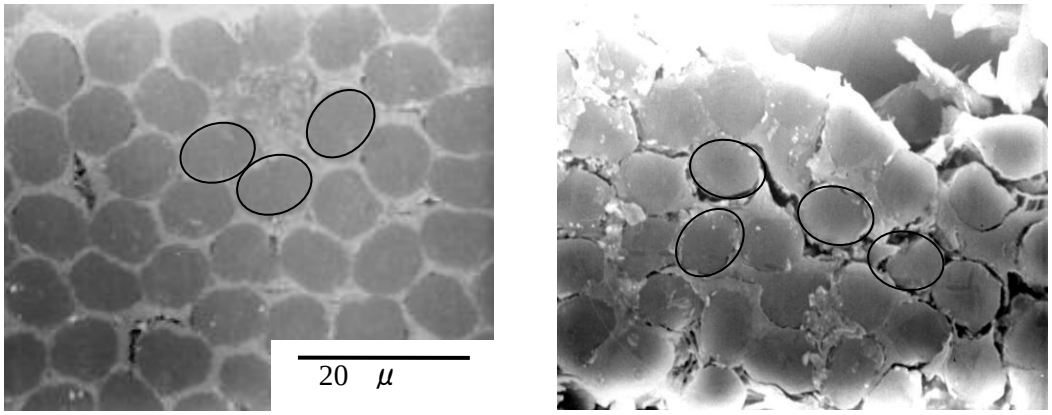

(a) Before oxidation **(b) After oxidation at 733K, weight loss 2.3%**

Fig. 5.11: SEM micro-photographs of near surface cross sections of Lot B C/C before (a) and after (b) oxidation. All circles in this figure have the same size and shape.

5.5 Discussion

The tensile strength of the carbon fibre used in this study is 2.740 GPa[132]. Using this value and the rule of mixture, the tensile strength of the C/C should be 685 MPa, if the potential fibre strength was fully exerted. However, the experimental tensile strength was about 1/3 of this value. The main reason for the degradation of the tensile strength has been assumed to be premature fibre fracture caused by the matrix cracking[133]. This suggests that the tensile strength of C/Cs has a high possibility of being increased by protecting fibres from damage of matrix cracking.

In the present study the four different damage phenomena stress concentration, fatigue, shear, and oxidation were examined. In all cases, a characteristic strength increase of the C/C composite was observed.

As pointed out above, the strength enhancement of damaged C/Cs is understandable based on the degradation of the interfacial bonding. In the case of oxidation damage, the interfacial damage could directly be observed in Figure 5.11. The interfacial damage of fatigue loaded C/Cs could be observed by the large fibre pull-out at the fracture surface[134]. Concerning shear damage, the interfacial damage between the fibre and matrix is the most plausible candidate for this loading mode[135]

5.6 Summary

We can note as summary that no matter how different the 4 damage mechanisms stress concentration, fatigue, shear, and oxidation are, all of them targeted on the fibre-matrix interface. For increasing strength one main criterion could be identified: The applied damage had to be large enough to affect substantially the fibre-matrix interface but weak enough not to harm the tensile strength of the fibres. Thus, a weak fibre-matrix interface is a main, if not to say *the* main factor to high tensile strength of C/Cs.

---

[91] M. Takabatake, Proc. 8th Symp. High Performance Mater. for Severe Environment, pp. 273-282, 1997-9, Tokyo.

[92] Y. Furukawa, H. Hatta, Y. Kogo, " Interfacial shear strength of C/C composites," Carbon, 41, 1819-1826 (2003).

[93] Chang T, Nakagawa T, Okura A. Studies on a New Manufacturing Process of Carbon Fiber Reinforced Carbon Matrix (C/C) Composites. Report of the Institute of Industrial Science, The University of Tokyo; 1991: 35(8) 1-20.

[94] D.F. Adams, D.E. Walrath, *Exper. Mech.*, 27(2), 113-119 (1987).

[95] D.F. Adams, D.E. Walrath, *Exper. Mech.*, 27(2), 113-119 (1987).

[96] Lars Denk, Hiroshi Hatta, Akihiro Misawa, Satoshi Somiya, "Shear fracture of C/C composites with variable stacking sequence", Carbon 39(10), 1505-1513 (2001).
[97] H. Hatta, Y. Kogo, H. Asano, H. Kawada, "Applicability of Fracture toughness Concept to Fracture Behavior of Carbon/Carbon Composites", *JSME Inter. J. Ser. A*, **42**(2), 265-271.
[98] K. Goto, H. Hatta, H. Takahashi, H. Kawada, "Effect of Shear Damage on the Fracture Behavior of Carbon-Carbon Composites", J. Am. Ceram Soc. 84(6) 1327-1333 (2001).
[99] M. S. Aly-Hassan, H. Hatta, S. Wakayama, M. Watanabe, K. Miyagawa, "Comparison of 2D and 3D carbon/carbon composites with respect to damage and fracture resistance," Carbon, 41, 1069-1078 (2003).
[100] K. Goto, H. Hatta, H. Takahashi, H. Kawada, "Effect of Shear Damage on the Fracture Behavior of Carbon-Carbon Composites", J. Am. Ceram Soc. 84(6) 1327-1333 (2001).
[101] M. S. Aly-Hassan, H. Hatta, S. Wakayama, M. Watanabe, K. Miyagawa, "Comparison of 2D and 3D carbon/carbon composites with respect to damage and fracture resistance," Carbon, 41, 1069-1078 (2003).
[102] Lars Denk, Hiroshi Hatta, Akihiro Misawa, Satoshi Somiya, "Shear fracture of C/C composites with variable stacking sequence", Carbon 39(10), 1505-1513 (2001).
[103] K. R. Turner, J. S. Speck and A. G. Evans, *J. Am. Ceram. Soc.*, 78(7), 1841-1848, (1995).
[104] F. E. Heredia, S. M. Spearing, T. J. Mackin, M. Y. He, A. G. Evans, P. Mosher and P. Brøndsted, *J. Am. Ceram. Soc.*, 77(11), 2817-2827, (1994).
[105] J. R. Strife, J. E. Sheehan, Ceramic Bulletine, 67(2) (1988), 369-374.
[106] E. Yasuda, S. Kimura, Y. Shibuya, Trans. JSCM, 6(1) 14-20 (1980).
[107] H. Hatta, T. Aoki, Y. Kogo, T. Yarii, "High Temperature Oxidation Behavior of the SiC-Coated C/C Composites", Composites Part A, 30, 515-520 (1999).
[108] E. Yasuda, S. Kimura, Y. Shibuya, Trans. JSCM, 6(1) 14-20 (1980).
[109] H. Hatta, T. Aoki, Y. Kogo, T. Yarii, "High Temperature Oxidation Behavior of the SiC-Coated C/C Composites", Composites Part A, 30, 515-520 (1999).
[110] C. Ahearn, B. Rand, " Modification of the Fiber-Matrix Bonding in a Brittle carbon-Carbon Composite by Controlled Oxidation", Carbon, 34(2), 239-249 (1996).
[111] E. Yasuda, S. Kimura, Y. Shibuya, Trans. JSCM, 6(1) 14-20 (1980).
[112] H. Hatta, T. Aoki, Y. Kogo, T. Yarii, "High Temperature Oxidation Behavior of the SiC-Coated C/C Composites", Composites Part A, 30, 515-520 (1999).
[113] C. Ahearn, B. Rand, " Modification of the Fiber-Matrix Bonding in a Brittle carbon-Carbon Composite by Controlled Oxidation", Carbon, 34(2), 239-249 (1996).
[114] P.L. Waker, Jr., F. Rusinko, Jr., L. G. Austin, "Gas reaction of Carbon," Advances in Catalysis, 11, 133-221 (1959).
[115] H. Hatta, T. Aoki, Y. Kogo, T. Yarii, "High Temperature Oxidation Behavior of the SiC-Coated C/C Composites", Composites Part A, 30, 515-520 (1999).
[116] C. Ahearn, B. Rand, " Modification of the Fiber-Matrix Bonding in a Brittle carbon-Carbon Composite by Controlled Oxidation", Carbon, 34(2), 239-249 (1996).
[117] P.L. Waker, Jr., F. Rusinko, Jr., L. G. Austin, "Gas reaction of Carbon," Advances in Catalysis, 11, 133-221 (1959).
[118] Y. Kogo, H. Hatta, H. Kawada and T. Machida, "Effect of Stress Concentration on Tensile Fracture Behavior of Carbon-Carbon Composites", *J. Comp. Mater.*, 32 [13], 1273-1294 (1998).

[119] Y. Kogo, H. Hatta, H. Kawada and T. Machida, "Effect of Stress Concentration on Tensile Fracture Behavior of Carbon-Carbon Composites", *J. Comp. Mater.*, 32 [13], 1273-1294 (1998).

[120] H. Hatta, K. Suzuki, T. Shigei, S. Somiya, Y. Sawada, "Strength Improvement by Densification of C/C Composites", Carbon, 39, 83-90 (2001).

[121] M. S. Aly-Hassan, H. Hatta, S. Wakayama, M. Watanabe, K. Miyagawa, "Comparison of 2D and 3D carbon/carbon composites with respect to damage and fracture resistance," Carbon, 41, 1069-1078 (2003).

[122] Lars Denk, Hiroshi Hatta, Akihiro Misawa, Satoshi Somiya, "Shear fracture of C/C composites with variable stacking sequence", Carbon 39(10), 1505-1513 (2001).

[123] H. Hatta, Y. Kogo, H. Asano, H. Kawada, "Applicability of Fracture toughness Concept to Fracture Behavior of Carbon/Carbon Composites", *JSME Inter. J. Ser. A*, **42**(2), 265-271.

[124] Y. Kogo, H. Hatta, H. Kawada and T. Machida, "Effect of Stress Concentration on Tensile Fracture Behavior of Carbon-Carbon Composites", *J. Comp. Mater.*, 32 [13], 1273-1294 (1998).

[125] K. Goto, H. Hatta, H. Takahashi, H. Kawada, "Effect of Shear Damage on the Fracture Behavior of Carbon-Carbon Composites", J. Am. Ceram Soc. 84(6) 1327-1333 (2001).

[126] M. S. Aly-Hassan, H. Hatta, S. Wakayama, M. Watanabe, K. Miyagawa, "Comparison of 2D and 3D carbon/carbon composites with respect to damage and fracture resistance," Carbon, 41, 1069-1078 (2003).

[127] M. S. Aly-Hassan, H. Hatta, S. Wakayama, M. Watanabe, K. Miyagawa, "Comparison of 2D and 3D carbon/carbon composites with respect to damage and fracture resistance," Carbon, 41, 1069-1078 (2003).

[128] M. Mizuno, S. Zhu, Y. Nagano, Y. Sakaida, Y. Kagawa and M. Watanabe, "Cyclic-Fatigue Behavior of SiC/SiC Composites at Room and High Temperatures," J. Am. Ceram. Soc., 79, [12], 3065-3077, (1996).

[129] N. Chawla, Y. K. Tur, J. W. Holmes, J. R. Barber and A. Szweda, "High-Frequency Fatigue Behavior of Woven-Fiber-Fabric-Reinforced Polymer-Derived Ceramic-Matrix Composites," J. Am. Ceram. Soc., 8, [5], 1221-1230, (1998).

[130] K. Goto, H. Hatta, D. Katsu, T. Machida, " Tensile Fatigue of a laminated carbon-carbon composite at room temperature," Carbon, 41, 1249-1255 (2003).

[131] K. Goto, H. Hatta, D. Katsu, T. Machida, " Tensile Fatigue of a laminated carbon-carbon composite at room temperature," Carbon, 41, 1249-1255 (2003).

[132] TORAYCA® Catalogue, Toray Co. Ltd., (1997).

[133] M. Takabatake, Proc. 8th Symp. High Performance Mater. for Severe Environment, pp. 273-282, 1997-9, Tokyo.

[134] K. Goto, H. Hatta, D. Katsu, T. Machida, " Tensile Fatigue of a laminated carbon-carbon composite at room temperature," Carbon, 41, 1249-1255 (2003).

[135] Lars Denk, Hiroshi Hatta, Akihiro Misawa, Satoshi Somiya, "Shear fracture of C/C composites with variable stacking sequence", Carbon 39(10), 1505-1513 (2001).

6. Tensile fracture behaviour

6.1 Introduction

In chapters 4 and 5, several kinds of damage were applied to the C/C composite and high strength behaviour could be observed. All damage sources targeted at the interface between fibre and matrix. This leads to the conclusion, that the interface between fibre and matrix is the ruling parameter determining the tensile strength of the C/C composite. A major question focuses on the way, in which the fibre-matrix interface affects the strength of C/C composites.

The fibre-matrix' interface is known to change by the degree of graphitization. Since the graphitization depends on the heat treatment temperature, C/C material with various different heat treatment temperatures was examined.

The procedure was as follows: C/C was graphitized at several temperatures between approximately 1200 K and 3200 K. Then, tensile tests were carried out. In another test series, fibre bundle push out tests with the same materials were performed to measure the interfacial strength between fibre and matrix. The interfacial strength was then related to the tensile strength of the same material. To analyse the fibre-matrix interface, the fracture surface was inspected by SEM.

6.2 Experimental procedure

6.2.1 Material

Other than in the previous cases, the examined C/C was produced by the liquid precursor route. The source material was a carbon fibre reinforced plastic (CFRP) with a matrix out of phenolic resin reinforced with a pitch based carbon fibre K 633, supplied by Mitsubishi Sanshi Co. The CFRP was carbonized at 1273 K. The resulting porous material was densified by 5 cycles of the hot iso-static pressuring process (HIP) with coal tar pitch at 893 K and 100 MPa pressure. Then, the material was separated into several batches and each batch was graphitized at a different final heat treatment temperature between 1273 K and 3173 K. During heat treatment, the temperature increased at 10 K / min, the holding time at the peak temperature was 1 hour and the cooling rate was less than 10 K / min. The final fibre volume fraction v_f was in all cases 0.6 and the thickness *t* approximately 1.5 mm.

6.2.2 Tensile fracture tests

Tensile fracture tests were carried out to determine the material's ultimate tensile strength after final heat treatment with a specimen configuration shown in Fig. 6.1.

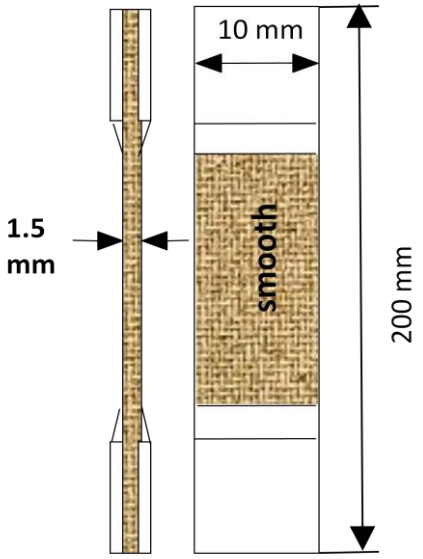

Fig. 6.1: Specimen geometry for tensile tests.

The specimens had a straight coupon type geometry with a length and width of 200 mm and 10 mm, respectively, and a thickness of 1.5 mm. Aluminium tabs were glued on the sides of both ends of the specimen to avoid damage of the material and to improve gripping. Tensile tests were carried out by a screw driven Shimadzu AG-5000A tensile testing machine at room temperature under a crosshead speed of 0.1 mm/min. Strain gages were glued on both sides during testing to monitor stress-strain behaviour.

6.2.3 Fibre bundle push-out tests

In addition to tensile testing, fibre bundle push-out tests were carried out after heat treatment to evaluate the interfacial shear strength. In this test, a specimen with a thickness of t = 100 μm and fibres oriented in thickness direction was placed on the base plate of a fibre bundle push-out test fixture shown in Fig. 6.2. An intender with a diameter of approx. 50 μm was located on top of the specimen pushing out a fibre bundle of approx. 30 fibres under a test speed of 0.1 mm/min at room temperature. The test fixture was mounted to a screw driven test machine of the type Orientech RTM 25. The Load and displacement were monitored by a load cell and displacement sensor, and the push

out test was observed by means of a CCD camera. The interfacial debonding strength τ_i was calculated by the formula

$$\tau_i = F_{max} \cdot L \cdot t \tag{6.1}$$

with F_{max}, L, and t denoting the push-out force, the specimen thickness, which is equivalent to the fibre length, and the debonded bundle's peripheral length, respectively.

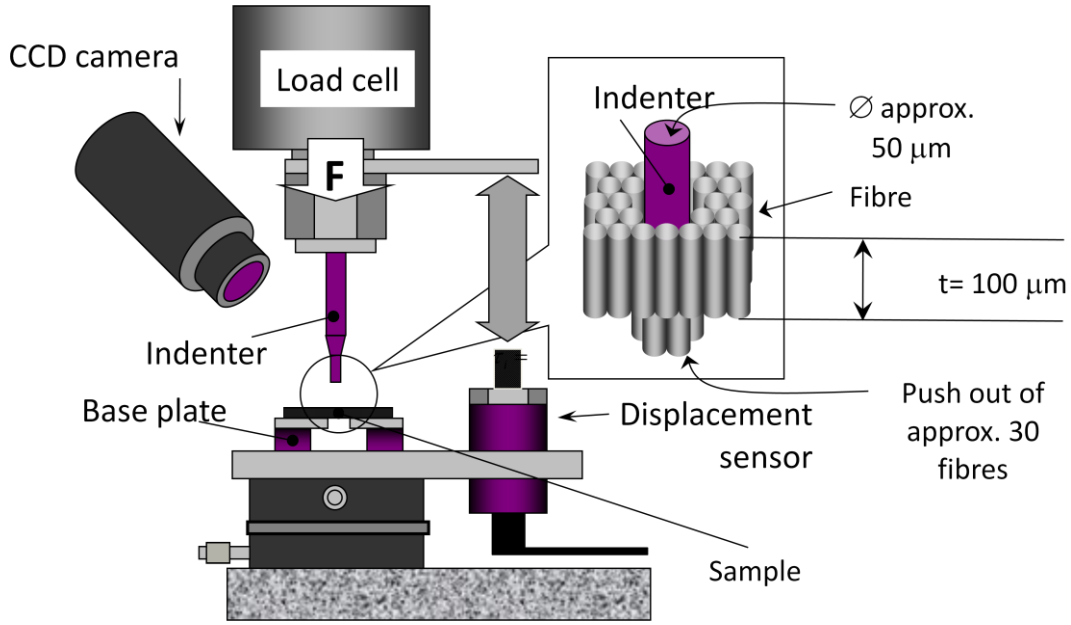

Fig. 6.2: Fibre bundle push-out test fixture.

6.3 Results

As mentioned in the previous chapter, the ultimate tensile strain of the C/C composites (ε_{ult}), about 0.2~0.4%, is generally much lower than that of their reinforcing carbon fibres, 0.65~1.5%. This low ε_{ult} is believed to be caused by the constraint of the matrix, i.e., the ε_{ult} of C/Cs being nearly equal to that of the matrices [1 3 6]. Hence, if the matrix constraint is released for example by interfacial damage, the ε_{ult} of C/Cs can be recovered towards that of the reinforcing fibre leading to higher strength. Keeping this in mind, the following discussion will be carried out on the basis of the tensile fracture strain ration r_{eu}

$$r_{eu} = \frac{\varepsilon_{ult}}{\varepsilon_{fibre}} \tag{6.2}$$

with ε_{ult} and ε_{fibre} denoting the ultimate tensile strain of the C/C and the fracture strain of the fibre, respectively.

The results of tensile and fibre bundle push-out tests are shown in Fig. 6.3 as a function of the heat-treatment temperature (HTT) in K. In this figure, the tensile test results are arranged on the left horizontal axis in terms of the tensile fracture strain ratio r_{eu}, and in terms of interfacial debonding stress τ_i on the right. The graph shows the clear relationship between the interfacial strength and strain degradation. High interfacial strength goes along with a high degree of strain degradation, represented in Fig. 6.3 as a low tensile fracture strain ratio r_{eu}. On the other hand, when the interfacial debonding strength is low, the C/C's fracture strain reaches nearly 70% of the fibres fracture strain.

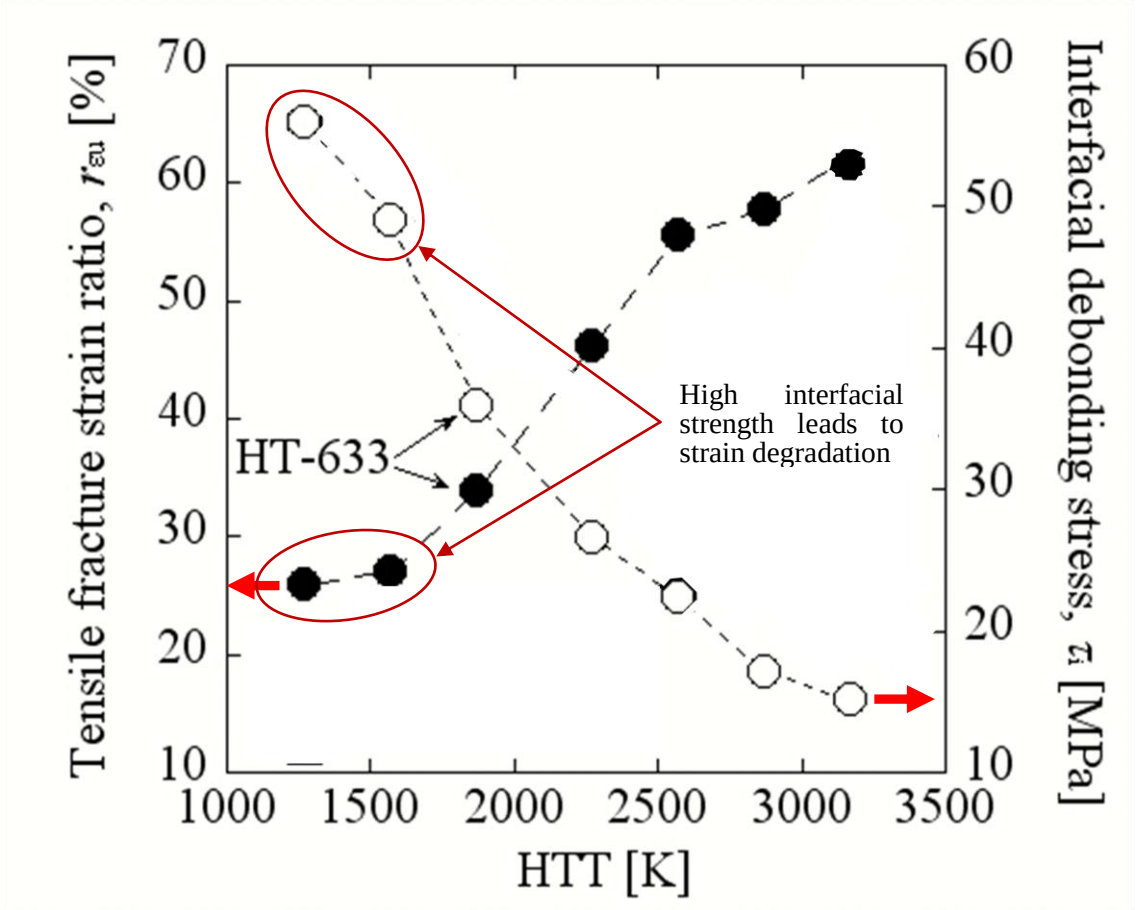

Fig. 6.3: Tensile fracture strain ratio r_{eu} ● interfacial debonding stress τ_i ○ as a function of the heat treatment temperature (HTT).

Fig. 6.4 shows the SEM picture of a typical fracture surface of a tensile-fractured HT633 C/C heat-treated at 1273 K. The characteristic feature in this picture is the nearly uniform fracture surface of lager segments which we will call in the following fibre bundles (FB). The fracture in bundles is a consequence of the carbon fibre's material

properties.

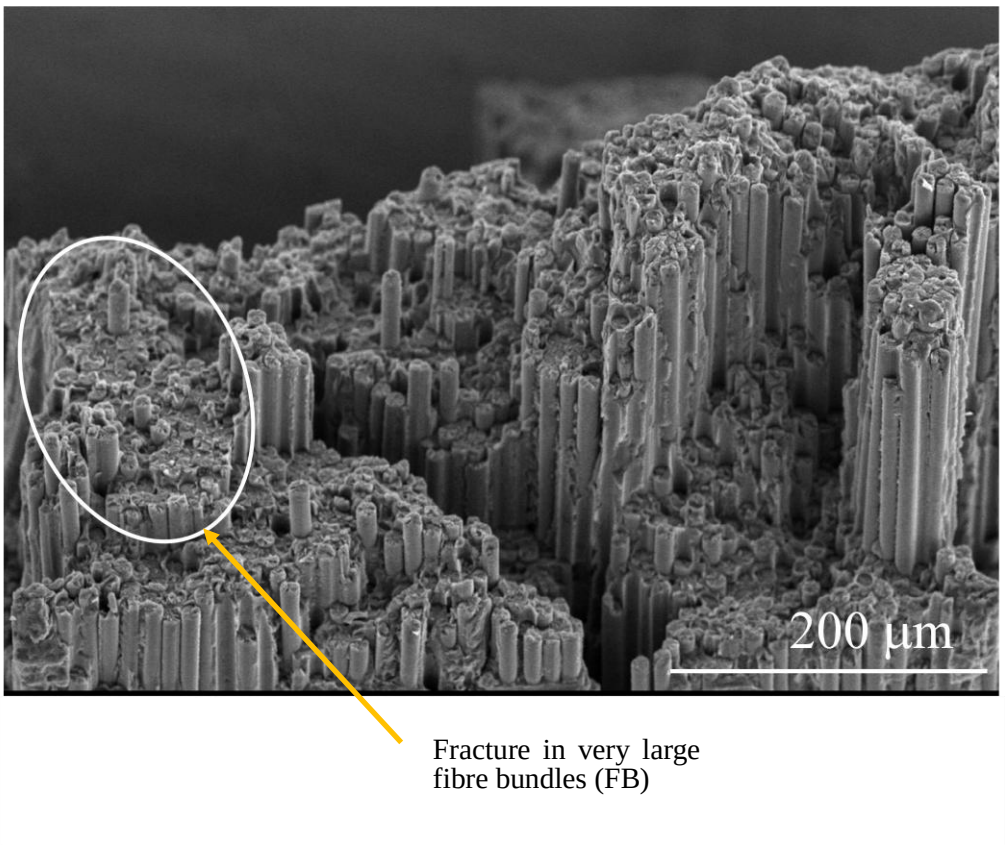

Fig. 6.4: Typical fracture surfaces of a tensile-fractured HT633 **C/C** heat-treated at 1273K

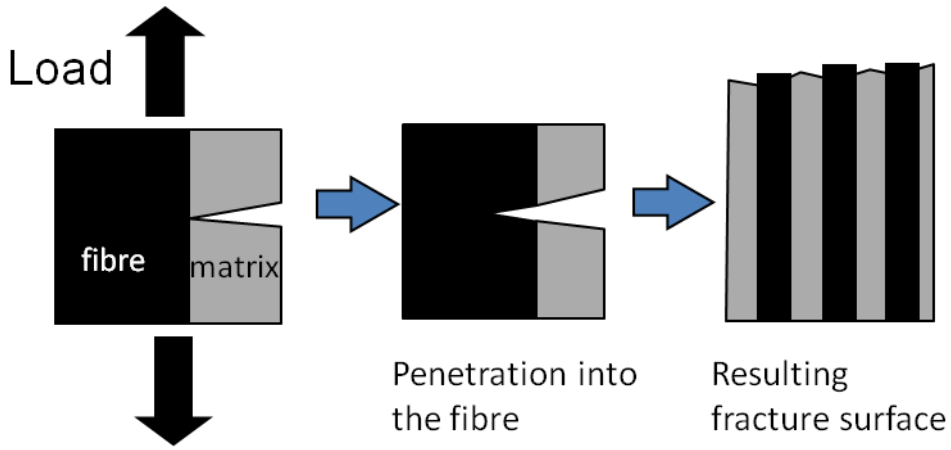

Fig. 6.5: Crack propagation at the fibre-matrix interface. Due to the fibre's low toughness fibre fracture in one bundle will continue until all fibres are fractured.

When a crack propagates the fibre-matrix interface as shown in Fig. 6.5, the crack will continue to penetrate into the fibre due to the fibre's low toughness. This process will

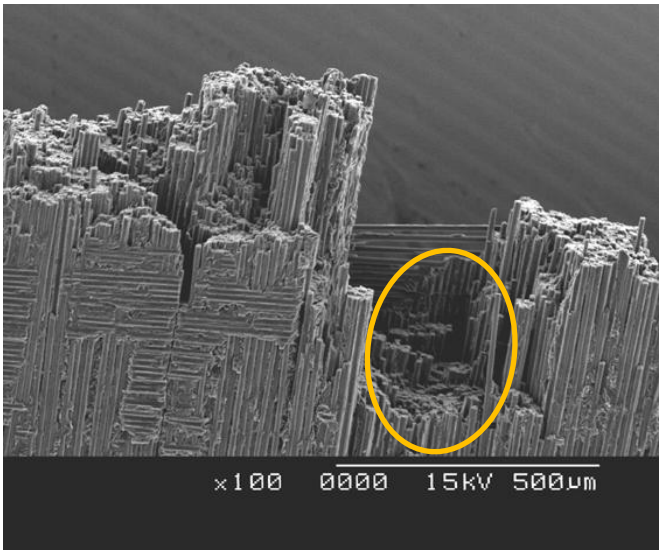

Fig. 6.6: (HTT): 1273K, t_i: 49MPa. Fracture occurs in very large fibre bundles (FB)

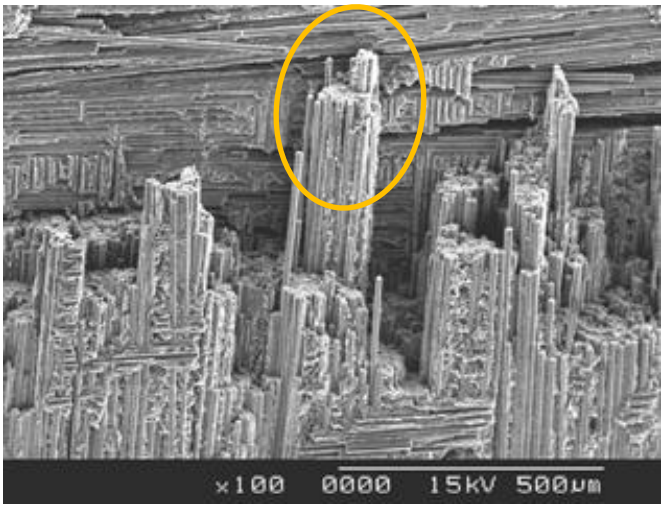

Fig. 6.7: (HTT): 2273K, t_i: 25MPa. Fracture occurs in larger fibre bundles (FB)

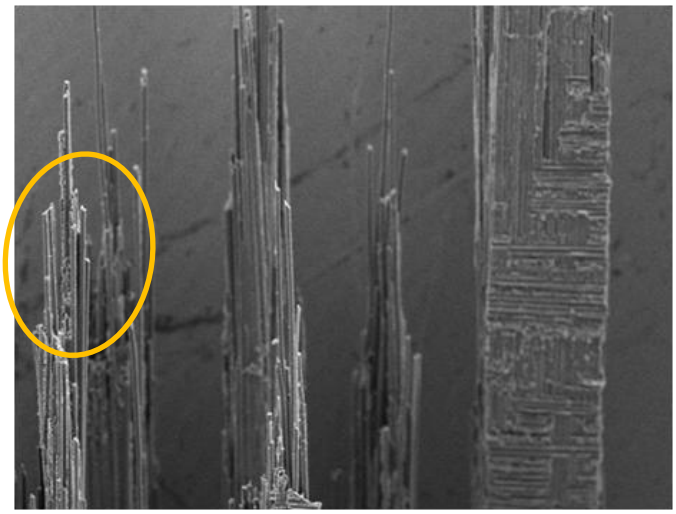

Fig. 6.8: (HTT): 3173K, t_i: 13MPa. Fracture occurs in small fibre bundles (FB)

continue, until all fibres of one fibre bundle are fractured. Figs. 6.6 – 6.8 show the

fracture surfaces of C/Cs treated with heat treatment temperatures (HTT) of 1273 K (Fig. 6.6), 2273 K (Fig. 6.7), and 3173 K (Fig. 6.8). Despite the already above mentioned feature, that the interfacial shear strength decreases with heat treatment temperature, all fracture surfaces show nearly the same pattern. However, the fibre bundle size differs significantly with heat treatment temperature and the corresponding interfacial shear strength: The lower the interfacial shear strength (e.g., the higher the heat treatment temperature), the less fibres fracture per bundle. In other words, the fibre bundles (FB) size at fracture decrease with decreasing interfacial shear strength.

6.4 Discussion

In the previous section, interfacial shear strength was related to the fibre bundle (FB) size and we found that smaller fibre bundles lead to higher tensile strength. When considering the source of this mechanism we have to consider two opposing cases as

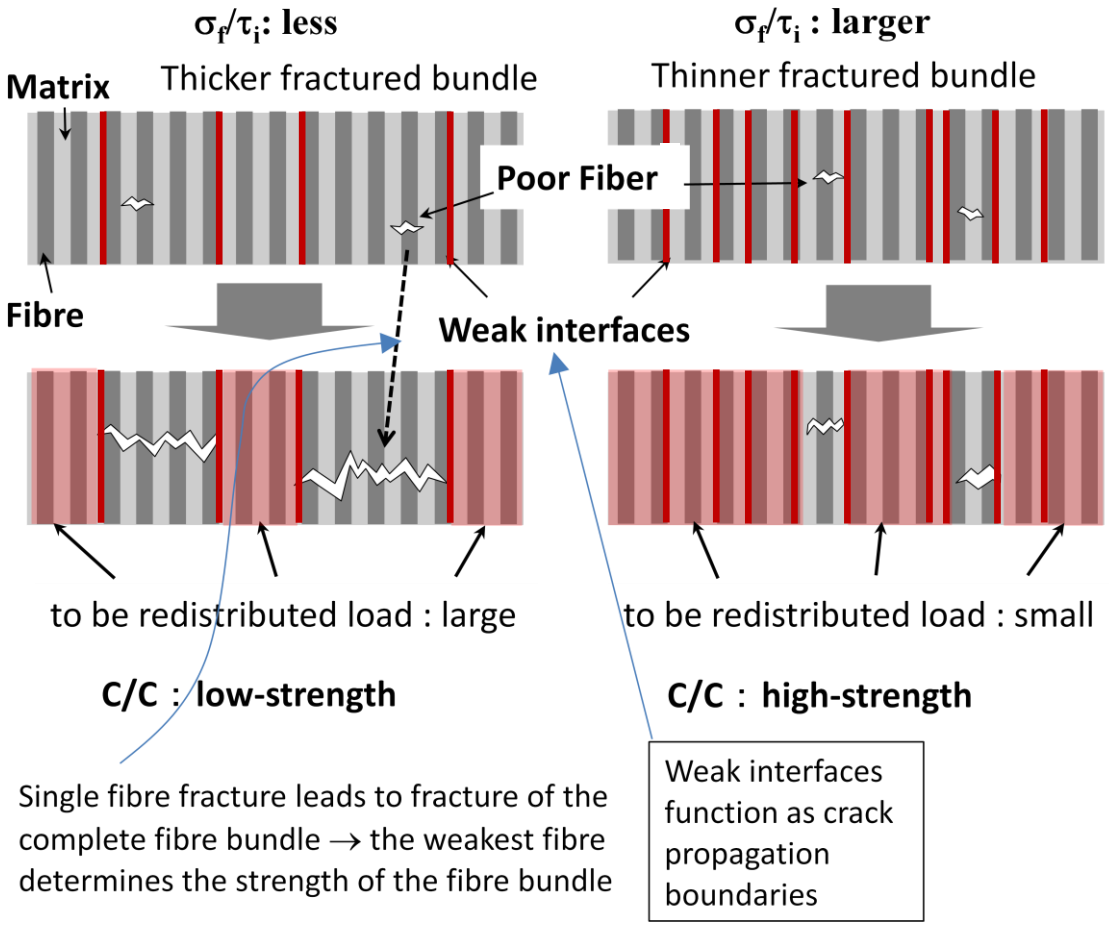

Fig. 6.9: Crack propagation boundary model.

shown in Fig. 6.9. In this figure on the left, a C/C composite with a large fibre bundle (FB) size is shown compared to specimen with a small fibre bundle size on the right. The main difference between the two is that the specimen on the right with a smaller fibre bundle size and lower interfacial strength possesses many more weak interfaces. Recalling that fracture within one bundle will continue until the last fibre has failed, these weak interfaces function as crack propagation boundaries. Thus, the crack propagation boundaries prevent the crack front from entering into neighbouring fibre bundles.

We have to take into consideration that the fibres do not possess uniform strength. In particular, some of the fibres might be weak for various reasons. As the loading increases, these fibres are especially prone to early fracture. Considering, that this early single fibre fracture leads to the fracture of the whole fibre bundle, we can observe a significant difference between the two configurations of Fig. 6.9:

The weak interfaces lead to smaller fibre bundles. Thus, in case of fibre fracture and resulting bundle failure, the load which has to be redistributed among all surviving fibre bundles is much small than in case of the failure of large fibre bundles. Consequently, the fibre bundles in the vicinity of a fractured small fibre bundle will not suffer from a drastic stress increase and are therefore more likely to sustain additional loads. For this reason, C/Cs with weak interfaces reveals a higher strength that those with strong fibre-matrix interfaces even if the specimen's fibres posses the same tensile strength.

6.5 Summary

Examined C/Cs with higher heat treatment temperature revealed lower interfacial strength and smaller fibre bundles fracture than those with lower treatment temperature. The smaller fibre bundles resulted from a larger amount of weak fibre-matrix interfaces. Single fibre fracture inevitably leads to the fracture of the whole fibre bundle due to the weak toughness of the C/C fibres. The weak fibre-matrix interfaces function as crack propagation boundaries preventing the crack front from entering into adjacent fibre bundles. In case of fracture of bundles, the load to be redistributed among all surviving fibre bundles is smaller if the fractured bundles themselves are small. For this reason the surviving bundles are more likely to sustain additional loads than those in the vicinity of a large bundle. This mechanism leads to the higher strength of the small fibre bundle configuration.

[136] M. Takabatake, Proc. 8th Symp. High Performance Mater. for Severe Environment, pp. 273-282, 1997-9, Tokyo.

7. Analysis of holed specimen

7.1 Introduction

The notch sensitive/insensitive behaviour of carbon-carbon (C/C) composites has received broad attention in the C/C research community[18-33]. Several investigations have been carried out, based on the analytical or experimental examination of single or double-edge notched (DEN) specimens. In some of these investigations [137,138] anomalous fracture behaviour was observed when the specimen's width was narrow, as shown in Fig 7.1. This figure was obtained by fixing the ratio of the notch length, *a*, and the specimen's width, *w*, to $2a/w = 0.5$ and by systematically changing *w*.

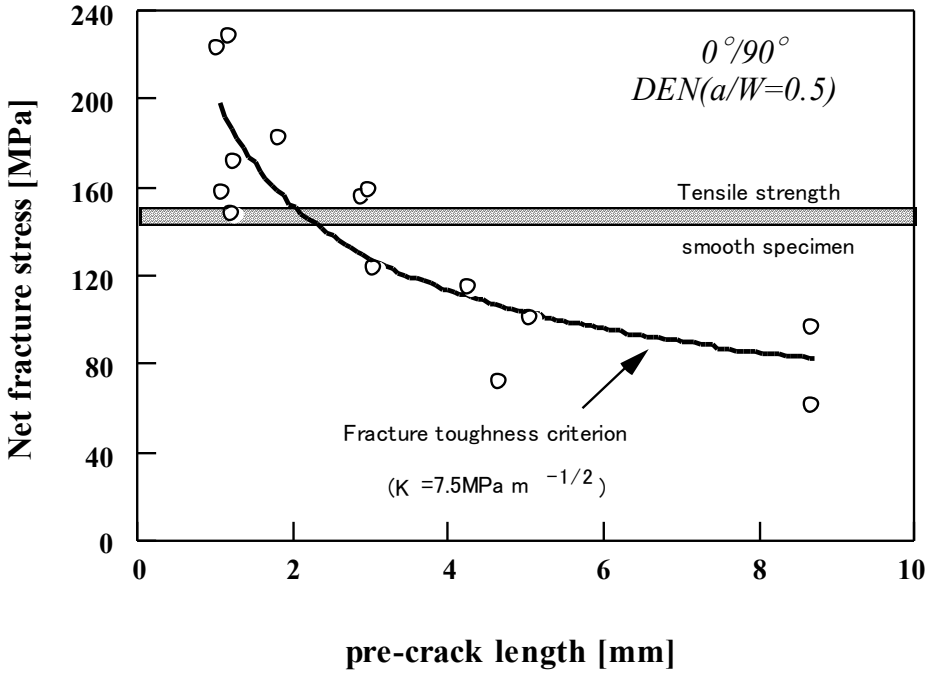

Fig. 7.1: Net fracture stress of double-edge-notched (DEN) C/Cs fitted by a constant toughness line of 7.5 MPa $m^{-1/2}$ (solid line) and compared with the tensile strength of smooth specimens (shaded region).

When *a* is small, the net fracture stress $\sigma_{f,net}$ of the notched specimens was much higher than the tensile strength of smooth specimens, σ_0 as shown by the shaded region. In ordinary materials, this behaviour might be difficult to understand. However, in case of C/C composites, high strength behaviour can be easily explained in some occasions. The ultimate tensile strain of C/C composites (≈0.2%) is usually much lower than that

of the constituent fibres (0.65~1.2%), and this strain degradation is believed to be caused by the constraint of the matrix[139]. Hence, if this constraint is relaxed, the ultimate strain of C/C composites eventually increases towards the original higher value of the reinforcing fibres. We considered that high strength is induced in double-edge notched specimens when the damage zones extending from both notch roots unite thus covering the whole ligament. The damage in the C/C composite possibly relieves in this situation the matrix constraint of the fibres.

The present study was motivated by the above mentioned observation and was carried out for two purposes: The first aim was to find the optimum arrangement of holes in multi-holed specimens under tensile loading. The second one was to discuss the origin of this high strength behaviour in relation to the damage zone formation at the notch tips and the weak shear strength characteristics of the C/C composites. Since the mechanical response in the damage zone near the hole seems to dictate the notch sensitive/insensitive behaviour of C/C composites, it is quite important for the design of actual C/C structures to understand the behaviour in the damage zone.

7.2 Experimental procedure

7.2.1 Material

The carbon-carbon composite used in this study was of cross-ply laminate type, made by means of the preformed yarn process[140], and supplied by Across Co. Ltd. It consisted of 16 layers of uni-directionally reinforced laminae arranged in a symmetrical 0°/90° stacking sequence with a total thickness of 3 mm. The reinforcing fibres were PAN based high modulus type TORAYCA® M40 with 6000 fibres per bundle giving a total nominal fibre fraction of 0.5.

7.2.2 Tensile fracture tests of multi-holed specimens

In previous experiments with single-holed specimens[141], particularly high net fracture stresses were observed when the specimens had relatively small holes with a fixed diameter of 2 mm and a short ligament length. Thus, similar configurations were used in this experiment as shown in Fig. 7.2.

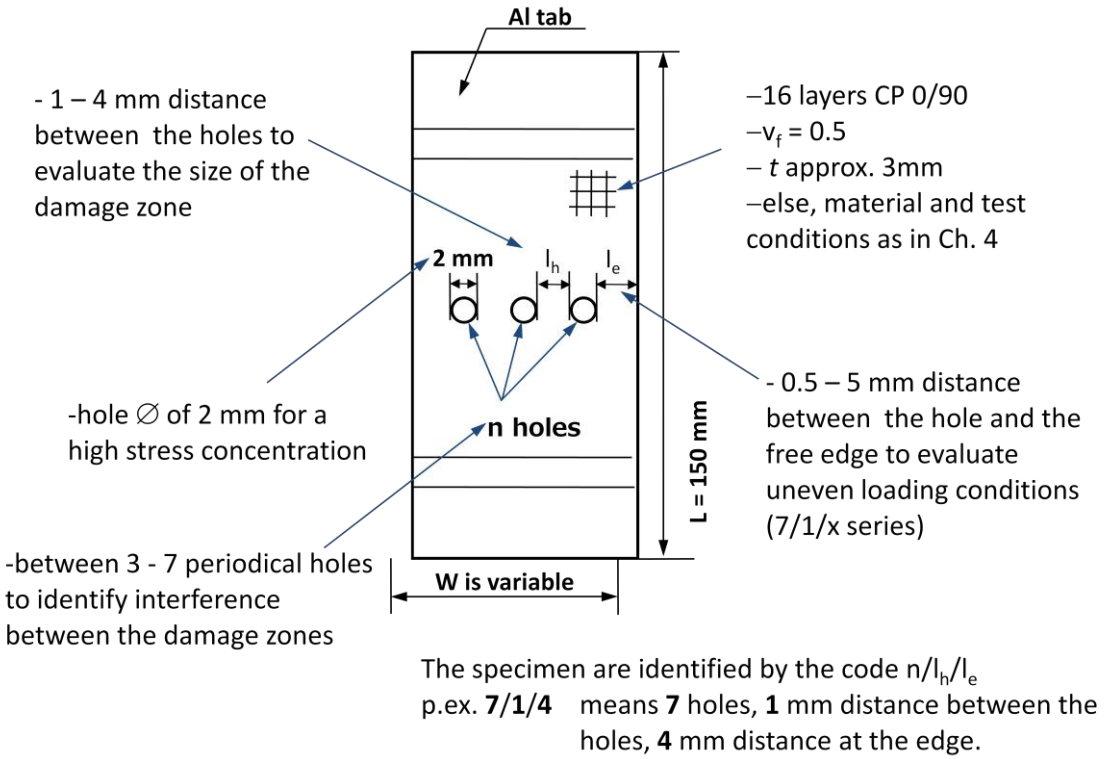

Fig. 7.2: Configuration of specimens.

The geometrical features of the specimens are summarised in Table 7.1, where l_h, l_e, and n denote the distance between adjacent holes, the distance between the most outer hole and the free edge, and the number of holes. Hereafter, the series of the three figures n/ l_h/ l_e and assigned symbols will be used to identify the specimen geometry. During drilling, the surfaces of the specimens were protected by wood layers to avoid delamination. The prepared specimens were then inspected by microscope and delaminated specimens were rejected. Aluminium tabs were attached on both sides of the specimen to reduce the stress concentration and to avoid damage during gripping. 3 to 7 samples in each configuration were fractured.

All tensile tests were performed by use of an electromechanical testing machine (Shimadzu AG-5000A) under a crosshead speed of 0.1 mm/min.

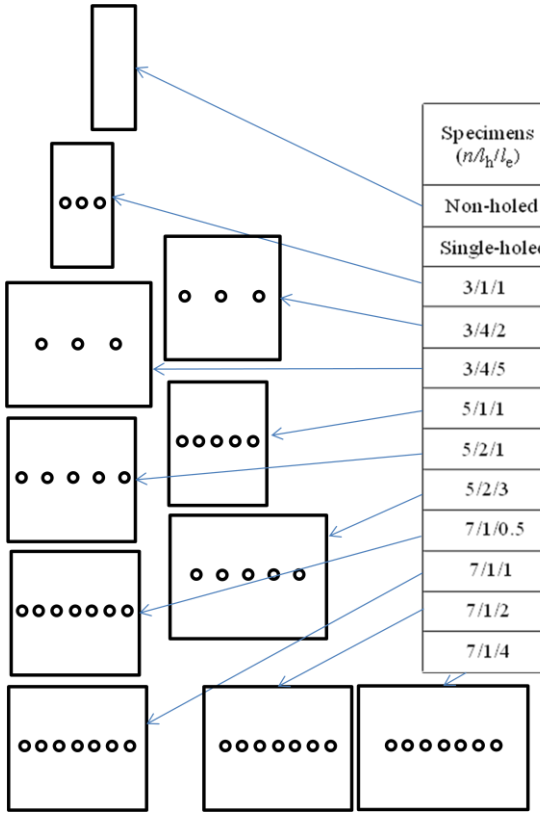

Specimens (n/l_h/l_e)	Number of Holes n	Hole distance l_h (mm)	Edge distance l_e (mm)	Width W (mm)	Mark
Non-holed	0	n/a	n/a	20	⊞
Single-holed	1	n/a	11	24	×
3/1/1	3	1	1	10	▼
3/4/2	3	4	2	18	◆
3/4/5	3	4	5	24	◇
5/1/1	5	1	1	10	▽
5/2/1	5	2	1	20	▲
5/2/3	5	2	3	24	△
7/1/0.5	7	1	0.5	21	■
7/1/1	7	1	1	22	□
7/1/2	7	1	2	24	○
7/1/4	7	1	4	28	●

Table 7.1: Specimen geometry.

7.3 Finite Element (FEM) analysis

7.3.1 Linear FEM

Finite element calculations of the stress distributions during tensile tests of the multi-holed specimens were carried out by use of ABAQUS® with a two dimensional orthotropic model assuming plane stress. The models consisted of between 1200 and 5600 8-node-points iso-parametric elements. Tensile and shear stress distributions near the hole in linear elastic cases were determined using the orthotropic material constants

$$E_{xx} = E_{yy} = 96.5 \text{ GPa}, \qquad \nu_{xy} = 0.026, \qquad G_{xy} = 5.4 \text{ GPa}$$

where E, ν, and G denoted the Young's modulus, the Poisson's ratio, the shear modulus, and the lower case indices y and x stand for the loading and normal directions, respectively. The tensile material constants were obtained from experiments described in section 3.2, and the shear modulus was determined from the initial slope of the shear stress-strain curve recorded from shear experiments as described in section 4.3.2.

7.3.2 Non-linear FEM

As described in section 4, C/C composites exhibit low shear strength and a strong non-linear stress-strain curve. To study the effect of low shear strength and non-linear shear stress-strain behaviour on stress concentration points like holes, non-linear FEM was carried out. Using the same grid pattern as described above the shear stress-strain behaviour was modelled up to γ_{12} = 2% by equ. 4.9,

$$\tau_{12} = 5{,}4 \text{ GPa } \gamma_{12} - 230 \text{ GPa } \gamma_{12}^2, \qquad (4.9)$$

giving the shear stress-strain relationship as shown in Fig. 7.3.

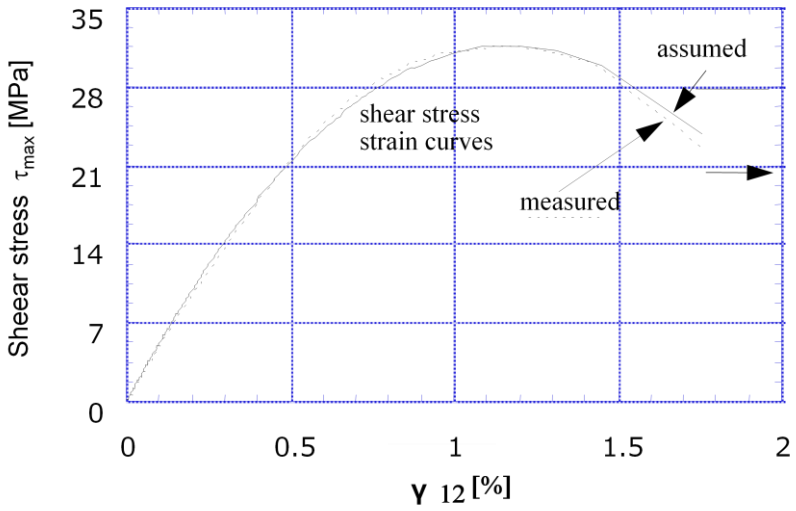

Fig. 7.3: Normalized tensile fracture stress as a function of shear preloading.

For strains above γ_{12} = 2%, the shear stress was limited to roughly $\tau_{12} \approx 20$ MPa. The tensile stress–strain relationship was assumed to be linear. In the non-linear finite element calculations, the tensile load was increased in 20 steps and the shear modulus G_{xy} changed depending on the local shear strain of the previous step by equ. 4.8.

$$G_{12} = 5{,}4 \text{ GPa} - 230 \text{ GPa } \gamma_{12} \qquad (4.8)$$

7.4 Results

7.4.1 Tensile test results of the multi-holed specimen

The tensile fracture test results of all multi-holed specimens are shown in Fig. 6.4 in terms of net fracture stress

$$\sigma_{f,net} = F_f / A_{net} \qquad (7.1)$$

with F_f and A_{net} denoting the fracture load and the net sectional area, respectively. The data is arranged as a function of l_h/l_e. l_h denotes in this figure the distance between adjacent holes, and l_e the distance between the most outer hole and the free edge. As we can see in Fig. 7.4, the net fracture stress $\sigma_{f,net}$ reached a maximum at $l_h/l_e = 1$, and exceeded at this point the strength of smooth specimens (186 MPa) significantly. Hence, the optimum arrangement is located in this area. It follows from this figure that $\sigma_{f,net}$ depends approximately only on the ratio l_h/l_e, which implies that $\sigma_{f,net}$ is insensitive to the hole number n and to the individual ligament lengths l_h *or* l_e.

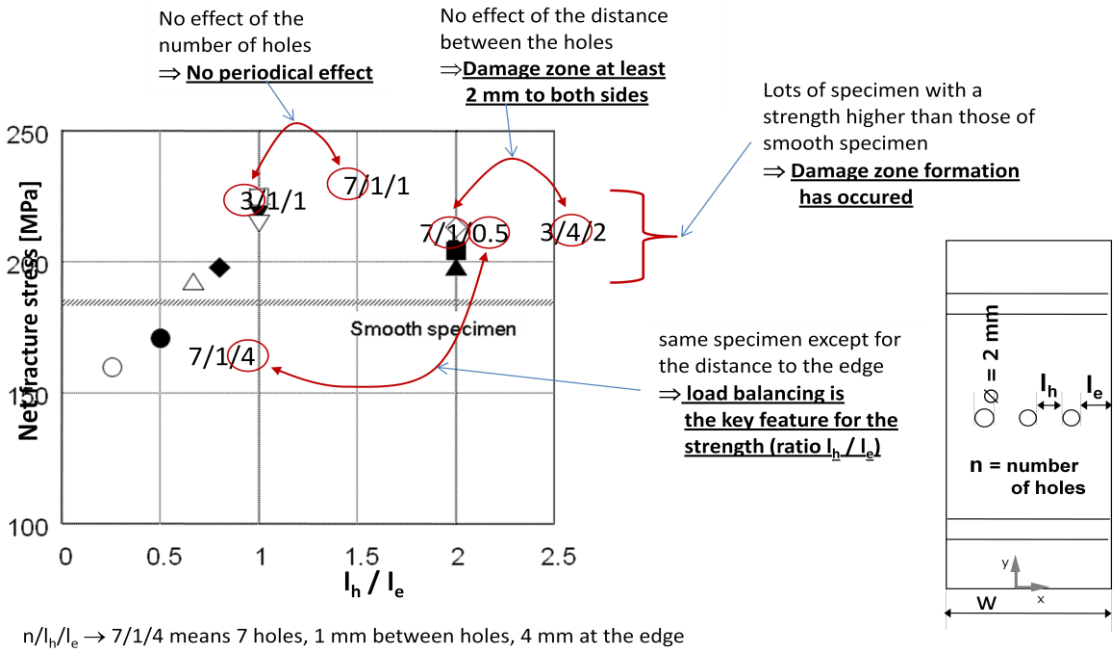

Fig. 7.4: Tensile net fracture stress $\sigma_{f,net}$ of multi-holed specimens.

7.4.2 Simplification of multi-holed geometry

In the previous chapter, we found that the load balancing between the hole and the edge elements is the key feature for the strength of the C/C composite. To study this phenomenon more in detail, let us consider a multi-holed 3/2/5 structure as shown in Fig. 7.5. The holes drilled into the centre section of the specimen lead to a reduction in load bearing area in the ligament. However, due to the different widths at the edge (W_e) and hole (W_h), the proportional loss of load bearing area is not the same in all ligament sections. In particular, the relatively wide edge section in Fig. 7.5 suffers only from a reduction of load bearing area of 20 % (from a gross width of 5 mm to a net width of 4 mm). The centre sections on the other hand lose 50 % of the load bearing area (from 2 mm to 1 mm). Thus, the stress in the centre sections is significantly larger than at the edge and fracture will therefore occur in the centre. Consequently, we must look at single ligament sections and analyse those with the highest relative loss of load bearing area, e.g. the highest stressed ligament.

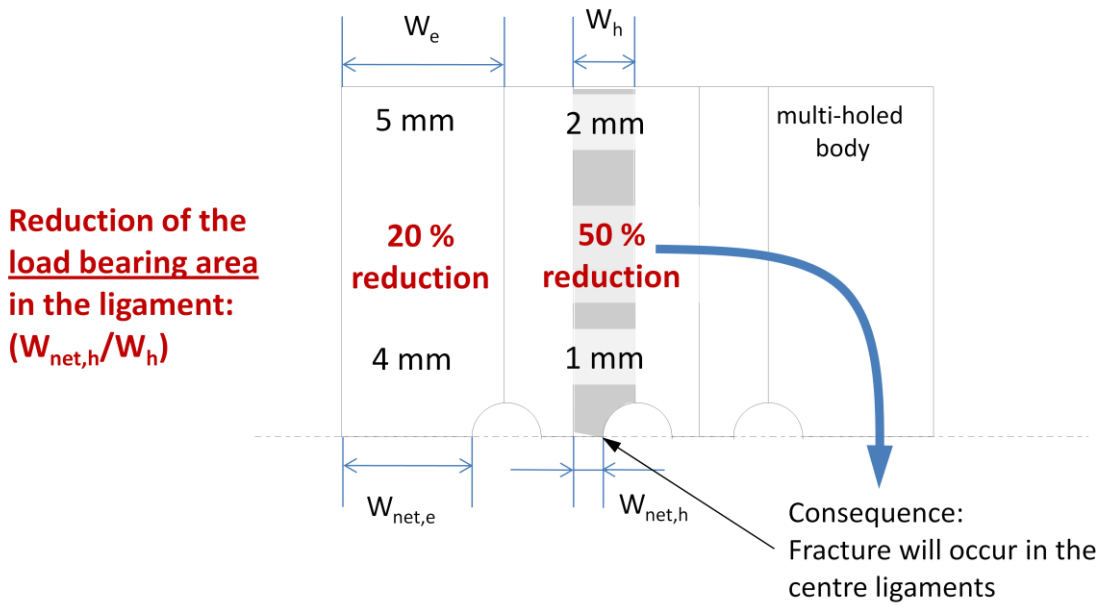

Fig. 7.5: Load balancing problem of a multi-holed 3/2/5 specimen.

Since we have to look at single ligament sections, let us introduce a model separating the whole multi holed body into single holed bodies, as shown in Fig. 7.6. In this model, the edge sub-elements are modelled by a single-centre-holed body with free

boundaries at both sides. In contrast, the centre sub-elements are modelled by a single centre-holed body with straight boundaries on the sides[1 4 2]. To these reduced models, the same gross average stress $\sigma_{gr,ave}$ was applied resulting in different net average stresses $\sigma_{net,ave}$ in the ligament section at the holes, which depend only on the ratio of the ligament width w_{net} and the gross width w of the individual sub-elements, e.g.

$$\sigma_{net,ave} = \sigma_{gr,ave} \times {}^{w}\!/_{w_{net}} . \qquad (7.2)$$

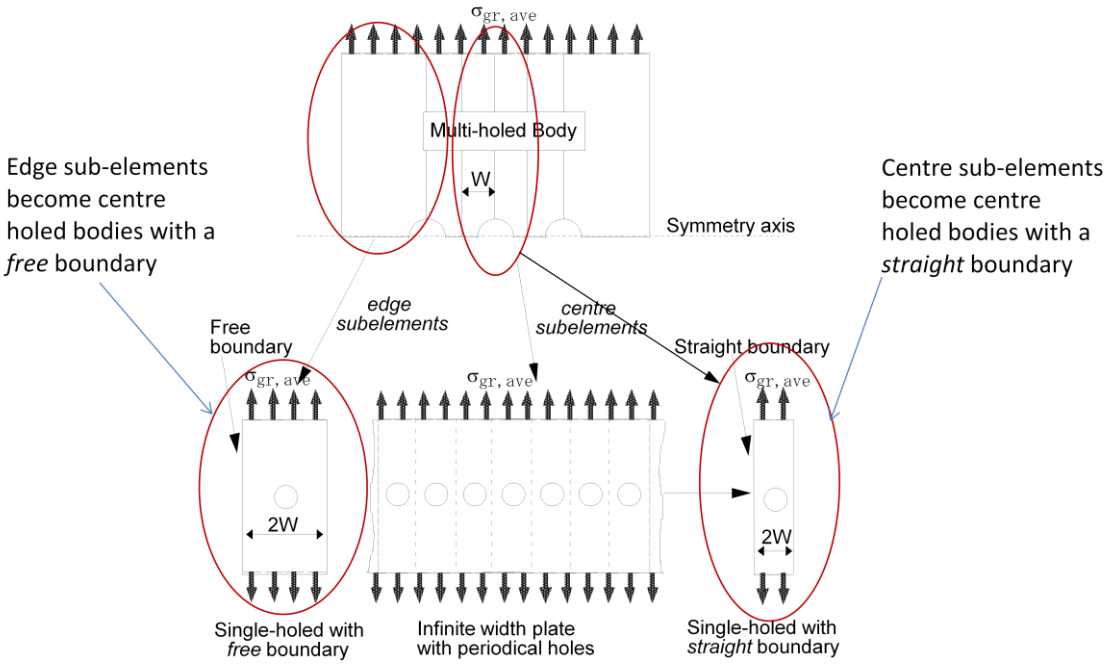

Fig. 7.6: Single-holed bodies used for the approximation of stress distributions of a full multi-holed body.

If we load both, the full multi-holed body and the corresponding single holed bodies by the same gross stress $\sigma_{gr,ave}$ we observed that the net average stresses $\sigma_{net,ave}$ in the ligament sections are nearly identical in both configurations. Thus, the single holed approximation is useful to study the stress distribution of a multi-holed body. This result is shown in Fig. 7.7. In this graph the $\sigma_{net,ave}$ in the centre and edge ligaments normalized with the $\sigma_{gr,ave}$ are compared between the full multi-holed Fig. 7.7 (a) and the separated Fig. 7.7 (b) bodies. The major result is that the averaged net stresses in both figures are nearly the same. The errors in terms of average stress were below 5% except for the filled square (7/1/0.5 geometry). Excluding this narrow edge ligament configuration, this hypothesis is quite effective.

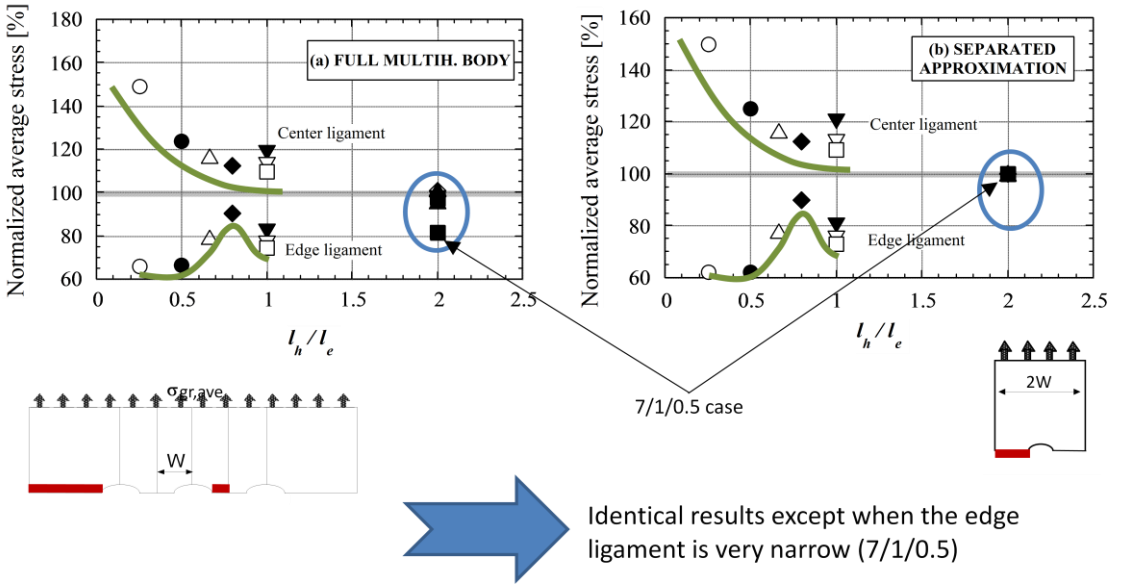

Fig. 7.7: Average stress levels in the center and edge ligaments as a function of the ratio l_h / l_e for multi-holed specimens (a) and approximated single-holed bodies (b).

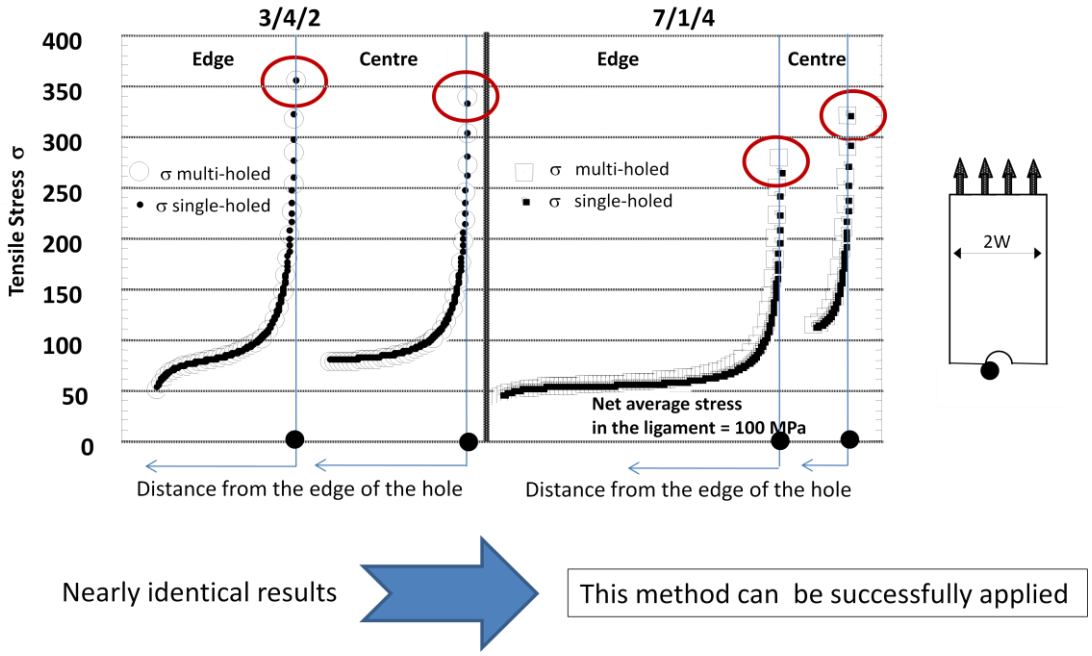

Fig. 7.8: Comparison of tensile stress distributions of the multi-holed specimens 3/4/2 and 7/1/4 and those in approximated single-holed bodies.

In Fig. 7.8, the stress distributions in the edge and centre portions of the 3/4/2 and 7/1/4 configurations are compared. In this figure, the large dotted and open symbols describe the stress distribution of the complete multi-holed body and of the single-holed approximation, respectively. The distributions are also nearly identical. Although the

above calculations were made under the assumption of linear-elastic response, the results suggest that the model using the separated bodies is effective.

7.4.3 Effect of non-linear stress-strain behaviour

Several models have been considered to explain the insensitive behaviour of C/C composites to stress concentration sources like notches or holes [143,144,145,146,147,148]. Among which shear damage induced stress relaxation[88-90] is one of the most widely discussed. For this case, shear damage propagating parallel to the loading direction was expected to significantly reduce the tensile stress concentrations at notches or holes. The shear damage should be related to the non-linearity of the shear stress-strain curve. Thus, the simulation was carried out using the separated single-holed model and taking the non-linear stress-strain response under shear into account.

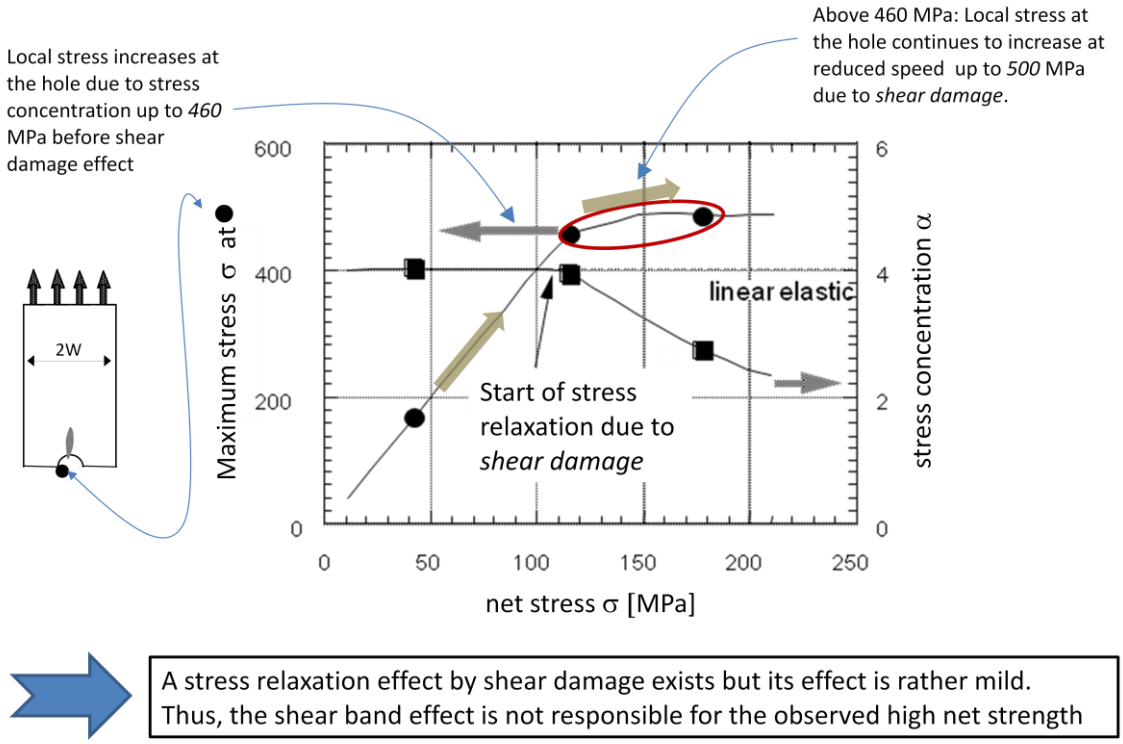

Fig. 7.9: Effect of damage on the stress concentration at the hole for a single holed specimen.

A typical result of the non-linear simulation is illustrated in Fig. 7.9 for a single holed geometry. The vertical axes in Fig. 7.9 represent the maximum stress σ_{max} at the edge of the hole and its stress concentration factor α, defined by

$$\alpha = \frac{\sigma_{max}}{\sigma_{net\ ,ave}} \tag{7.3}$$

as a function of $\sigma_{net,ave}$. In this figure, the maximum tensile stress at the hole σ_{max} increases linearly up to 460MPa, more than twice the tensile strength of the examined material, until shear damage reduces the stress concentration at the hole. We must therefore conclude that there is a stress relaxation effect from shear damage, but the effect is too small to explain the fracture of the examined C/C material in terms of the maximum stress criterion.

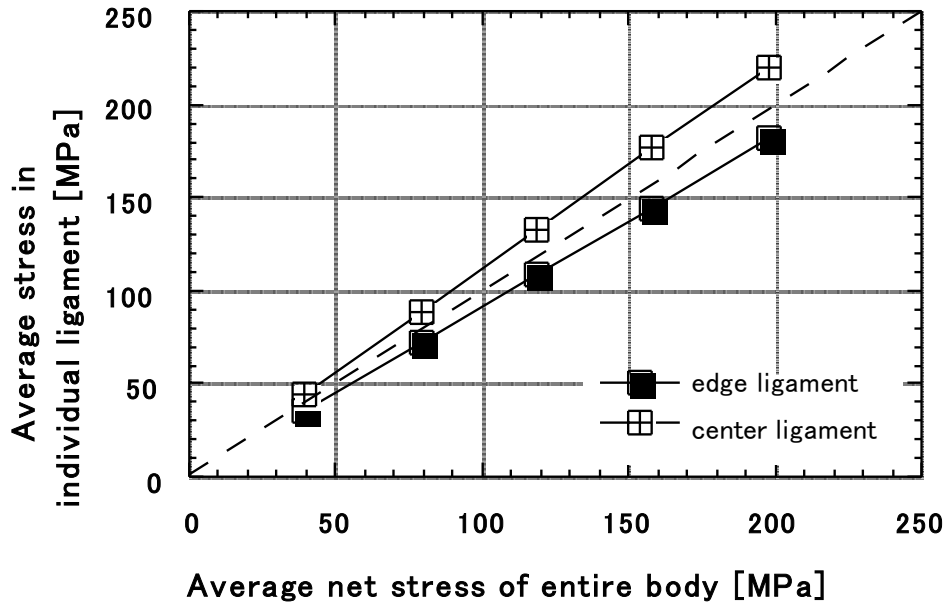

Fig. 7.10: Effect of non-linear shear strain on the average stress in the individual ligament for the specimen 3/4/5.

Next, the average net stresses $\sigma_{net,ave}$ of the centre and edge ligaments of the 3/4/5 body are compared in Fig 7.10. In this figure, in spite of the non-linear shear behaviour, the average stresses in the centre and edge-ligaments increase almost linearly under the applied load. Thus, it can be concluded that though the shear non-linearity changes the stress concentration at the hole, the average stresses in the individual ligaments are practically identical to those of the linear elastic solution. In other words, there is no load redistribution into other ligament sections due to non-linear shear stress/strain behaviour of the C/C.

7.4.4 Prediction of fracture behaviour

To the authors' knowledge, there are presently no established fracture criteria for brittle matrix composites regarding rather mild stress concentrations, as for example specimens with holes. Several techniques have been proposed in the past. Among them, three criteria were frequently examined, namely the linear-elastic fracture mechanics (LEFM)[149], the point stress criterion[150151], and the net stress criterion[152]. In the point stress criterion, two parameters, the strength of a smooth specimen, σ_0, and a characteristic distance, d_0, are introduced. Fracture in this criterion is assumed to occur, when the stress reaches σ_0 at a distance d_0 from the edge of the hole. For some ceramic materials, d_0 was shown to be constant and thus, this criterion is effective. On the other hand, Kiuchi et al.[153] showed for some ceramic matrix composites that the fracture of a notched specimen is simply determined by a constant net sectional stress.

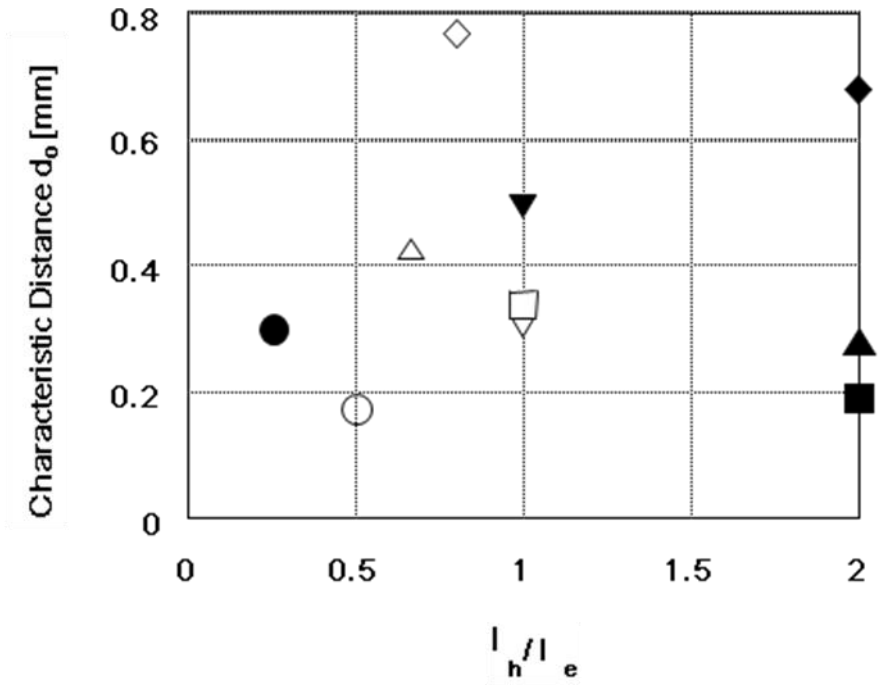

Fig. 7.11: Characteristic distances d_0 of the point stress criterion as a function of l_h/l_e

In Fig. 7.11 the characteristic distances d_0 of the point stress criterion are plotted as a function of l_h/l_e. It can be seen in this figure that the scattering is of d_0 is so large that this criterion is unsuitable in the present case. Then the LEFM approach was applied assuming that the holes were replaced by centre cracks of the same length as the hole diameter[154]. This criterion was also found to be unsuitable. Besides both of them the maximum stress criteria was also examined where the criterion was applied to the

highest stress concentration ligaments. However, the results were poor and this criterion was rejected as well.

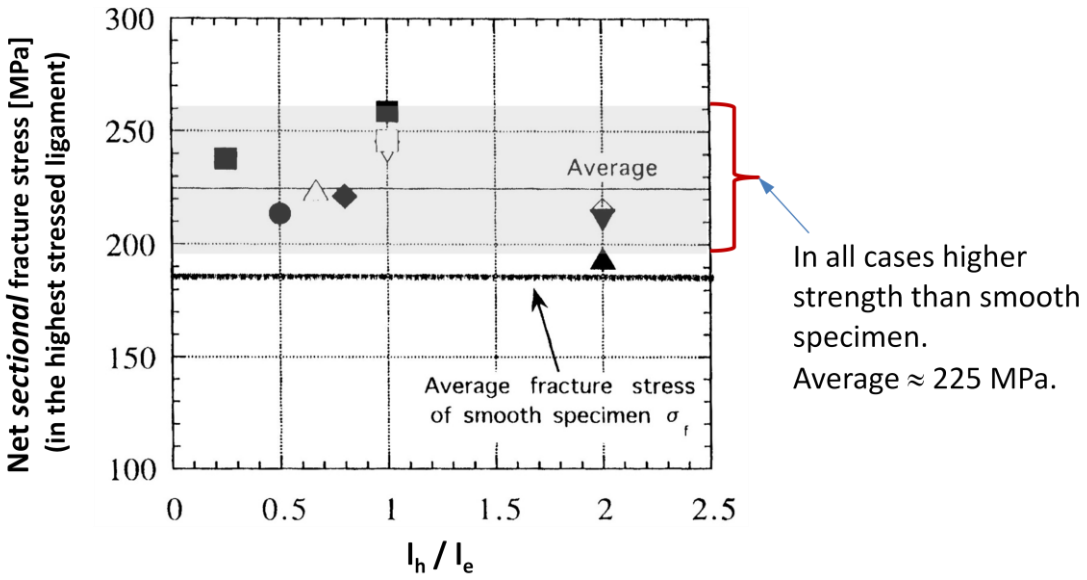

Fig. 7.12: Fracture stress in the highest stressed ligament as a function of l_h/l_e.

As shown in Fig 7.9 there is an effect of shear damage at stress concentration points due to the non-linear shear stress-strain behaviour so that the average stress criterion becomes another possible candidate. Thus, the ligament of the multi-holed body with the highest net average stress was first identified. The average stress at fracture, $\sigma_{f,max}$, was then calculated. The results are shown in Fig. 7.12 as a function of l_h/l_e. In this figure, the data points gather closely around 225 MPa well above the ultimate tensile strength of smooth specimens, though slightly lower values are observed in the case of short l_e. Thus, the average fracture stress in the ligament $\sigma_{f,max}$ can be applied to predict the failure of configurations of multi-holed C/C specimens examined in this study. However, when the distance of adjacent holes becomes much larger, their damage zones will not unite any more and therefore, fracture stresses below the ultimate tensile strength of smooth specimen will most likely be obtained. Thus, the average stress criterion has no universal character and is only valid in cases when the damage zones of stress concentration sources cover nearly all of the ligament section.

7.4.5 Summary

The examined multi-holed C/C composites showed a significant dependency of the net fracture stress $\sigma_{f,net}$ on the two parameters l_h and l_e. The highest $\sigma_{f,net}$ could be obtained for an intermediate value of $l_h/l_e = 1$. For this configuration, the maximum net

fracture stresses were above the fracture stress of smooth specimens.

In addition, a non-linear simulation of shear damage propagation in a CP 0/90 specimen was carried out. The result reveals a stress relaxation effect from shear damage, but this effect does not occur prior to a local stress above 450 MPa, which is more than twice the fracture stress of an un-notched specimen. Thus, shear damage in a shear band fashion does not play a significant role regarding the high toughness of the C/C composite in the 0/90 configuration. The previous results show that the C/C composite's strength drastically increases if the fibre-matrix interface is damaged reducing fibre bundle size and releasing the fibres from the constraint of the matrix. A mechanism explaining the C/Cs high toughness must address this circumstance.

---

[137] H. Hatta, Y. Kogo, H. Asano, et al, Applicability of fracture toughness concept to fracture behaviour of carbon/carbon composites, JSME International Journal, A42(2), pp. 265 (1999)

[138] Y. Kogo, H. Hatta, H. Kawada, et al., Effect of stress concentration on tensile fracture behaviour of carbon-carbon Composites, J. Comp. Mater., 32(13), pp. 1273-1294 (1998)

[139] M. Takabatake, Proc. 8th Symp. High Performance Mater for Severe Environments, Tokyo, pp.279-282 (1997-1999)

[140] A. Okura, T. Chou, Advanced Composites in Emerging Technologies, 348-353, (1992)

[141] Y. Kogo, H. Hatta, H. Kawada, et al., Effect of stress concentration on tensile fracture behaviour of carbon-carbon Composites, J. Comp. Mater., 32(13), pp. 1273-1294 (1998)

[142] G. N. Savin, Stress concentration around holes, Pergamon Press (1961)

[143] A. G. Evans, F. W. Zok, Review, The physics and mechanics of fibre-reinforced brittle matrix composites, J. Mater. Sci., 29, pp. 3857 (1994)

[144] G. Bao, Z. Suo, Appl. Mech. Rev. 45(8), 355-366 (1992)

[145] B. N. Cox, C. S. Lo, Acta Metall. Mater. 40(7),1487-1496 (1992)

[146] B. N. Cox, D. B. Marshall, J. Am. Ceram. Soc. 79(5), 1181-1188 (1996)

[147] F. E. Heredia, M. Spearing, T. J. Mackin, et al., Notch effects in carbon matrix composites, J. Am. Ceram. Soc., 77(11), pp. 2817-2827 (1994)

[148] V. Kostopolous, Y. Z. Pappas, Notched strength prediction of centre-hole carbon/carbon composites, Mater. Sci. Eng., A250, pp.320 (1998)

[149] V. Kostopolous, Y. Z. Pappas, Notched strength prediction of centre-hole carbon/carbon composites, Mater. Sci. Eng., A250, pp.320 (1998)

[150] Y. Kogo, H. Hatta, H. Kawada, et al., Effect of stress concentration on tensile fracture behaviour of carbon-carbon Composites, J. Comp. Mater., 32(13), pp. 1273-1294 (1998)

[151] J. M. Whitney, R. J. Nuismer, Stress fracture criteria for laminate composites containing stress concentrations, J. Comp. Mater., 8(7), pp. 253 (1974)

[152] J. M. Whitney, R. J. Nuismer, Stress fracture criteria for laminate composites containing stress concentrations, J. Comp. Mater., 8(7), pp. 253 (1974)

[153] A. Kiuchi, I. Iwata, N. Nakano, Proc. 4th Symp. High Performance Mater. for Severe Environments, pp. 37-45, (1993) Tokyo

[154] V. Kostopolous, Y. Z. Pappas, Notched strength prediction of centre-hole carbon/carbon composites, Mater. Sci. Eng., A250, pp.320 (1998)

8. Toughening of C/C

8.1 Toughening mechanism

In chapter 4, we obtained irregular shear tests results when the 0° ply ratio r was larger than 0.6. In particular, while the shear strength increased linearly for $r < 0.6$ no further increase could be measured above $r \approx 0.6$. The source of this phenomenon is related to the path of crack propagation which the C/C takes under shear. The shear strength is determined by the strength of the fibres and the main mechanism can be characterized as follows:

1. The shear crack propagates parallel to the fibre directions leaving in case of the 0/90 CP configuration as possible fracture planes the 0° and 90° direction.
2. Shear crack initiation will occur in that fracture plane with the least amount of fibres normal to it to prevent fracture.

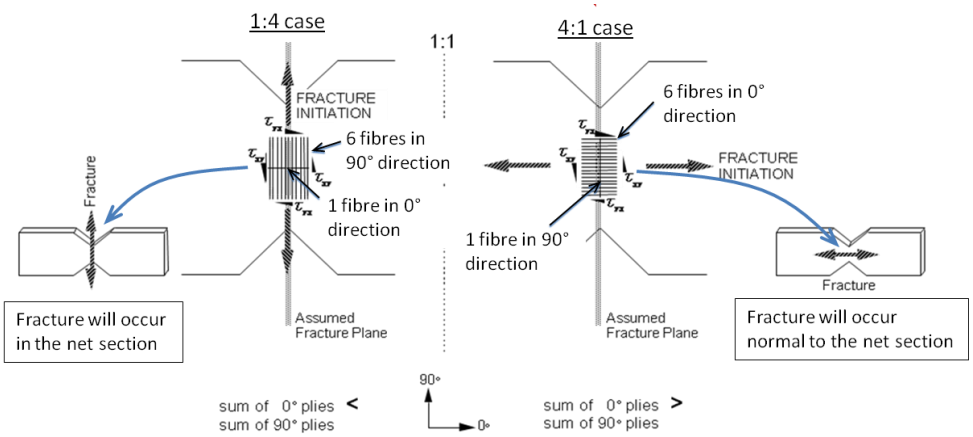

Fig. 8.1: Crack propagation as a function of the fibre orientation.

This situation is demonstrated in Fig. 8.1 for the 1:4 and 4:1 configurations. This figure shows in the top section the experimental results of the shear experiments of Fig. 4.11. In Fig. 4.11 we observed a continuous strength increase in the left side while no further increase was observed on the right. In the lower section of Fig. 8.1 shear fracture is demonstrated by typical representatives, that is the 1:4 configuration for the left case and the 4:1 configuration for the right. In case of the 1:4 configuration which is shown in the lower left section of Fig. 8.1, 6 fibres run parallel to the ligament of a Iosipescu specimen in 90° direction while one fibre is located normal to it in the 0° direction. Recalling that shear stress is symmetric, e.g. $\tau_{xy} = \tau_{yx}$, the shear stress is identical in 0° and 90° direction. Since only one fibre (in the 0° direction) is preventing shear fracture

in the 90° direction in the ligament section, fracture will occur in this direction. The opposite will occur in the 4:1 case shown in Fig 8.1 in the lower right. In this case, 6 fibres are located in 0° direction normal to the ligament section (the assumed fracture plane), but only one fibre is oriented in 90° direction. Since shear stress is symmetric, the stress will much more easily fracture the one fibre in 90° direction than 6 fibres in 0° direction. For this reason the shear crack will propagate in 0° direction into the specimen causing substantial softening of the specimen. However, fracture in the assumed fracture plane of the ligament does not occur. The specimen is practically un-fracturable under shear.

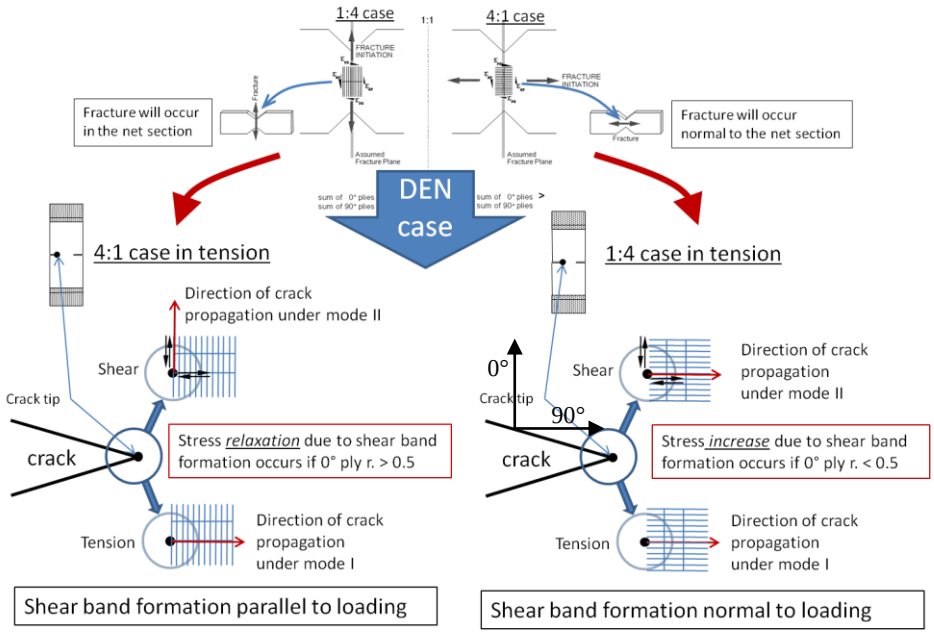

Fig. 8.2: Shear crack propagation at a notched specimen.

Let us now transfer this result to the shear stress situation of a DEN specimen under tensile loading as shown in Fig. 8.2. In this figure, the stress situation at the crack tip is analysed for the same two fibre configurations as in Fig. 8.1. Since the denomination of the specimen was carried out with respect to the longitudinal axis, the shear stress condition of the 1:4 case occurs under tension in the 4:1 specimen. This configuration is shown in Fig. 8.2 in the lower left, while the shear stress condition of the 4:1 case occurring under tension in the 1:4 configuration is shown in the same figure in the lower right.

The tensile stress of a notched DEN specimen in 4:1 configuration leads at the crack tip to a stress field, which consists of a shear and a tensile component. The tensile component results in potential crack propagation under mode I normal to the loading

direction which is shown in Fig. 8.2 on the lower left corner. The shear component leads to crack propagation under mode II into direction parallel to the loading, thus, the crack deflects to mode II. The crack propagation under mode II in direction parallel to the loading results from the fibre orientation. Recalling the symmetry of the shear stress, e.g. $\tau_{xy} = \tau_{yx}$, a shear crack could theoretically propagate normal or parallel to loading. However, since there are much less fibres preventing crack propagation in direction parallel to loading (0° direction) a shear crack will propagate in this direction. Thus, shear band formation parallel to loading leads to stress relaxation.

The 1:4 case of a notched DEN specimen under tensile stress is shown in Fig. 8.2 on the lower right. Again, the tensile component leads to potential crack propagation under mode I normal to the loading direction which is shown in Fig. 8.2 on the lower right corner. The shear case is located right above the tension case in this figure. Again, the symmetry of the shear stress, e.g. $\tau_{xy} = \tau_{yx}$, could theoretically lead to shear crack propagation normal or parallel to the loading direction. However, in the 1:4 case, fewer fibres are preventing crack propagation in direction normal to loading, which is the 90° direction in this figure. Consequently, shear band formation rotates in the 90° direction, and both stresses, shear and tension, lead to crack propagation in the same direction normal to loading. As a consequence, a DEN specimen will always fracture in a mode I fashion if the 0° ply fraction r is less than 0. Consequently, we have to look for 2 different toughening mechanisms depending on the 0° ply fraction leading to three different regions as shown in Fig. 8.3.

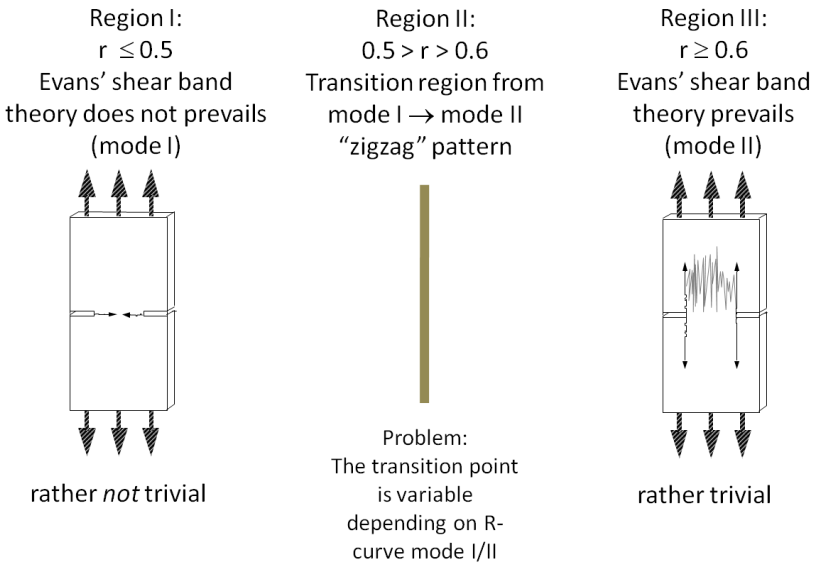

Fig. 8.3: 3 different regions depending on the 0° ply fraction r.

In region I, the direction of shear band fracture has rotated into the same direction as that for tension. Thus, in any case, crack propagation will occur in a mode I fashion normal to the tensile loading direction as shown in Fig. 8.4 on the left. The shear stress field creates in this situation ahead of the crack tip a damage region, which can be differentiated into a slightly (green in Fig. 8.4) and heavily (red in Fig. 8.4) damaged section, shown in the same figure on the right. In the slightly damaged region, many more weak interfaces, caused by shear damage ahead of the crack tip, lead to higher strength than in the undamaged region, shown next to the slightly damaged region on the very right. Here tensile strength enhancement (TSE) is the prevailing mechanism.

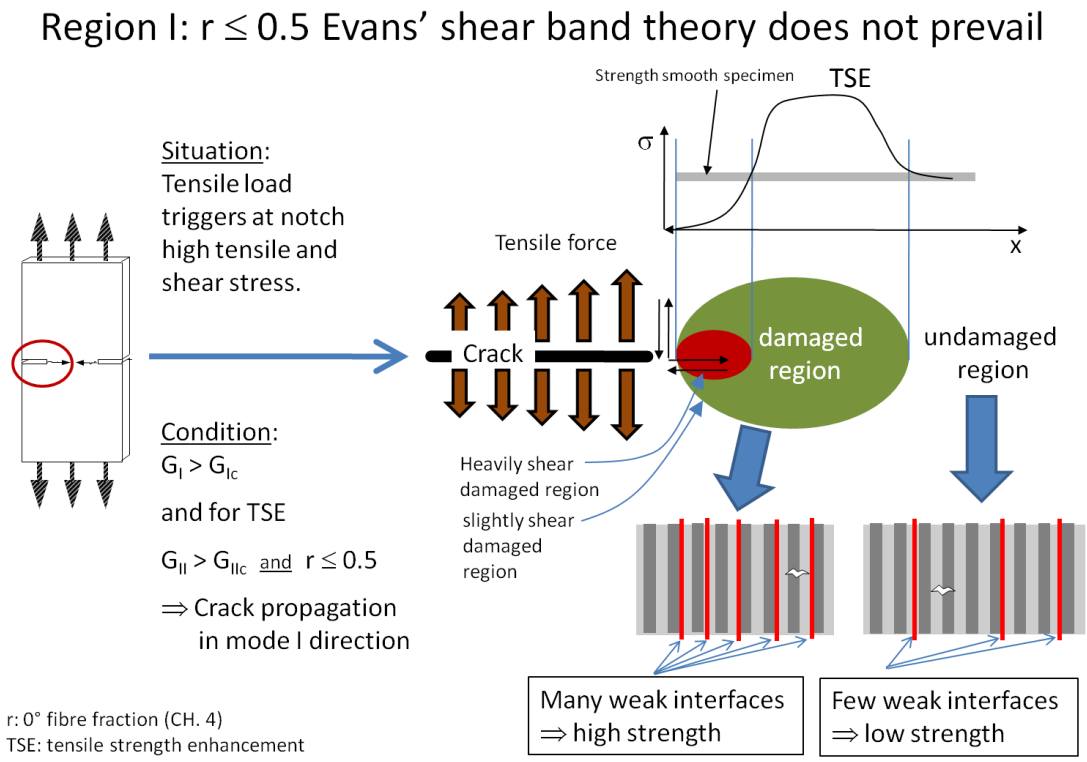

Fig. 8.4: Condition r < 0.5, Evans' shear band theory does not prevail.

In the heavily shear damaged region, shown in Fig. 8.4 in red and in Fig. 8.5 more in detail, two mechanisms have to taken into consideration: The shear strain in the heavily shear damaged region has exceeded the strain at maximum shear stress, $\gamma > \gamma(\tau_{max})$, thus heavy shear damage has occurred. As one consequence of this damage, shear stress must be redistributed away from the crack tip region leading to some blunting effect. In addition, some fibres might already be fractured while the others ahead of the crack tip are nearly completely debonded from the matrix. Thus, in this

region fibre failure occurs one by one and large elongations of the surviving fibres can be expected before ultimate fracture causing some bridging of the crack in the crack tip region.

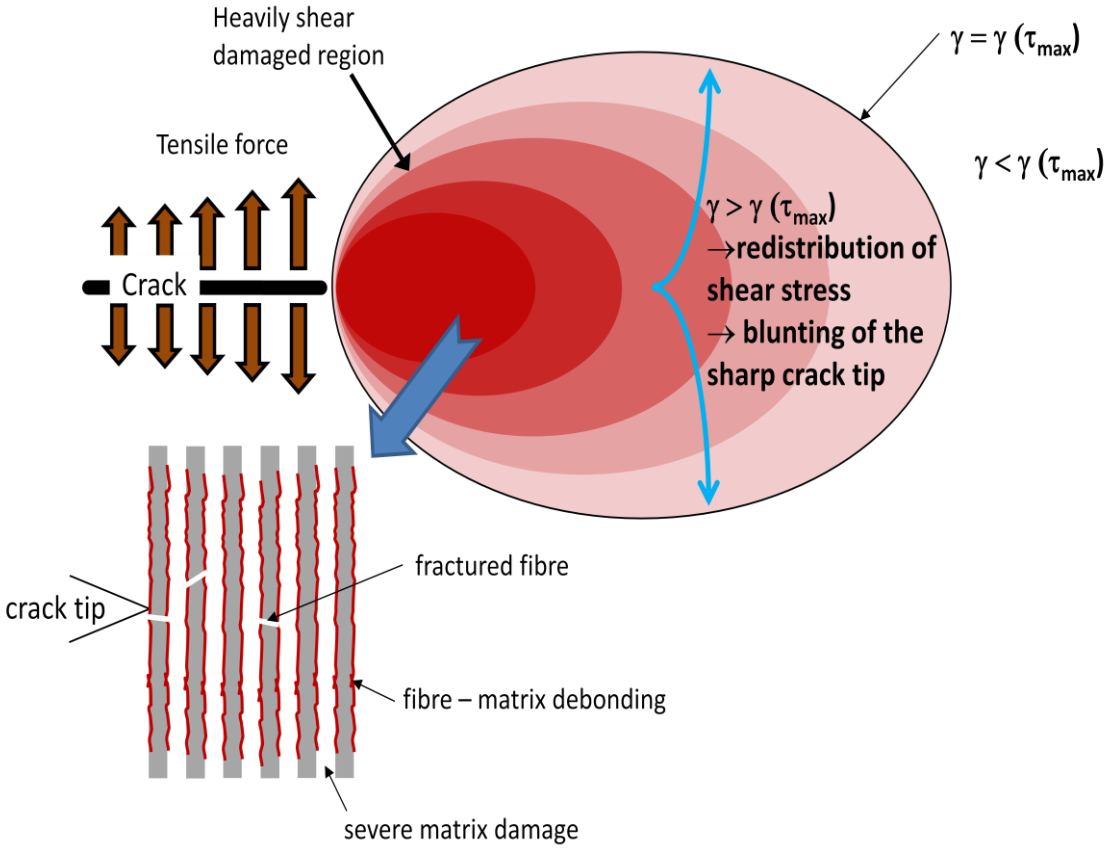

Fig. 8.5: Condition r < 0.5, model of the heavily shear damaged region.

In region II, above $r \approx 0.6$, shear band formation is the prevailing mechanism leading to complete notch insensitivity due to shear band formation. This mechanism is shown in Fig. 8.6. The basic situation is that a specimen is facing at a stress concentration source tensile and shear stress. Under the condition that the critical energy release rate G_c under mode II is reached first and the 0° ply fraction r is larger 0.5, crack initiation and propagation under mode II parallel to loading will occur. The shear crack parallel to loading transforms the DEN specimen into a smooth specimen having the width of the previous net section, as shown in Fig. 8.6 on the right. This mechanism leads in its final stage to complete notch insensitivity and the same material properties as those of a smooth specimen. However, due to effective shielding of the net section from the shear stress field additional strength increase due to damage does not occur.

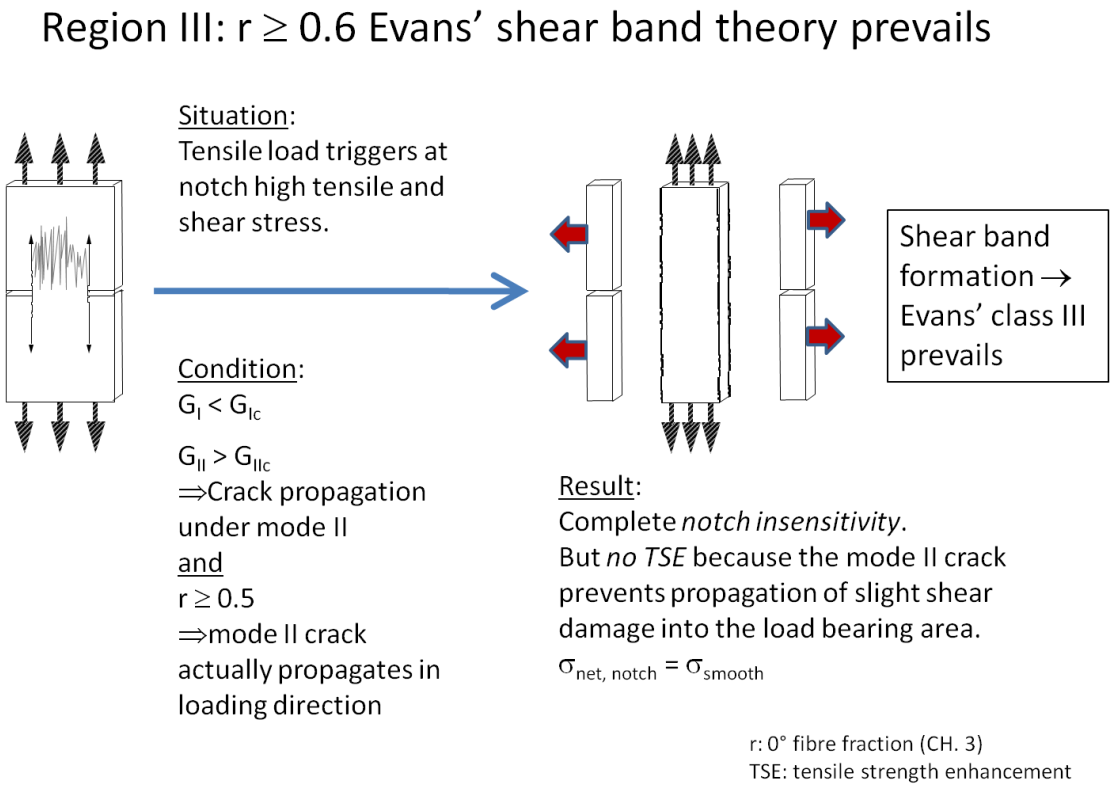

Fig. 8.6: Condition r ≥ 0.6, Evans' shear band theory prevails.

The model of region II, e.g. the transition region from mode I to mode II is shown in Fig. 8.7. In this region the crack might deflect several times prior to ultimate fracture. To understand this phenomenon, let us recall a major result from chapter 6. In this chapter, we found that weak interfaces function as crack propagation boundaries which prevent the crack from penetrating into an adjacent fibre bundles. One possible source of crack propagation boundaries are transverse cracks originating from the cooling stage. At the same time we have to keep in mind that new cracks preferably propagate on top of transverse cracks. Thus, we can identify a grid pattern of transverse cracks in horizontal and vertical direction which determine possible paths for crack propagation. That means, a crack will preferably propagate on top of a transverse crack until the crack tip hits a transverse crack normal to its own direction. At this "intersection" the crack will arrest and the energy release rates under mode I and mode II will be newly evaluated. The crack will finally propagate in that direction in which the critical energy release rate is exceeded first. Thus, each intersection of a horizontal and vertical transverse crack is a possible crack deflection point. This mechanism causes crack propagation in a rectangular fashion.

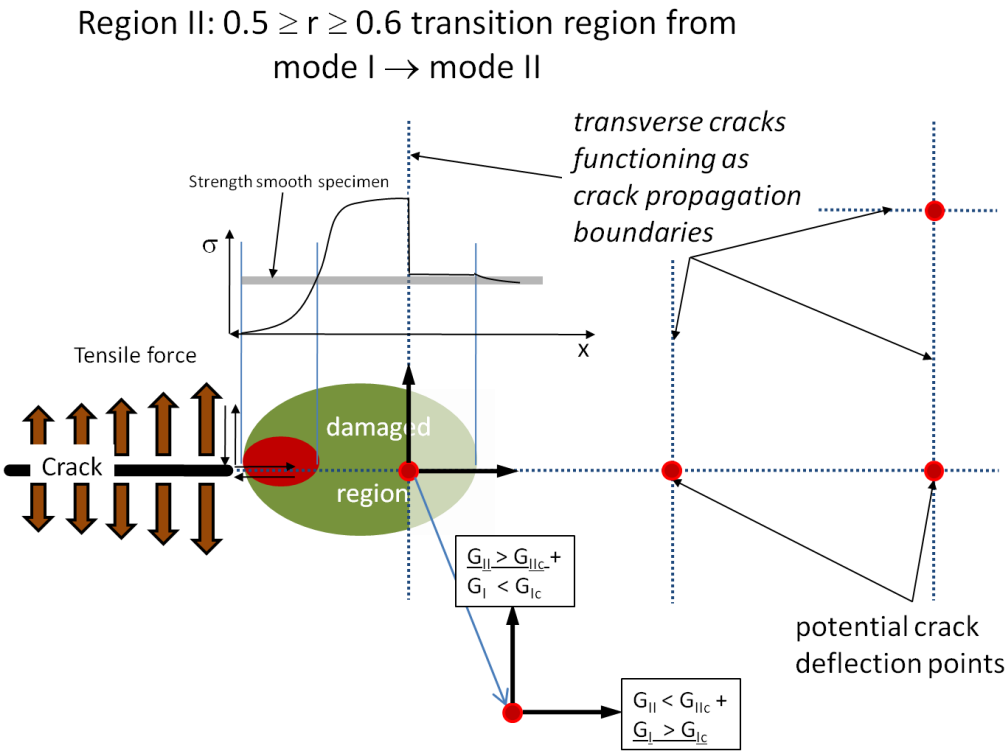

Fig. 8.7: Transition region between mode I and mode II.

8.2 Outlook

In the previous section the toughening of C/C was explained by two different mechanisms. While shear band formation is rather straight forward, the mechanism for $r < 0.5$ depends on the damage zone. When moving in a next step from a qualitative to a numerical analysis, the evaluation of the damage zone size and its properties bears the main obstacles as shown in Fig. 8.8. In particular, open issues exist regarding the size and the stress distribution of the heavily shear damaged region as a function of the stress field and regarding the evaluation of the blunting effect. Similar obstacles appear when moving from the heavy to the slightly shear damaged region. The size and stress distribution and its effect on tensile strength must be evaluated more in detail.

The second issue focuses on the modelling of crack propagation under shear in one single direction. In Abaqus FEM calculations, damage is modelled by softening of the shear modulus. This technique does not allow shear failure in one particular direction. Thus, only the CP 0/90 case can be modelled non-linear with some accuracy. To overcome this obstacle, fibre and matrix must be modelled separately.

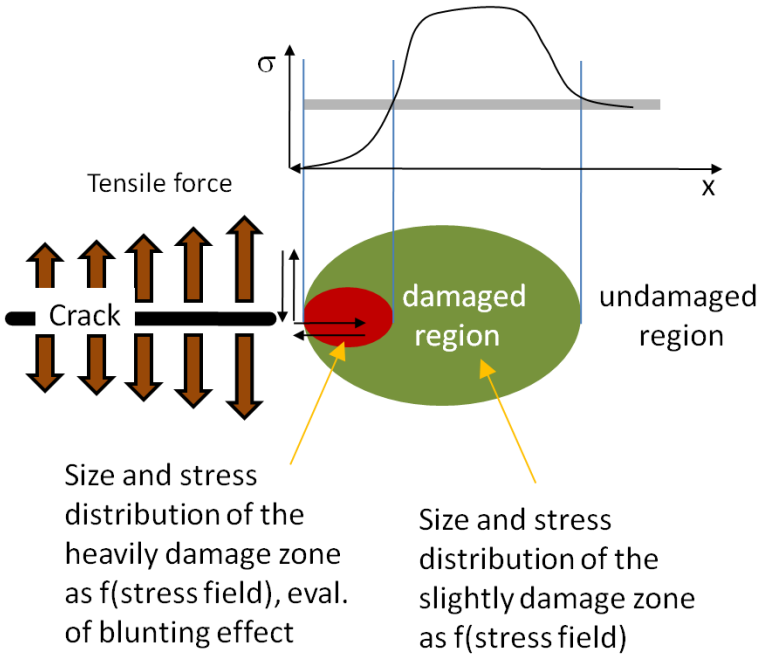

Fig. 8.8: Condition r < 0.5, model of the heavily shear damaged region.

9. Summary

9.1 Summary of this work

In this work, a model was established to explain the fracture behaviour of a cross-ply laminate type C/C composite from mode I to mode II. Three regions can be distinguished. In region I pure mode I fracture occurs and the prevailing toughening mechanism is damage of the fibre matrix interface. In region III, mode II fracture occurs prior to ultimate fracture leading to notch insensitivity. In the intermediate region II, a crack might deflect several times from mode I to mode II and vice versa prior to ultimate fracture.

9.2 Summary with respect to the chapters

C/C belongs to the brittle matrix composites which exhibit a high degree of toughness. According to Evans et al.[155], these materials can be distinguished into 3 different classes with respect to their toughening mechanism. In these categories, the C/C composite would fall into class III for which shear band formation is the prevailing mechanism. In our terminology, we understand as shear band formation the propagation of a crack under mode II originating at a notch tip. The shear band formation causes stress relaxation at the notch root leading to notch insensitivity. This phenomenon can be easily observed in case of the UD 0. However, in case of a cross-ply 0/90, the failure pattern is completely different. These specimens fail under clear mode I without any visible shear crack under mode II. This casts doubt on the universal application of the shear band theory (Ch.2). Moreover, some CP 0/90 specimens revealed higher net-strengths than corresponding un-notched specimens, a phenomenon which can hardly be understood in terms of stress relaxation.

To examine this phenomenon more in detail, tensile tests of notched specimens with various degrees of fibre orientation between the UD0 and UD 90 configuration were carried out. The configurations were distinguished by their fraction of fibres in 0° direction with respect to the total amount of fibres in 0° and 90° direction, the so-called 0° ply ratio *r*. The fracture of the C/C specimen could be distinguished into 3 regions. Specimen with *r* up to 0.5 revealed, considering the high stress concentration at the notch, a high degree of toughness with strengths approx. 15% lower than their un-notched counter parts (Region I). These specimens failed under mode I. Above *r* = 0.6, shear band formation occurred leading to complete notch insensitivity (Region III). Although notch insensitivity occurred and although a mode II crack became visible, the

carbon fibres crossing the mode II crack did not fracture. In Region II ($0.5 < r < 0.6$) crack deflection from mode I to mode II and vice versa may occur several times before ultimate fracture (Ch.3).

To understand the damage occurring in the shear band (Region III) a clear understanding of the fracture mechanism under shear is indispensable which led to the examination of the shear fracture behaviour. The shear stress-strain curve was found to be non-linear nearly from the beginning which was due to fibre matrix debonding and matrix cracking. When the peak shear stress was reached, fracture of all fibres occurred which was accompanied by a sharp drop of the shear stress. At this stage the specimens were completely fractured. However, substantial shear load could still be carried due to friction between the fracture surfaces. To attain these results, tensile tests after shear pre- loading had been carried out. During these tests, specimen with very slight shear damage revealed in the subsequent tensile tests higher tensile strength than non-shear damaged specimen which was due to interfacial damage of fibre and matrix. In the shear tests, the same material configurations as in previous tensile tests had been used and shear strength was found to increase similar to tension with r. However, two possible fracture planes exist and fracture occurs always in the weaker plane. For this reason, it is impossible to attain reasonable results above $r = 0.5$ (Ch.4).

More detailed examination of the high strength behaviour after shear preloading (tensile strength enhancement, TSE) revealed that higher strength can be obtained by several ways as long as the fibre-matrix interfacial strength is reduced without damaging the fibres (Ch.5).

A reduction of the fibre-matrix interfacial strength was found to lead to an increasing amount of weak fibre-matrix interfaces. These fibre-matrix interfaces act as crack propagation boundaries resulting in smaller fibre bundles. Due to the low toughness of the fibres, fracture of single fibres results in the failure of complete fibre bundles. However, the amount of load which has to be redistributed among surviving fibre bundles is small if the fractured fibre bundle is small. Therefore, material with a smaller fibre bundle size is more likely to sustain the load of fractured fibre bundles which in the end leads to higher ultimate strength (Ch.6)

The previous bending tests of the shear band region revealed no fibre breakage. Knowing from the shear tests that no serious shear damage occurs prior to fibre fracture leads to the conclusion that the shear damage in Region I must be small. To verify this assumption, a non-linear FEM calculation of a centre-holed specimen was carried out. In this calculation, the shear stress-strain behaviour was programmed to follow the in a previous shear test obtained non-linear shear stress-strain curve while the tensile behaviour was assumed to be linear-elastic. The calculation result supports the above

assumption. The local stress at the hole reaches up to 460 MPa before tensile stress relaxation due to shear damage becomes effective. Nevertheless, the local tensile stress at the hole does not drop from this point but increases slightly up to 500 MPa with increasing remote loading. Thus, the stress relaxation effect from shear damage in Region I is slight and the high tensile stress occurring at the hole must be included in any kind of model explaining the C/C's high toughness (Ch.7).

The small effect from shear damage in Region I leads to the conclusion that linear-elastic fracture mechanics (LEFM) can be applied in this region. This can be demonstrated by DEN experiments with constant ratio of notch length a and width w being $a / w = 0.5$ and increasing width. When evaluating the shear damage ahead of the crack tip in this region a shear crack is found to propagate in mode I direction of a mode I crack. For this reason mode II shear band formation is impossible to occur if $r < 0.5$. In this region the shear damage causes directly ahead of the crack tip a heavily shear damaged zone in which a mix of fractured fibres and to single fibres reduced fibre bundles exist. The surviving single fibre bundles cause bridging which is the class II toughening mechanism in the Evans' terminology. Beyond this region, a slightly shear damaged region is located in which shear damage results in a reduced fibre bundle size. This smaller than original fibre bundle size results in increasing strength ahead of the crack. In Region III shear band behaviour (the class III toughening mechanism) is the dominant mechanism as described before by Evans et al. leading to notch insensitivity. Considering that in both cases, a crack under mode I or II will propagate in a transverse crack originating from the cooling stage, the junction of a crack in horizontal and normal direction functions as potential crack deflection point. In Region II a crack might deflect at each of these "junctions" depending on whether the critical energy release rate G_c is first exceeded under mode I or II, causing the observed zigzag crack pattern in this region (Ch.8).

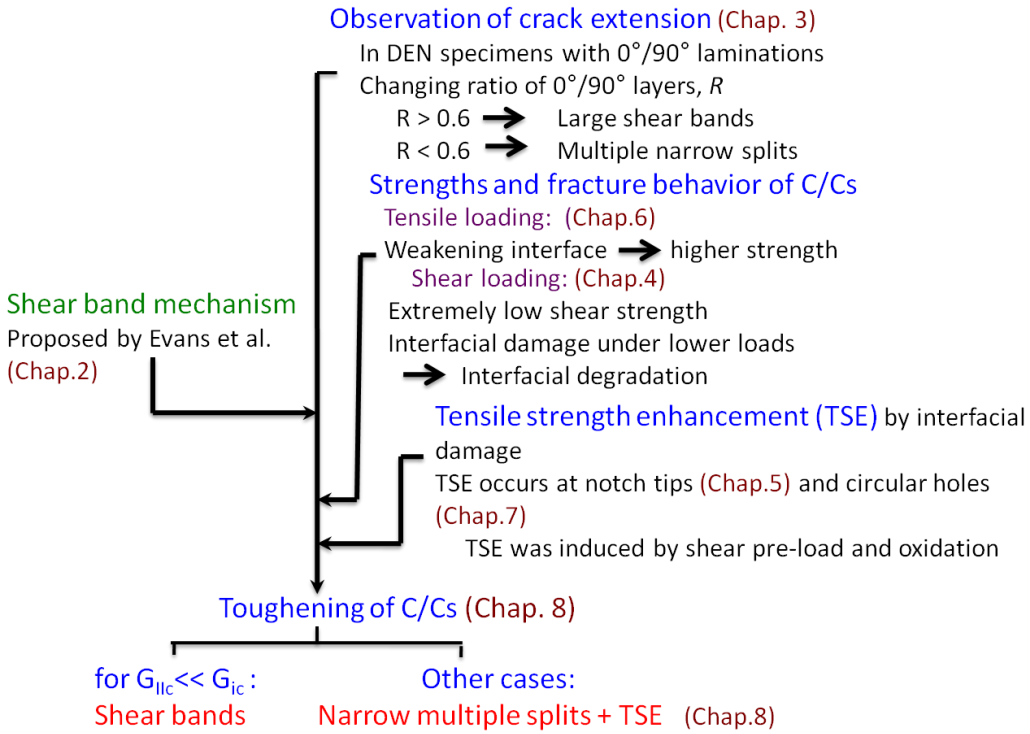

Fig. 9.1: Flow of the paper

---

[155] A. G. Evans, F. W. Zok, Review, The physics and mechanics of fibre-reinforced brittle matrix composites, J. Mater. Sci., 29, pp. 3857 (1994)

Acknowledgement

This work would not have been possible without all the people who contributed in many different ways to it. In particular, I would like to thank my family for their continuous support and Mr. Aoi and Dr. Mohamed Sayed Aly-Hassan from ISAS for their help during experiments and for the experimental data I used in this work. In addition, I would like to thank Professor Sato, Professor Goto, Professor Ishimura, Professor Kogo, and Professor Wakayama from the board of examiners for their effort and fruitful remarks on my work.

Most of all, I would like to thank my teacher, Professor Hatta, for his continuous support for more than a decade and through periods at which a successful end was almost out of sight. His support, advice, and motivation made this PhD possible. There are no words to express my gratefulness.